Interfacial Engineering of the Magnetism in 2D Magnets, Topological Insulators, and Their Heterostructures

Hangtian Wang

To cite this version:

Hangtian Wang. Interfacial Engineering of the Magnetism in 2D Magnets, Topological Insulators, and Their Heterostructures. Physics [physics]. Université de Lorraine; Beihang university (Pékin), 2023. English. NNT : 2023LORR0206 . tel-04536873

HAL Id: tel-04536873
https://hal.univ-lorraine.fr/tel-04536873v1

Submitted on 8 Apr 2024

École Doctorale C2MP

Institut Jean Lamour

Beihang University

Thèse

Présentée et soutenue publiquement pour l'obtention du titre de
DOCTEUR DE l'UNIVERSITE DE LORRAINE

Mention : Physique

par **Hangtian WANG**

Sous la direction de **Stéphane MANGIN (FRANCE)**
Weisheng ZHAO (CHINE)
Tianxiao NIE (CHINE)

Interfacial Engineering of the Magnetism in 2D Magnets, Topological Insulators, and Their Heterostructures

21/10/2023

Membres du jury:

Directeur(s) de thèse:	Stéphane MANGIN	Professeur, Université de Lorraine
	Weisheng ZHAO	Professeur, Beihang University
Président de jury:	Jörg WUNDERLICH	Professeur, Universität Regensburg
Rapporteurs:	Jörg WUNDERLICH	Professeur, Universität Regensburg
	Guoqiang YU	Professeur, University of Chinese Academy of Sciences
Examinateurs:	Shunsuke FUKAMI	Professeur, Tohoku University
	Na LEI	Professeur, Beihang University
	Grégory MALINOWSKI	Chargé de recherche, Université de Lorraine

Interfacial Engineering of the Magnetism in 2D Magnets, Topological Insulators, and Their Heterostructures

Author:

Hangtian WANG

Stéphane MANGIN Professor, University of Lorraine, Director

Weisheng ZHAO Professor, Beihang University, Director

Tianxiao NIE Professor, Beihang University, Director

ACKNOWLEDGMENT

I would like to express my gratitude to my supervisor, Professor Stéphane MANGIN. It is because of standing on your shoulders that I have been able to come this far. Thank you for your meticulous guidance in my study, and for being an excellent role model in my life. When I embarked on my PhD study in France with nothing but passion, it was you who welcomed me and provided me with unwavering support.

I would also like to express my gratitude to Professor Thomas Hauet, Professor Sébastien Petit-Watelot, and Professor Yannick Fagot-Revurat from the Jean Lamour Institute. Every time when I encountered difficulties in my research, they always selflessly offered me help, and each discussion with them has been enriching. I am thankful to Stéphane Suire, Sylvie Robert, Laurent Badie, Sylvie Migot, Jaafar Ghanbaja, and Luc Moreau for their patiently teaching about equipment manipulation. I extend my gratitude to my colleagues during my time in France: Héloïse Damas, Anna Friedel, and Yan. Thank you for your assistance in my life and studies. Your warmth and friendliness made me feel welcome in this unfamiliar country. I also want to thank the friends I made in Nancy: Yang Wei, Lv Chen, Liu Lin, Wang Tao, Zhou Mengxi, Zhang Wei, and Peng Yi. Thank you for accompanying me during my wonderful time studying in France. These memories will be the most cherished in my life.

I would like to thank my friends Huang Tianxun and Guo Zongxia. We have enjoyed the landscapes of foreign countries together, ventured into volcanoes and glaciers, paddled on lakes and seas, and even journeyed to the ends of a solitary world. Although we are now separated by distance, I still wish that we can all have a bright future.

I am grateful to my father, Wang Yu, my mother, Pan Qingjie, and my girlfriend, Zhou Zitong. It was their unconditional support and encouragement that give me confidence to face the difficulties and make my own decision.

Hangtian WANG

30th August 2023, Beijing, China

TABLE OF CONTENTS

LIST OF ABBREVATIONS

GMR	giant magnetoresistance
MTJ	magnetic tunnel junction
TMR	tunnel magnetoresistance
MRAM	magnetoresistive random access memory
FM	ferromagnetic
AFM	antiferromagnetic
TI	topological insulators
QL	quintuple layer
QAHE	quantum anomalous Hall effect
SIA	single-ion perpendicular magnetocrystalline anisotropy energy
SOT	spin orbital torque
SOC	spin-orbital coupling
MBE	molecular beam epitaxy
RHEED	reflection high-energy electron diffraction
XRD	X-ray diffraction
FWHM	full width at half maximum
AFM	atom force microscope
TEM	transmission electron microscope
MOKE	magneto-optic Kerr effect
VSM	vibrating sample magnetometer
SQUID	superconducting quantum interference device
PPMS	physical property measurement system
HAADF-STEM	high-angle annular dark-field scanning transmission electron microscopy
EDS	energy dispersive spectroscopy
DFT	density functional theory

PDOS	partial density of states
DOS	density of states
UPS	ultraviolet photoelectron spectroscopy
XPS	X-ray spectroscopy
IBE	ion beam etching
FIB	focused ion beam
FMS	ferromagnetic semiconductor
WL	weak localization
WAL	weak antilocalization
EEI	electron-electron interaction
ARPES	angle-resolved photoemission spectroscopy
THz-TDS	terahertz time-domain spectroscopy
CPGE	circular photogalvanic effect
LPGE	linear photogalvanic effect
SCC	spin-charge conversion
IEE	inverse Edelstein effect
ISHE	inverse spin Hall effect

Abstract

With the critical node of integrated circuits (IC) entering the 1 nm stage, traditional three-dimensional materials cannot maintain their original physical properties, and thus cannot meet the needs of IC manufacturing processes. Meanwhile, the shrinking line width also introduces an inevitable increase in static power consumption. Therefore, researching new materials and new technologies to break through the "Size Wall" and "Power Wall" has become a crucial direction in the IC industry. As a new member of the two-dimensional (2D) material family, the 2D magnets can maintain its long-range magnetic order at the atomic scale with its physical properties easily controlled by external stimuli, which provides an ideal platform for the high-density and low-power spintronic devices.

However, due to the dimensional effect, 2D magnetism cannot exist at high temperatures. Although several methods can enhance the Curie temperature (T_c) of 2D magnets (such as doping, ion intercalation, or laser pumping), they are far from easy-controllability and high-efficiency. More importantly, the widely-used preparation method via mechanical exfoliation abandons the merit of 2D interfacial effect, which was proved to be an important approach to efficient 2D magnetic manipulation. Therefore, studying the interfacial effect in epitaxial 2D magnets is regarded as a key field to achieving large-scale, high-T_c, easy-controlling, and stable 2D ferromagnetic order. Topological insulator (TI) is another 2D material with strong spin-orbital coupling. The topology-protected surface states provided TI with numerous fascinates spin-related effects, such as spin-momentum locking, spin exchange effect, etc., which makes this material a potential candidate to fabricate effective spintronic devices. In addition, the TI can be integrated with 2D magnets to form a 2D heterostructure, in which not only the magnetism can be enhanced via the interfacial effect, but also the spin-related properties of the heterostructure can be manipulated due to the advantages of these two materials. To explore these issues, the work of this paper is as follows:

1. **A high-T_c magnetism with controllable magnetic anisotropy was achieved in 2D vdW**

film FGT via magnetic doping. Due to the limitation of mechanical exfoliation, it is hard to achieve large-scale preparation of 2D magnet with high T_c. In this thesis, we successfully achieve the wafer-scale epitaxy of 2D magnet FGT (including Fe_3GeTe_2 and Fe_4GeTe_2). After that, we established a Heisenberg model including RKKY interaction to explain the origin of its 2D ferromagnetic order. According to this model, we achieved the magnetism manipulation in Fe_4GeTe_2 by controlling the Fe flux rate during the growth and obtained a high-temperature, robust, easy-handling magnetic anisotropy in the film.

2. **The modulation of the interfacial magnetism in 2D magnets was confirmed from both the theory and experiment.** Through a series of thickness-dependent experiments, we proved that the Fe_4GeTe_2/Al_2O_3 interface can enhance the T_c of the Fe_4GeTe_2 film greatly. Combining the first principles simulations and photoelectron spectroscopy methods, we theoretically and experimentally demonstrated that the local state shift of Fe *d* electrons introduced by orbital coupling in the interface is responsible for the increase in the T_c.
3. **A high-quality topological insulator (TI) thin film was prepared and a 2D magnetism was induced in the film by the interfacial proximity effect.** After achieving high-quality TI film epitaxy (including Bi_2Se_3 and Bi_2Te_3), we fabricated a topological magnetic heterostructure Bi_2Se_3/MnGe and studied the 2D magnetism induced by the interfacial proximity effect. The long-range ferromagnetic order in the heterostructure can be verified by transport measurement results, which presents a transition from WAL to WL feature. By quantifying the conductance quantum correction resulting from WAL and WL, we proved that an 80 meV bandgap could be opened in TI's surface state by the interfacial proximity effect.
4. **The magnetism and spin manipulation effects by interfacial effect in the 2D topological magnetic heterostructure was revealed by multiple characterization results.** After integrating TI and FGT to form a 2D heterostructure, we demonstrated a manipulation on the T_c and the magnetic anisotropy by the interfacial effect. In addition,

we studied the magnetic properties of Bi_2Te_3/Fe_4GeTe_2 by terahertz (THz) method, which proved again the T_c enhancement by the interfacial effect. Moreover, the THz time domain spectra clarified the ultrafast spin-charge conversion process in the 2D magnetic interface.

Key words： two-dimensional magnet, topological insulator, two-dimensional heterostructure, interfacial effect

Résumé en Français

Avec les tailles des circuits intégrés (CI) atteignant des tailles caractéristiques de 1 nanomètre, les matériaux traditionnels ne peuvent plus maintenir leurs propriétés physiques d'origine, et par conséquent, ils ne peuvent pas répondre aux besoins des processus de fabrication des CI. Parallèlement, la réduction des tailles génère une augmentation inévitable de la consommation d'énergie statique. Par conséquent, la recherche de nouveaux matériaux et de nouvelles technologies pour surmonter la "limite de Taille" et la "limite de Puissance" est devenue une direction cruciale dans l'industrie des CI. De nouveaux matériaux bidimensionnels (2D), les matériaux magnétiques 2D peuvent maintenir leur ordre magnétique à longue portée à l'échelle atomique, avec des propriétés physiques facilement contrôlées par des stimuli externes. Cela offre une plateforme idéale pour les dispositifs spintroniques à haute densité et à faible consommation d'énergie.

Cependant, en raison de l'effet dimensionnel, le magnétisme 2D ne peut pas exister à des températures élevées. Bien que plusieurs méthodes permettent d’augmenter la température de Curie (Tc) des matériaux magnétiques 2D (telles que le dopage, l'intercalation ionique ou le pompage laser), elles sont loin d'être faciles à contrôler et d'être efficaces. De plus, la méthode de préparation par exfoliation mécanique largement utilisée abandonne l'avantage de l'effet interfacial 2D, qui s'est avéré être une approche importante pour une manipulation magnétique 2D efficace. Par conséquent, l'étude de l'effet interfacial dans les matériaux magnétiques 2D épitaxés est considérée comme une technique clé pour atteindre un ordre ferromagnétique 2D à grande échelle, haute Tc, facile à contrôler et stable.

L'isolant topologique (IT) est un autre matériau 2D avec un fort couplage spin-orbite. Les états de surface protégés par la topologie confèrent à l'IT de nombreux effets liés au spin, tels que le verrouillage spin-moment cinétique, l'effet d'échange de spin, etc., ce qui fait de ce matériau un candidat potentiel pour fabriquer des dispositifs spintroniques efficaces. De plus, l'IT peut être intégré avec des matériaux magnétiques 2D pour former une hétérostructure 2D, dans laquelle non seulement le magnétisme peut être renforcé par l'effet interfacial, mais aussi les propriétés liées au spin de l'hétérostructure peuvent être manipulées grâce aux avantages de ces deux matériaux. Ce travail de Thèse a permis de faire de nombreuses avancées majeures dans ce domaine

1) Un matériau magnétique 2D (FeGeTe dopé) avec une température de Curie (T_c) supérieure à la température ambiante dont l’ anisotropie est modulable a été réalisé.

En raison de la limitation de l'exfoliation mécanique, il est difficile d'obtenir une préparation à grande échelle d'un matériau magnétique 2D à haute Tc. Dans cette thèse, nous avons réussi à obtenir l'épitaxie à l'échelle de la plaquette du matériau magnétique 2D FGT (composé de Fe_3GeTe_2 et Fe_4GeTe_2). Ensuite, nous avons établi un modèle de Heisenberg incluant l'interaction RKKY pour expliquer l'origine de son ordre ferromagnétique 2D. Selon ce modèle, nous avons réussi à manipuler le magnétisme dans le Fe_4GeTe_2 en contrôlant la concentration de Fe pendant la croissance et avons obtenu une anisotropie magnétique à haute température, robuste et facile à manipuler.

2) **Manipulation des propriétés magnétiques du matériau magnétique 2D (FeGeTe) en contrôlant l’interface, confirmée théoriquement et expérimentalement.**

Grâce à une série d'expériences dépendant de l'épaisseur, nous avons prouvé que l'interface Fe_4GeTe_2/Al_2O_3 peut grandement améliorer la T_c du film Fe_4GeTe_2. En combinant les simulations des premiers principes et les méthodes de spectroscopie photoélectronique, nous avons démontré théoriquement et expérimentalement que le déplacement de l'état local des électrons d du Fe induit par le couplage orbital dans l'interface est responsable de l'augmentation de la T_c.

3) Croissance d'isolant topologique (TI) de haute qualité sur matériau magnétique 2D observation des effets de proximité interfaciale.

Après avoir réussi l'épitaxie d'un film de TI de haute qualité (composé de Bi_2Se_3 et Bi_2Te_3), nous avons fabriqué une hétérostructure magnétique topologique Bi_2Se_3/MnGe et étudié le magnetisme 2D induit par l'effet de proximité interfaciale. L'ordre ferromagnétique à longue portée dans l'hétérostructure peut être vérifié par les résultats de mesure du transport, présentant une transition de l'effet de localisation faiblement antilocalisée (WAL) à l'effet de localisation faiblement localisée (WL). En quantifiant la correction quantique de la conductance résultant de WAL et WL, nous avons prouvé qu'une bande interdite de 80 meV pouvait être ouverte dans l'état de surface du TI par l'effet de proximité interfaciale.

4) Manipulation de l’aimantation et du spin grâce aux interfaces dans l'hétérostructure Bi_2Te_3/Fe_4GeTe_2 topologique 2D.

Après l'intégration de l'IT et du FGT pour former une hétérostructure 2D, nous avons démontré une manipulation de la Tc et de l'anisotropie magnétique par l'effet interfacial. Nous avons étudié les propriétés magnétiques de Bi_2Te_3/Fe_4GeTe_2 par une méthode terahertz (THz), ce qui a de nouveau confirmé l'augmentation de la T_c par l'effet interfacial. De plus, les spectres THz ont clarifié le processus ultra-rapide de conversion spin-charge dans l'interface magnétique 2D.

Mots-clés: aimant bidimensionnel, isolant topologique, hétérostructure bidimensionnelle, effet interfacial.

Chapter 1. Introduction

The rapid development of the information technology has led to an increasingly demand for data storage, processing, and transmission capabilities of integrated circuits (IC) devices. However, constrained by device size and power consumption, the development of Moore's Law is gradually reaching its limits[1]. Therefore, researching new materials and devices to overcome the "size wall" and "power wall" has become a key direction in the IC field. Spintronics is a new technology that focuses on the electron spins. Unlike traditional CMOS devices that manipulate charge for information transmission, spintronic devices control the electron spins to achieve information read/write operations, offering advantages such as low power consumption, radiation resistance, and non-volatile data storage[2]. Two-dimensional (2D) magnets are a new member of the 2D materials family. Based on these materials, 2D spintronic devices can inherit the advantages of 2D materials and the spintronic materials, achieving high-intensity, low power-consumption information reading/writing, which potentially breaks through the "power wall" and "size wall" that currently restrict the development of IC devices, further extending Moore's Law [3,4].

However, due to the low Curie temperature (T_c) of 2D magnets, these 2D spintronic devices cannot meet the temperature requirements in the industry field. Although some external methods can be used to enhance the T_c of 2D magnets [5-9], most of these methods lack the necessary conditions for large-area, easy-controllability, and high efficiency, which are important for industry field. Interfacial effect is considered an efficient method to controlling 2D magnetism[10]. Due to their low-dimensional characteristics, 2D materials are highly sensitive to external manipulation. Therefore, by constructing 2D heterostructures and introducing interfacial effects, effective control can be achieved over the magnetic[11-14], electrical[15,16], and optical properties[17] of 2D materials. Topological insulators, which also possess a layered structure, are important candidates for realizing novel spintronic devices due to their various efficient spin manipulation properties [18-21]. Moreover, due to their unique layered structure, they can be combined with various 2D magnets easily to form 2D magnetic topological heterostructures[22-24]. These heterostructures combine the advantages of 2D magnets and 2D topological insulator materials, allowing for control of the magnetic properties and spin-related effects of the heterostructures through interfacial effects, which hold great scientific research and industrial value.

In this chapter, we will first provide a brief introduction to spintronics and spintronic devices, leading to the two research objectives of this thesis: 2D magnets and topological insulators. We will then briefly discuss the generation mechanism of 2D magnetism and its manipulation methods. Compared to the external control methods, the interfacial effects have advantages such as large area, simple fabrication process, and high efficiency. The study on the interfacial magnetism manipulation is expected to achieve 2D magnets with higher T_c and tunable magnetic anisotropy.

1.1 Introduction to spintronics

1.1.1 Magnetism and electron spin

In 1820, Danish scientist Hans Christian Ørsted discovered the magnetic effect of electric current, establishing the connection between electricity and magnetism for the first time. 100 years later, with Paul Dirac's formulation of relativistic quantum mechanics in 1928, people began to recognize the role of electron spin and magnetic moment, which provides an explanation for the origin of material magnetism. Taking ferromagnetic materials as an example, their magnetism arises from the spin-split energy band structure caused by the exchange interaction between electrons. As shown in Figure 1a, on this split energy band, the electron density of states and conductivity differ for different spin orientations, which is the source of spin-dependent scattering. The concept of spin-dependent scattering was initially proposed by Mott to explain the anomalous resistance behavior of ferromagnetic metals near the T_c, based on the foundation of the two-current model (as shown in Figure 1b)[25]. In the two-current model, the conduction current is phenomenologically divided into two parallel transport states, representing two paths for spin-up and spin-down, each with different distribution functions and relaxation times. Due to the spin-split energy bands in ferromagnetic materials, specific spin electrons may occupy the partially filled *d* electron states. These electrons have a shorter mean free path, resulting in strong scattering effects and high resistivity, while the other spin state electrons in the partially filled shell experience less scattering and exhibit lower resistance. The two-current model laid a solid physical foundation for the development of spintronics, establishing a direct connection between electron transport and electron spin.

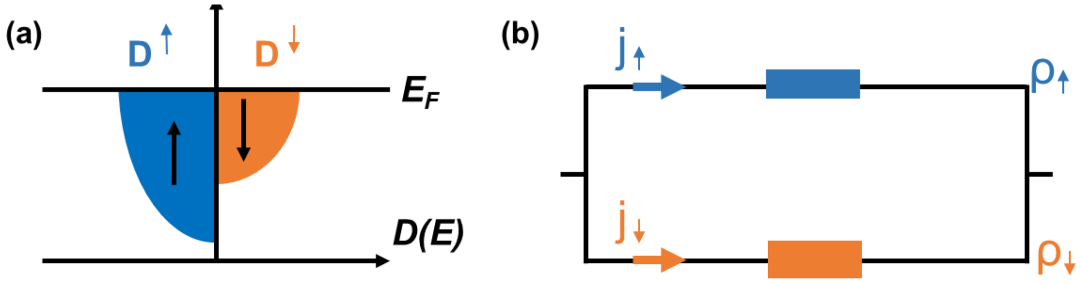

Figure 1. Two-current model of spintronics.

In the late 20th century, rapidly advancing nanofilm fabrication technologies provided the technical foundation for the development of spintronics. Micro and nanofabrication techniques allowed us to precisely control the growth of ferromagnetic metal films at the nanoscale. In 1986, a team led by Peter Grünberg discovered a significant magnetoresistance effect in Fe/Cr/Fe trilayer heterostructures[26]. The magnetoresistance value could reach as high as 1.5% even at room temperature. In the same year, a team led by Albert Fert at the University of Southern Paris independently observed a remarkably high magnetoresistance up to 50% in Fe/Cr multilayer superlattice samples, with a magnetoresistance value as high as 17% even at room temperature. The antiferromagnetic coupling between the Fe/Cr layers caused the magnetic moments of adjacent ferromagnetic layers to spontaneously align in an antiparallel configuration. When an external magnetic field causes the magnetic moments of the ferromagnetic layers to align in parallel, the resistance of the heterostructure undergoes a significant change[27] (as shown in Figure 2). Fert named this effect giant magnetoresistance (GMR). The discovery of the GMR effect revealed the connection between electron spin and electron transport and demonstrated that the transport properties of charge (i.e., resistance) can be altered by applying a magnetic field to manipulate spin. This discovery paved the way for exploring methods of information writing through spin manipulation, leading to a hot research in the field of storage and driving a technological revolution in the storage industry. In 2007, the Royal Swedish Academy of Sciences awarded the Nobel Prize in Physics to Albert Fert and Peter Grünberg to honor their outstanding contributions to the discovery of the GMR effect.

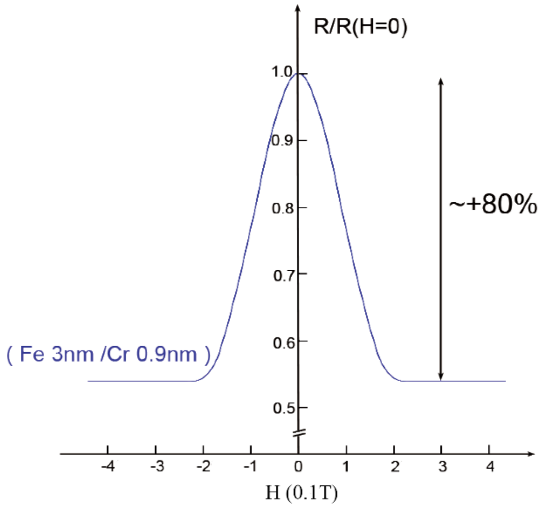

Figure 2. Giant magnetoresistance effect of Fe/Cr multilayer films[27].

1.1.2 Spintronic devices

As the research on spintronics deepening, various functional spintronic devices have been developed, such as spin memory devices, spin logic devices, and spin computing devices. In the future, spintronic devices have the potential to replace some semiconductor devices and become the key technology for the next generation of ultra-low power consumption storage and computing circuits.

Spin Memory Devices: In 1991, IBM utilized the giant magnetoresistance (GMR) effect to design spin valve-based magnetic heads[28]. In 1995, high-capacity hard drives based on this design were commercialized by IBM, triggering a revolution in the hard drive industry. Over the course of a decade (1997-2007), the storage capacity of hard drives increased by over 1000 times, and this enormous market growth gave rise to world-class companies such as Seagate and Western Digital. The discovery of the room-temperature tunnel magnetoresistance (TMR) effect in the magnetic metal/insulator/magnetic metal trilayer structure, known as the magnetic tunnel junction (MTJ), in 1995 further propelled the emergence and development of magnetoresistive random-access memory (MRAM)[29,30]. MTJ structures with a magnetoresistance value exceeding 230% directly contributed to the advancement of MRAM[31]. MRAM based on the TMR effect offers significant advantages in terms of read/write speed, scalability, and rewritability, positioning it as one of the promising emerging non-volatile memory technologies that could replace existing semiconductor memories (as shown in Figure 3). Additionally, MRAM primarily consists of ferromagnetic metal materials, utilizing their magnetization states to store information. Unlike charge, the spin property of electrons is not influenced by high-energy particles generated by the atmosphere or electromagnetic weapons. As a result, MRAM exhibits natural resistance and immunity to radiation and interference, making it highly significant for the informatization of aerospace systems.

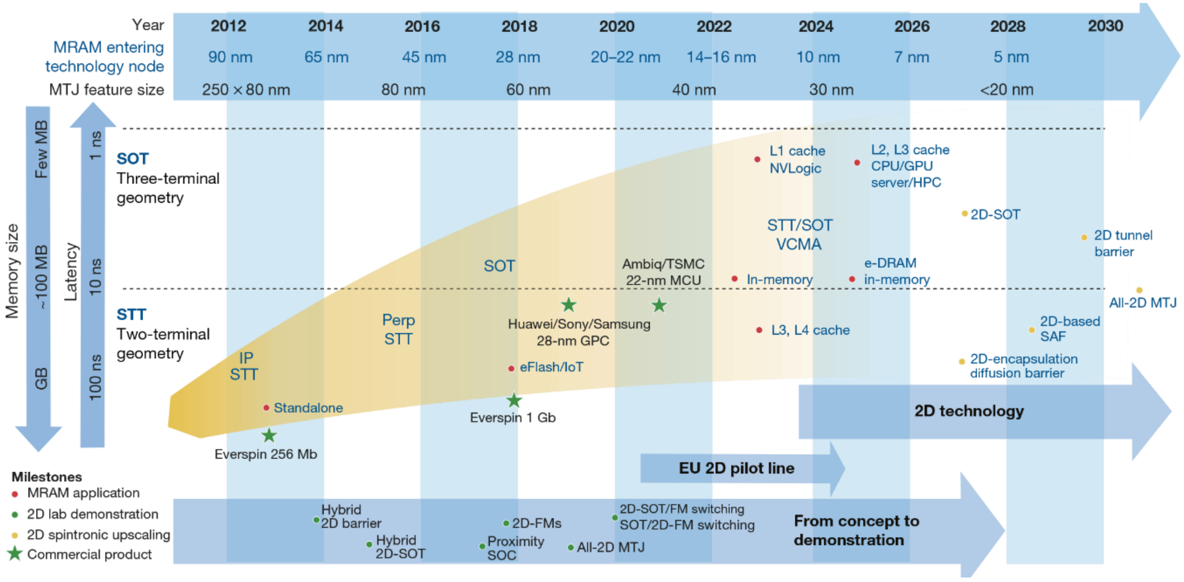

Figure 3. Technology Development Roadmap of MRAM [32].

Spin Logic Devices: Spin logic offers the advantage of non-volatility and enables circuits with instant on/off functionality. In 2005, Russell Cowburn *et al.* of the University of Cambridge proposed a spin logic device based on the motion of magnetic domain walls in magnetic wires[33]. When the magnetization direction of the magnetic wire aligns with the direction of domain wall motion, the logic value is "1"; when they are opposite, the logic value is "0". This was the first integration of electron spin characteristics into logic computation, opening a new door for achieving ultra-low power logic computing in the future. In 2010, Supriyo Datta of Purdue University introduced the concept of all-spin logic[34]. This model utilizes lateral spin valves to accomplish data storage and processing through the injection, transport, and detection of pure spin currents. Due to the absence of charge transfer, spin logic devices can significantly reduce power consumption. However, the above achievements are currently limited to fundamental theory and material exploration, and research on device fabrication processes is still ongoing. Designing spin logic devices with high stability and strong controllability based on the spin properties of electrons remains a challenging task that needs to be addressed.

Spin Computing Devices: Spin computing devices have the following advantages: non-volatility; low energy consumption; larger storage capacity[35]. Currently, spin computing devices that utilize electron spin as the information carrier are under development, such as instant ON/OFF circuits, approximate computing devices, logic-in-memory devices, and neuromorphic devices. These spin computing devices have advantages in processing complex real-time data and are gradually being applied in fields such as artificial intelligence and deep learning. However, many concepts related to spin information processing remain at the theoretical level, and numerous key technologies are awaiting breakthroughs.

1.2 Two-dimensional magnets and topological insulators

With the development of nanofilm fabrication processes, traditional methods of improving integration density through process optimization are no longer applicable. This is because at the sub-nanometer scale, traditional three-dimensional materials cannot maintain their original physical properties[36]. 2D materials, characterized by their layered structures, can preserve excellent physical properties at the atomic level due to their unique van der Waals interface. The discovery of graphene in 2004 sparked the exploration of 2D materials[37,38]. Currently, approximately 700 types of 2D materials have been experimentally or theoretically confirmed. These 2D materials encompass a wide range of properties, including insulators, semiconductors, semimetals, metals, and even superconductors. The diversity of their physical properties confirms the enormous potential of 2D materials to replace traditional three-dimensional materials[39].

In the field of spintronics, although the discovery of intrinsic 2D magnets came later, the spin properties of some 2D materials (such as the strong spin-orbit coupling effect in topological insulators) have been widely studied and are being utilized in the spintronic devices. With the development of fabrication processes, a large amount of intrinsic 2D magnets have been discovered. Due to their low-dimensional nature, the spin properties of 2D magnets are highly sensitive to external manipulation. It has been found that by forming heterostructures with topological insulators, the strong spin manipulation of topological materials and the interface sensitivity and tunability of 2D magnets can be fully utilized, which enables efficient control of the spin and magnetic properties of heterostructures through the interfacial effects[17,22-24]. Therefore, the study of 2D magnets, topological insulator materials, and the magnetism manipulation introduced by the interfacial effects in the heterostructures is of great significance for realizing novel spin devices, particularly high-density magnetic storage devices and high-performance quantum devices. In this section, we will provide a brief introduction to the properties of these two types of materials.

1.2.1 Two-dimensional (2D) magnets

Two-dimensional (2D) magnets are a relatively young member in the 2D family. In 1955, Mermin and Wagner theoretically proved that long-range magnetic order is impossible in the 2D Heisenberg model at finite temperature, which was called M-W theory[40]. As a result, for a long time, the scientific community did not believe that 2D magnets could exist. It wasn't until 2017 when Zhang Xiang *et al.* of the University of California, Berkeley, successfully prepared few-layer $Cr_2Ge_2Te_6$ thin films through mechanical exfoliation and characterized their magnetic properties using magneto-optical Kerr effect[41]. This was the first experimental confirmation of the existence of intrinsic 2D magnets. $Cr_2Ge_2Te_6$ is a magnetic semiconductor, which means its electrical and magnetic properties can be controlled by an electric field, making it a good candidate for novel 2D spintronic field-effect transistors[42]. Subsequently, Xiaodong Xu *et al.* successfully prepared a 2D antiferromagnetic material, CrI_3[5]. Similarly, they characterized the magnetic properties of CrI_3 by magneto-optical Kerr technology and confirmed the interlayer antiferromagnetic coupling in CrI_3. These discoveries demonstrated that long-range magnetic order in 2D magnets can exist stably at finite temperatures. It's important to note that this does not mean the M-W theory is incorrect. In the next section, we will demonstrate through theoretical discussion that the presence of magnetic anisotropy in 2D magnets breaks the continuous symmetry in the Hamiltonian, allowing for the stable existence of magnetism in the 2D system.

Through relentless efforts, long-range magnetic ordering phenomena have been observed in various 2D materials (as shown in Table 1). Currently, different 2D magnets with distinct magnetic and electrical properties can be obtained to meet the requirements of different devices. For example, there are ferromagnetic (FM) 2D materials such as Fe_3GeTe_2[43-46], $CrSe_2$[47], $CrGeTe_3$[41] and antiferromagnetic (AFM) 2D materials including Cr_2S_3[48], CrI_3[49], $CrBr_3$[50], $CrCl_3$[51], $FePS_3$[52], $NiPS_3$[53], etc. One of the most important tasks in this field is to achieve control over the magnetic properties of 2D magnets, such as Curie temperature (T_c) and magnetic anisotropy, to meet the demands of spin devices for high operating temperatures and thermal stability. Various control methods have been developed to achieve higher-temperature 2D magnets, including carrier doping, interlayer stacking control, and strain engineering. However, each of these methods has its limitations and it remains challenging to achieve easily-controlled and high efficiency magnetic modulation. Furthermore, the existing methods were designed for the sample prepared by mechanical exfoliation methods, which neglects the "interfacial effect" in the 2D materials. The latter is considered an important means of achieving magnetic control in mechanical exfoliation methods systems (as shown in Figure 4).

Among them, the 2D topological ferromagnetic heterostructure is considered an excellent system for studying such interfacial effects. Due to the strong spin-orbit coupling and rich spin-related effects of topological insulators (TI), when they are combined with 2D magnets to form heterostructures, it is expected to achieve efficient control of the spin and magnetic properties through the interfacial effects.

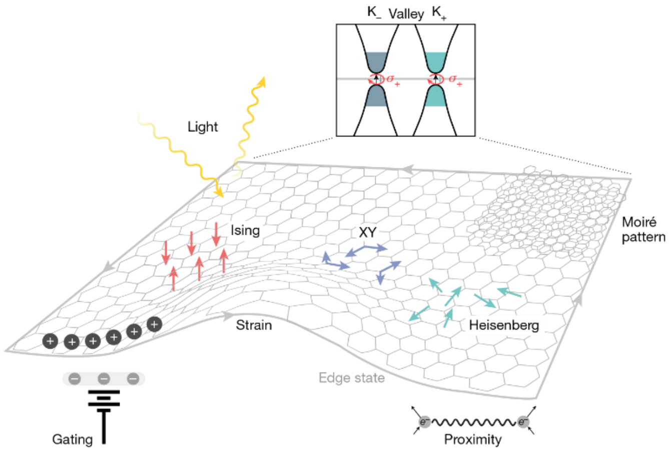

Figure 4. Interface effects in magnetic two-dimensional materials[10]

Table 1. Some experimentally confirmed 2D magnets

Materials	Conductivity	Magnetic order	Magnetic anisotropy	Magnetic transition temperature (K)
$CrCl_3$[51]	Insulator	AFM	*weak*	14 (T_N)
		FM		17 (T_c)
$CrBr_3$[50]		FM	*c*	34
CrI_3[49]		AFM	*c*	45
		FM		
VI_3[54]	Semiconductor	FM	*c*	50 (bulk)
Fe_3GeTe_2[43-46]	Metal	FM	*c*	130 (1 L)
				220 (>4 L)
Fe_4GeTe_2[55-57]			*ab*	280
$CrSe_2$[47]	Metal	FM	*c*	65 (1 L)
				110 (16 L)
$CrTe_2$[58]			*c*	200 (1 L)
				300 (>7 L)
VSe_2[59]			*ab*	330 (1 L)
Cr_2S_3[48]	Semiconductor	AFM	*ab*	120 (15 nm)
				300 (45 nm)
CrSe[60]	Metal	FM	*c*	280
$MnBi_2Te_4$[61]	Topological insulator	AFM	*c*	18 (few layer)
		FM		25 (bulk)
$FePS_3$[52]	Insulator	AFM	*c*	104 (1 L)
$NiPS_3$[53]			*ab*	25 (1 L)
				130 (2 L)
				155 (bulk)

$CrGeTe_3$[41]	Insulator	FM	*weak*	30 (2 L)
			c	61 (bulk)
α-$RuCl_3$[62]	Insulator	AFM	*c*	--

1.2.2 Topological insulator

Compared to the 2D magnets, topological insulator (TI) materials have a longer history. Group-VI-V bismuth telluride-based compounds (such as Bi_2Te_3, Sb_2Te_3, Bi_2Se_3 etc.) are typical examples of topological insulator materials[63]. Similar to graphene, topological insulators also have a layered structure, with each layer connected by van der Waals gap. The single-layer topological insulator consists of a quintuple layer (QL) composed of five atomic layers, with each layer having a thickness of approximately 1 nm. Figure 5a illustrates the crystal structure and band structure of the topological insulator Bi_2Se_3 [64], which belongs to the hexagonal crystal system with a space group of D_{3d}^{5}.

Unlike traditional insulating or conducting materials, TIs are insulating in the bulk while exhibiting conducting metallic states on their surfaces, as shown in Figure 5b. This unique band structure imparts various fascinating spin-related effects to topological insulator materials. One of the most important characteristics being "spin-momentum locking," where the spin is locked to its momentum direction on the TI's surface states. As shown in the *E*-*k* band diagram (Figure 5b), the band inversion resulting from spin-orbit coupling gives rise to the topological surface states in the bulk band gap, forming a Dirac cone at the Γ point. Unlike the spin-degenerate bulk bands, the two surface states on the Dirac cone are highly spin-polarized, with electron spins perpendicular to the *E*-*k* plane and opposite polarization directions on different surface states. Under the protection of time-reversal symmetry, when the momentum of the surface state electron changes from *k* to -*k*, its spin direction also changes correspondingly. Therefore, this spin-polarized surface exhibits a high spin-charge conversion effciency. Due to the spin-momentum locking effect, electrons with a specific spin on the surface of a TI thin film can only move in one direction along the sample's edges, preventing backscattering to quantum states moving in the opposite direction (i.e., backscattering is prohibited), similar to the characteristics of superconductors. This feature can be utilized in electronic devices to reduce energy loss during electron transport [65].

Due to the efficient spin manipulation characteristics of topological insulators, they have been widely utilized in various spintronic devices, such as topological quantum devices and topological superconducting devices. In the past, the scientific community often introduced ferromagnetism into topological insulators through magnetic doping to study the spin-related effects in TI[66-70]. In 2013, Qikun Xue *et al.* at Tsinghua University demonstrated that the time-reversal symmetry (TRS) in 2D topological insulators could be broken through magnetic doping, leading to quantum anomalous Hall effect (QAHE)[65]. This discovery is of great significance and provides possibilities for developing a new generation of ultra-low-power and high-speed spintronic devices. However, the magnetism introduced by magnetic doping can only exist at extremely low temperatures (30 mK), far from meeting the requirement for device operation at room temperature. Alternatively, the magnetism could be introduced into TI by the magnetic proximity effect, where the magnetic elements from adjacent ferromagnetic materials are coupled with the TI surface states through exchange interactions. Consequently, a magnetism introduction or enhancement could be achieved in TI[71-74].

The magnetic proximity effect arises from the strong spin-orbit coupling in TI. As an interfacial effect, the magnetic proximity effect has been recognized as one of the effective methods to achieve magnetism generation and manipulation, particularly in the field of 2D materials. Since TI also has a 2D layered structure without surface dangling bonds, it is possible to create a well-defined vdW interface by stacking the 2D magnetic thin film onto a TI thin film, hereby realizing the magnetic proximity effect. Moreover, due to the strong spin-orbit coupling in TI, various novel spin-related effects can emerge at the interface of the 2D topological magnetic heterostructures, such as topological superconductivity[15,16,75] and spin-exchange interactions[24,76]. Previous studies have demonstrated that the formation of 2D magnetic topological heterostructures can effectively control the magnetic properties of 2D magnets.

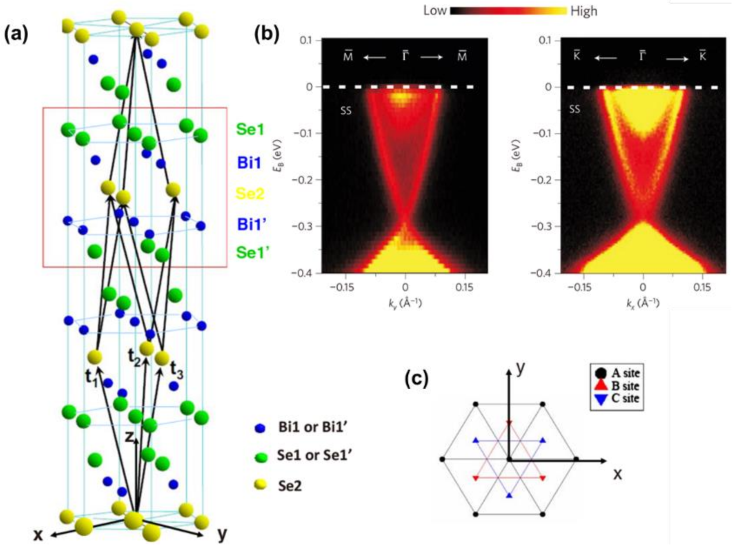

Figure 5. Crystal Structure and Band Structure of Topological Insulator Bi_2Se_3[64]

1.3 The mechanism of 2D magnetism

Like 2D magnets, the long-range magnetic moments in 2D magnets also arise from the exchange interactions between magnetic atoms. Based on the orientation of spins in neighboring magnetic sites, these magnetic materials can be classified into Heisenberg, Ising, and XY models. Here, we will first introduce the Heisenberg model. When considering only the spin exchange interactions within the magnetic material, the Hamiltonian of the Heisenberg model can be expressed as [77]:

$$H = \sum_{ij} J_{ij} S_i \cdot S_j \tag{1.1}$$

Here, J represents the magnitude of the exchange interaction between magnetic atoms, S represents the spin of the magnetic atoms, and the subscripts i and j denote the positions of any two magnetic atoms in the material's crystal structure. The summation term represents the non-redundant sum over all spin exchange interactions between atoms. In order to simplify this model, we often consider only the interactions between nearest neighboring sites in the structure, assuming the exchange interaction to be a constant J. In this case, Eq (1.1) can be simplified as:

$$H = \sum_{\langle i,j \rangle} J S_i \cdot S_j \tag{1.2}$$

Obviously, when $J>0$, the spins of all atoms in the material align parallel to each other, resulting in ferromagnetic behavior. On the other hand, when $J<0$, the spins of all atoms align antiparallel to each other, leading to antiferromagnetic behavior. Furthermore, if we express Eq (1.2) in the Cartesian coordinate system, the Hamiltonian becomes:

$$H = \sum_{\langle i,j \rangle} J_x S_i^x S_j^x + J_y S_i^y S_j^y + J_z S_i^z S_j^z \tag{1.3}$$

In this case, J_x, J_y, J_z represent the components of the exchange interaction J in the x, y, and z directions, respectively, and S_i^x, S_i^y, S_i^z represent the components of the spin S of any magnetic atom in the spaces. For the Heisenberg model, it is evident that all components of J in three-dimensional space are nonzero, i.e., $J_x \neq 0$, $J_y \neq 0$, $J_z \neq 0$. This means that the spins of magnetic atoms in the material can point in any direction in three-dimensional space, resulting in a spin dimensionality of 3. When the z-component of J is zero, i.e., $J_x \neq 0$, $J_y \neq 0$, $J_z = 0$, the exchange interaction in the system becomes the XY model, where the spins of magnetic atoms in the material can point in any direction within the plane, resulting in a spin dimensionality of 2, and the sample exhibits in-plane magnetic anisotropy. When both the x and y components of J are zero, i.e., $J_x = 0$, $J_y = 0$, $J_z \neq 0$, the exchange interaction in the system becomes the Ising model, where the spins of magnetic atoms in the material can only point in the up or down direction, resulting in a spin dimensionality of 1. Clearly, in this case, the sample exhibits perpendicular magnetic anisotropy. It is worth noting that for 2D materials, an additional magnetic anisotropy term is often added in Eq (1.1).

$$H = \sum_{ij} J_{ij} S_i \cdot S_j + \sum_i A(s_i^z)^2 \tag{1.4}$$

Here, A represents the single-ion perpendicular magnetocrystalline anisotropy energy (SIA) arising from the spin-orbit coupling in the material. It is evident that for the Heisenberg model, the presence of magnetic anisotropy breaks the continuous symmetry of the Hamiltonian. Therefore, magnetic anisotropy is a necessary condition for the existence of long-range magnetic order in 2D magnets.

1.4 2D magnetism manipulation by external stimuli

In Eq (1.4), the spin exchange interaction J includes various types of exchange interactions among the *3d* electrons of magnetic atoms, including direct exchange, indirect exchange, and superexchange, etc. The interplay between these different exchange interactions, along with the presence of magnetic anisotropy arising from spin-orbit coupling, allows for the control of the magnetic properties of 2D materials through external stimuli (such as gate voltage, electrostatic doping, ion intercalation, strain, etc.). This further expands the application potential of 2D magnets. Some common methods for magnetism manipulation include the following:

Carrier concentration control: In the Anderson model, the spin exchange interactions in magnetic materials can be described by a function involving the Fermi level (E_F) and the energy level of localized states (E_d), which directly depend on the carrier concentration [78,79]. It is evident that by controlling the carrier concentration, the ferromagnetic properties of 2D magnets such as T_c and magnetic anisotropy, can be directly manipulated. Various methods can be used to adjust the carrier concentration, including gate voltage[5,6,80,81], ion intercalation[46,82], and laser pumping[9].

Interlayer stacking control: Previous studies have demonstrated that controlling the interlayer stacking arrangement enables the modulation of magnetic coupling properties in 2D magnets. Taking CrI_3 as an example, bulk CrI_3 crystal exhibits two magnetic coupling phases: an antiferromagnetic coupling phase at high temperatures with a monoclinic crystal structure, and a ferromagnetic phase at temperatures below 220 K with a low-temperature rhombohedral crystal structure. Therefore, the interlayer stacking arrangement of CrI_3 can be altered by physical manipulation[7] or hydrostatic pressure[83,84] to modify its magnetic ground state. Similar control methods have also been reported for materials such as $Cr_2Si_2Te_6$[85], $MnPS_3$[86], $CrBr_3$[87].

Strain engineering control: According to Eq (1.1), the long-range magnetic order in magnetic materials depends on the magnitude of the exchange interactions among magnetic atoms. Strain engineering can enhance the magnetic exchange interactions in materials, thus directly controlling their magnetic properties. Early theoretical work has predicted that by introducing stress in the crystal structure, the magnetic properties of CrI_3 can be induced to transition between ferromagnetic and antiferromagnetic states[88,89]. Theoretical and experimental studies on $Cr_2Ge_2Te_6$[90] and Fe_3GeTe_2[8,91] have also confirmed that even slight structural strain can significantly increase the T_c of 2D magnets.

1.5 Interfacial manipulation of 2D magnetism

The discussion above confirms that the magnetic properties of 2D materials can be controlled through external methods. However, the methods used to enhance the magnetism through external stimuli do not possess the necessary conditions for industrial-scale implementation, such as large-area coverage, controllability, and high efficiency. Moreover, previous research on 2D magnets mostly relied on the samples prepared by mechanical exfoliation, which hinders large-scale wafer-level fabrication and subsequent material processing. Furthermore, mechanical exfoliation discards the "interfacial effect" of 2D materials, which are considered crucial for achieving efficient control over their magnetic properties. Due to their low-dimensional nature, 2D materials exhibit high sensitivity to external manipulation. Therefore, by constructing 2D heterostructures and introducing interfacial effects, the magnetic, electrical, and optical properties of 2D materials can be effectively controlled. Compared to traditional methods, utilizing interfacial effects to control the magnetism in the epitaxial thin films offers various advantages, such as large-area coverage, simplicity in structure, and high control efficiency. Moreover, this approach is compatible with patterning process in the modern semiconductor industry.

Interfacial effects include proximity effect[22,23,71,92-94], exchange interaction[11-14,24], charge transfer[95], strain modulation[96,97], etc. They all have advantages such as large effective area, no external assistance required, and ease of implementation, making them commonly used for magnetism manipulation in 2D heterostructures. Both proximity effect and exchange interaction arise from the spin-orbit coupling at the interface, which influences the electronic density of states and results in a magnetism manipulation. Proximity effect can induce long-range magnetic moments in 2D topological insulators, leading to topological phase transitions, which serve as the foundation for constructing topological quantum devices. In 2D magnetic films, exchange interaction enhances the spin interactions in the system, tunning its magnetic properties of the film consequently, such as magnetic anisotropy or T_c. Charge transfer, similar to voltage or laser modulation discussed in Section 1.4, controls the electronic structure of 2D materials. Since the electronic structure directly determines the magnetism in ferromagnetic materials, charge transfer can effectively control the magnetic characteristics of 2D magnets. Compared to charge transfer and strain modulation, proximity effect and interfacial exchange are more operable and have been widely reported in experiments. Therefore, this thesis primarily focuses on these two interfacial effects.

1.5.1 Interfacial spin-orbit coupling

For the interfacial proximity effect and exchange interaction, both of them originate from the spin-orbit coupling (SOC) in the material. Therefore, before discussing the magnetism manipulation effects at the interface, we should explore the origin of SOC effects. Spin-orbit coupling arises from the interaction between the electron's spin and its orbital angular momentum, where spin is an intrinsic property of the electron, and orbital angular momentum arises from the electron's motion around the atomic nucleus. The electron moves around the nucleus, which generates a magnetic field and in turn exerts a force on the atomic nucleus. Although there is no magnetic field acting on the electron in the reference frame of the stationary nucleus, when we consider the electron as the reference point, the atomic nucleus can be seen as producing an equivalent field on the electron, which we call the spin-orbit coupling magnetic field ($\boldsymbol{B_{SO}}$). According to the theory of special relativity, the magnitude of $\boldsymbol{B_{SO}}$ can be expressed as:

$$\boldsymbol{B}_{SO} = (1/c^2)\boldsymbol{E}\times\boldsymbol{v} \tag{1.5}$$

Where v represents the velocity of the electron, c is the speed of light, E denotes the electric field generated by the atomic nucleus at the electron's position, and its magnitude is $E = \boldsymbol{Zer} / 4\pi\varepsilon_0 r^3$. In this equation, Z is the atomic number of the nucleus, e is the elementary charge, ε_0 is the vacuum permittivity, and r represents the electron's position (i.e., the orbital radius). According to the definition of orbital angular momentum $\boldsymbol{L} = \boldsymbol{r}\times\boldsymbol{P}$, $\boldsymbol{P} = m_0\boldsymbol{v}$ (where $\boldsymbol{P}$ is the momentum of the electron and m0 is the mass of a free electron), the magnitude of $\boldsymbol{B_{SO}}$ can be expressed as:

•

$$B_{SO}=(Ze\,/\,4\pi\varepsilon_0 r^3 m_0{}^2 c^2)\boldsymbol{L} \tag{1.6}$$

For an electron with a spin magnetic moment of μ_S, the magnitude of its magnetic moment can be expressed as $\mu_s = \text{-}g_s\mu_B\boldsymbol{S}$, where $\boldsymbol{S}$ is the electron's spin angular momentum, g_S is the spin quantum number (equal to 2), μ_B is the Bohr magneton, and its magnitude is $\mu_B = e\,/\,2m_0$. In this case, the potential energy of the electron under the influence of the coupling field $\boldsymbol{B_{SO}}$ is given by:

$$\mathrm{U} = \text{-}\boldsymbol{\mu}_{\mathrm{s}}\cdot\boldsymbol{B} = \frac{Ze^2}{4\pi\varepsilon_0\hbar r3c^2m_0{}^2}\boldsymbol{L}\cdot\boldsymbol{S} \tag{1.7}$$

From Eq (1.7), it can be observed that the magnitude of the spin-orbit coupling energy during the electron's motion around the atomic nucleus is positively correlated with the atomic number Z, which is why the SOC effect is stronger in heavy atoms. Recent experimental work has demonstrated that the SOC effect on the outermost electron of an atom is proportional to the square of the atomic number[98], which is consistent with the previous reports. Additionally, Eq (1.7) also shows that the potential energy experienced by an electron is dependent on its position (i.e., the electron's orbital radius r).

It is worth noting that the discussion above assumes that the atomic nucleus revolves around the electron in a circular motion. In reality, the atomic nucleus does not directly exert a force on the electron during its motion. Therefore, the spin-orbit coupling effect can be understood as the electron's orbital angular momentum generating an equivalent magnetic field, which acts on the electron's spin angular momentum. This is the physical origin of the SOC effect. The SOC effect serves as the foundation for various spin-related phenomena such as spin precession, spin Hall effect, and magnetic anisotropy, revealing the relationship between electron spin and electron orbit. Research on the SOC effect holds the promise of achieving efficient spin manipulation and developing more advanced spintronic devices.

1.5.2 Proximity effect

Previous studies have demonstrated that combining TI thin film with magnetic film to form heterostructures can achieve magnetism generation and enhancement in TI through the magnetic proximity effect at the interface. S. V. Eremeev *et al.* theoretically proved the existence of the proximity effect at the interface of the heterostructure composed of the ferromagnetic insulator MnSe and the topological insulator Bi_2Se_3 using density functional calculations[99]. They suggested that charge redistribution and orbital coupling in MnSe/Bi_2Se_3 lead to a change in the interfacial electron structure, inducing a long-range ferromagnetic order. Furthermore, the introduced magnetism breaks the time-reversal symmetry of Bi_2Se_3, opening a gap in its surface states and potentially realizing the QAHE. This result was later experimentally confirmed by S. Moodera *et al.*[100]. They successfully obtained a topological phase with long-range ferromagnetic order by constructing the EuS/Bi_2Se_3 heterostructure and increased it T_c to 20 K. Subsequently, they achieved ferromagnetism exceeding room temperature in the same structure. Polarized neutron diffraction results showed that the combination with EuS can induce a stable long-range magnetic order in Bi_2Se_3, with a T_c exceeding 300 K[92]. In recent years, the proximity effect has been extensively studied as an important approach to achieving high-temperature QAHE in TI. Ferromagnetic insulators such as EuS[92], YIG[93], TIG[48], antiferromagnetic CrSb[71]， diluted magnetic semiconductor $Ga_{1-x}Mn_xAs$[94] have all been shown to exhibit proximity-coupling-induced high-temperature ferromagnetism when combined with TI thin films.

Most of the previous research on the proximity effect has focused on the system of 3D ferromagnetic materials and 2D topological insulators. By replacing the 2D ferromagnetic film in the heterostructure with a 2D material, one can achieve the interfacial effects in a completely 2D system. Soon after the discovery of TI, Kang L. Wang *et al.* confirmed the proximity effect in a 2D heterostructure $(Bi,Sb)_2Te_3$/Cr-$(Bi,Sb)_2Te_3$, as shown in Figure 6a. This proximity effect was proved to be able to tune the ferromagnetic order in Cr-$(Bi,Sb)_2Te_3$ layer[22]. In 2018, Y. Tokura *et al.* used the 2D magnetic insulator $Cr_2Ge_2Te_6$ and $(Bi,Sb)_2Te_3$ to create the first 2D magnetic/topological insulator heterostructure and studied the interfacial effect (Figure 6b). Due to the insulating nature of $Cr_2Ge_2Te_6$, they characterized the ferromagnetic properties of the TI later by anomalous Hall effect. The results demonstrated the presence of proximity-coupling effects at the interface, which introduce a stable ferromagnetic order in the TI layer[23].

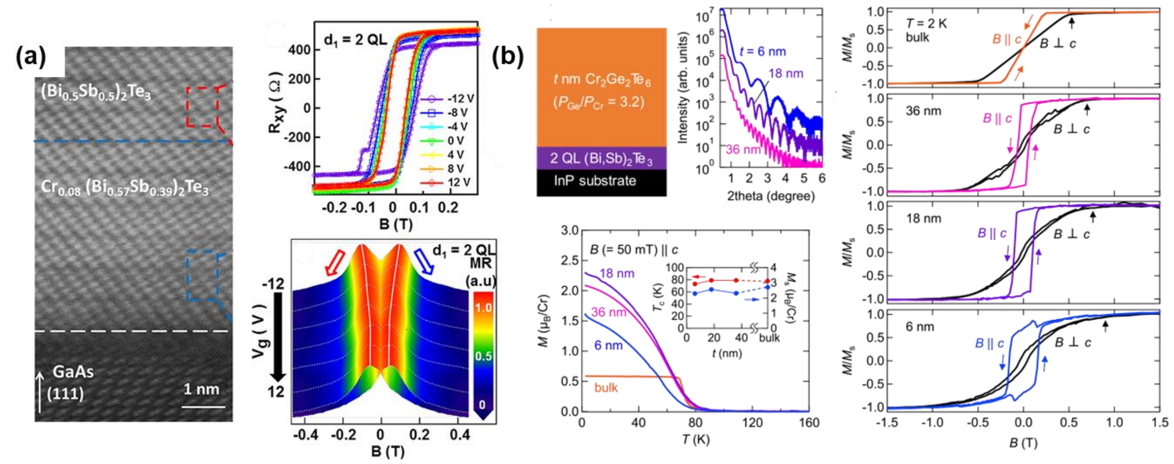

Figure 6. Proximity-induced magnetism in topological insulators-based heterostructures [22,23]

1.5.3 Interfacial exchange interaction

With the development of fabrication techniques for 2D materials, methods for producing large-area single-crystal ferromagnetic 2D materials have emerged. Due to the characteristics of 2D materials that do not require lattice matching, there is growing interest in designing 2D heterostructures to develop high-performance spintronics devices. In the previous section, we discussed the role of interfacial exchange coupling in introducing and enhancing magnetism in topological insulators. In fact, due to the strong spin-orbit coupling effects in TI, the interfacial exchange interaction can also affect the magnetic properties of the ferromagnetic layer. For example, in the EuS/Bi_2Se_3 heterostructure, the exchange interaction in EuS is significantly enhanced by the interface, leading to an increase in the heterostructure's T_c to 300 K[92]. In contrast, the original T_c of pure EuS films is only 20 K.

This interfacial exchange coupling can also enhance the magnetism in 2D magnets. Compared to the external manipulation methods such as electrostatic doping, interfacial exchange coupling does not require additional energy consumption. Xiufa Xian *et al.* from Fudan University constructed Fe_3GeTe_2/CrSb and Fe_3GeTe_2/MnTe heterostructures using molecular beam epitaxy techniques and utilized the exchange interaction between the ferromagnetic/antiferromagnetic interfaces to enhance the magnetism in the Fe_3GeTe_2

layer[11,12]. Magnetic characterization results demonstrated that the interfacial exchange coupling can effectively tune the T_c and magnetic anisotropy of Fe_3GeTe_2. In 2019, Wee *et al.* fabricated a monolayer VSe_2/Co heterostructure and measured the magnetic properties of VSe_2 using X-ray magnetic circular dichroism, confirming that the interfacial exchange coupling between Co and VSe_2 leads to the transition of VSe_2's magnetic coupling from ferromagnetic to antiferromagnetic[13]. In 2020, Junbo Han *et al.* prepared 2D magnetic films $FePS_3$ and Fe_3GeTe_2 by mechanical exfoliation and combined them into bilayer $FePS_3/Fe_3GeTe_2$ and trilayer $FePS_3/Fe_3GeTe_2/FePS_3$ heterostructures[14]. Subsequently, they characterized the magnetic properties of the two heterostructures using low-temperature magneto-optical Kerr microscopy, as shown in Figure 7. When combined with $FePS_3$, the magnetization of Fe_3GeTe_2 increases two times, and its T_c increased by 30 K, confirming the role of interface exchange coupling in controlling the 2D magnetism. Moreover, unlike the hysteresis loop of pure Fe_3GeTe_2, the $FePS_3/Fe_3GeTe_2$ heterostructure exhibited an obvious exchange bias feature, indicating that the interface exchange coupling in the heterostructure is similar to antiferromagnetic coupling.

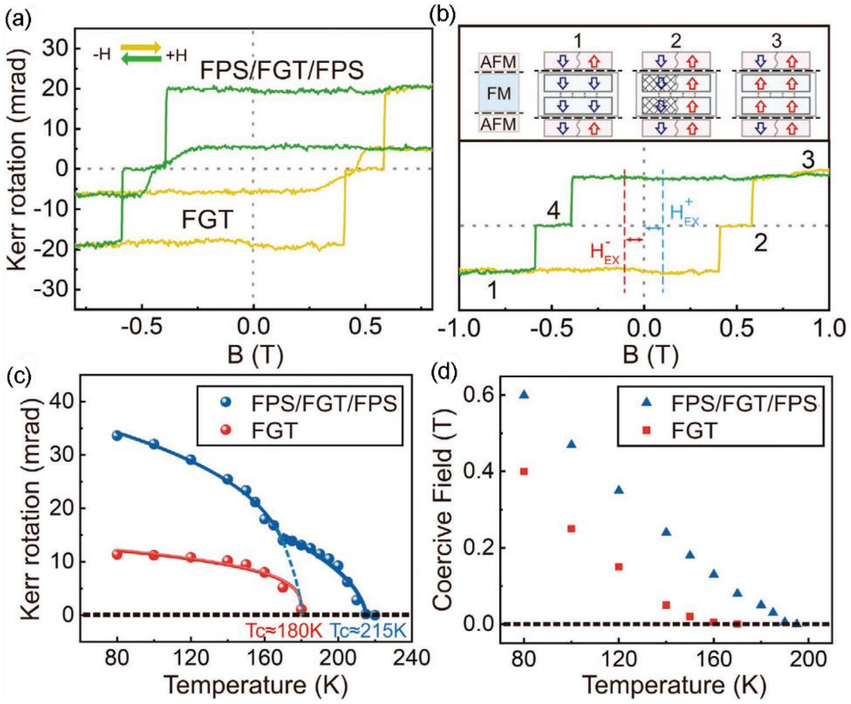

Figure 7. Magnetic manipulation of Fe_3GeTe_2 by interface exchange coupling[14]

In 2020, our research group prepared high-quality 2D magnet Fe_3GeTe_2 and 2D topological insulator Bi_2Te_3 by molecular beam epitaxy and combined them into a 2D heterostructure. A series of thickness-dependent characterization results revealed that the exchange couling at the heterostructure interface can raise the T_c of Fe_3GeTe_2 above room temperature[24], which is described in detail in Chapter 6 of this thesis. In summary, the aforementioned results confirm that the exchange coupling at the 2D interface is an important method to manipulate the 2D magnetism, providing insights for the future development of spintronic devices based on 2D magnets.

1.6 Main work and content arrangement of the thesis

The structure of this thesis is as follows:

Chapter 1 provides an introduction, starting with spintronics and briefly introducing the origin and various spintronic devices, highlighting the significance of spintronic materials in modern integrated circuits. It then introduces the two main research systems of this thesis: 2D magnets and topological insulators. The generation and manipulation mechanisms of 2D magnetism are systematically discussed.

Chapter 2 introduces the preparation and characterization methods used in this thesis and provides a brief overview of the equipment involved. Based on their functions, these equipment can be divided into three categories: material preparation equipment, morphology and crystal structure characterization equipment, and magnetic and electrical properties characterization equipment.

The main content of Chapter 3 is the epitaxial preparation and doping modulation of 2D magnet FGT (including Fe_4GeTe_2 and Fe_3GeTe_2). After obtaining high-quality thin films, we establish a Heisenberg model based on the RKKY exchange interaction to describe the magnetism in FGT. Based on this model, a method for enhance the T_c through magnetic doping is proposed. Using this method, we discovered three 2D ferromagnetic phases in Fe_4GeTe_2 and investigate the magnetic properties of Fe_4GeTe_2 as a function of doping concentration through electrical and magnetic properties measurements.

Chapter 4 reveals the interfacial T_c enhancement in Fe_4GeTe_2. Through a series of thickness-dependent experiments, we confirm that the Fe_4GeTe_2/Al_2O_3 interface can significantly increase the T_c of Fe_4GeTe_2. Combining first-principles simulations and photoelectron spectroscopy, we theoretically and experimentally demonstrate that the movement of Fe *d*-electron localized states induced by orbital coupling at the interface is the reason for the increase in the T_c.

Chapter 5 focuses on the proximity-induced magnetism in topological insulator thin films. Firstly, we explore the growth of high-quality two-dimensional TI thin films (including Bi_2Se_3 and Bi_2Te_3). Based on this, we fabricate a heterostructures of Bi_2Se_3 and ferromagnetic semiconductor MnGe and utilize the magnetic proximity effect to introduce a long-range ferromagnetic order in Bi_2Se_3. Furthermore, by measuring the transport properties, we quantify the contribution of proximity effect on the topological surface states.

Chapter 6 is dedicated to the interfacial engineering of the magnetism in 2D magnetic/topological heterostructures. We construct a heterostructure of topological insulator Bi_2Te_3 and 2D magnet FGT, and demonstrate the interfacial magnetism manipulation through electrical and magnetic measurements. Finally, we employ terahertz techniques to study the magnetic properties of the heterostructures, confirming the interfacial enhancement of the T_c in FGT and elucidating the spin-charge conversion process on the 2D magnetic interface through terahertz time-domain spectroscopy.

Chapter 7 summarizes the entire content of the thesis and discusses the unresolved issues and directions for further research in the future.

Chapter 2. Preparation and Characterization of 2D Magnets

This paper mainly revolves three main contents: the preparation and magnetic property characterization of 2D magnet FGT (including Fe_3GeTe_2 and Fe_4GeTe_2); the preparation and characterization of the topological insulator/ferromagnetic semiconductor heterojunction Bi_2Se_3/Mn_xGe_{1-x}; the preparation and magnetic property characterization of the 2D magnetic topological heterostructure FGT/Bi_2Te_3. Each part of the experiment involves three aspects: the first part is sample growth by molecular beam epitaxy (MBE) system, during the growth, the deposition process was monitored by crystal oscillator and reflection high-energy electron diffraction (RHEED) in situ; the second part is the characterization of the morphology and crystal structure of the sample. After the growth, the sample quality is identified by X-ray diffraction (XRD), transmission electron microscope (TEM), atom force microscope (AFM) and other technologies; the third part is the characterization of the sample's magnetic and transport properties, after obtaining samples with specific parameters and good quality, the magnetic and electrical properties of the sample are characterized by vibrating sample magnetometer (VSM), superconducting quantum interference device (SQUID), magneto-optic Kerr effect (MOKE), physical property measurement system (PPMS) and other methods. Finally, the spin transport properties of the sample are studied using terahertz time-domain spectroscopy (THz-TDS). In this chapter, we will briefly introduce the equipment involved in the work.

2.1 Molecular beam epitaxy

The methods for preparing 2D materials can be divided into top-down and bottom-up approaches. Top-down methods include mechanical exfoliation, liquid phase exfoliation, etc., which could overcome the interlayer van der Waals forces through mechanical energy or thermal and transfer the exfoliated material to a substrate. Top-down methods are simple to operate and make it relatively easy to obtain the desired materials. However, samples prepared using exfoliation methods have low yields, small areas, poor reproducibility, and, most importantly, no control over the thickness of the samples. Therefore, they cannot be compatible with mainstream semiconductor pattern processes. In contrast, bottom-up methods primarily use intermolecular chemical reactions or interactive forces to directly grow the sample on the substrate. Although this method has higher equipment requirements, it can produce thickness-controllable, high-quality wafer-level 2D material films. A representative bottom-up method is molecular beam epitaxy (MBE) technology, which has gradually become the mainstream method for preparing 2D materials.

MBE is a common physical vapor deposition technique, typically performed under ultra-high vacuum conditions (pressure below 10^{-9} torr). The material is sublimated into a gas state by heating, then a molecular beam with a certain velocity is sprayed and deposited onto the surface of a substrate, leading to epitaxial crystal growth. MBE is currently one of the primary technologies in the field of material epitaxial growth, mainly used for the growth of 2D materials and heterostructures that require atomic level precision control. MBE technique is also the method used in this paper to prepare 2D materials. Figure 8 shows the schematic diagram of the Smart-100 system used in this paper. The system is mainly made of 306 stainless steel and includes two main chambers (a growth chamber and a loading chamber), a three-stage combined pump system (a mechanical pump, a molecular pump, and an ion pump), an epitaxial growth system (including effusion cells, sample heating stage, RHEED, crystal oscillator, etc.), and the corresponding equipment control system.

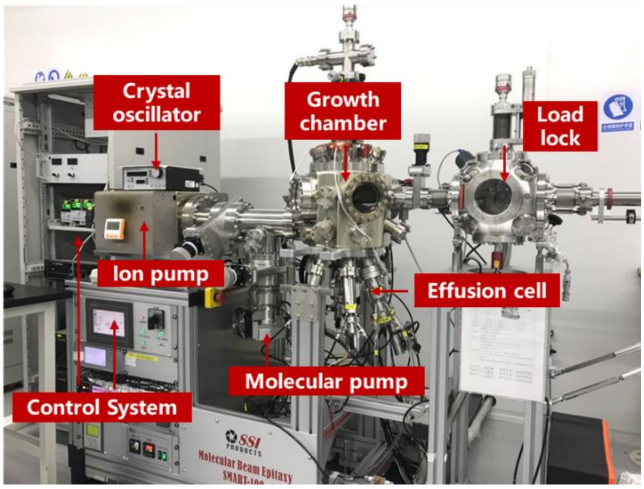

Figure 8. The Molecular Beam Epitaxy system used in this paper.

During the epitaxial growth process, the flux rate of the vapored material can be controlled by the temperature of effusion cell, then thin film with different composition could be obtained. Meanwhile, by controlling the growth time, the thickness of the thin film can be controlled. Molecular Beam Epitaxy has the following advantages: 1. Slow growth rate, enabling precise control of film thickness; 2. By precisely controlling the flux ratio between different sources, the composition and doping concentration of the film can be strictly controlled; 3. The crystal quality of the epitaxial material is high; 4. With crystal oscillator and RHEED, the epitaxial growth process can be monitored in real-time, and the process parameters of thin film growth can be optimized by analyzing the diffraction patterns to obtain high-quality thin films.

When using MBE to prepare materials, a constant current is first applied to the corresponding effusion cell, causing the material inside to be evaporated in the form of atoms or atom clusters. The evaporated materials are called "beam flux", which move in a straight line towards the substrate at a certain speed. Due to the ultra-high vacuum environment of the MBE system, the beam flux will not collide and scatter with impurity atoms during the movement, until it reaches the substrate location. When the beam flow collides with the substrate, the first adsorbed atoms or atom clusters will form nucleation sites on the substrate. The subsequent atoms deposit near the previous nucleation sites and gradually grow into a monocrystalline thin film by epitaxy.

In an ideal situation, epitaxial thin films are grown layer by layer. That is, during the epitaxy process, multiple single-crystal nuclei are first formed on the substrate, then the single-crystal nuclei expand and connect to form a single layer covering the entire substrate, and this process is repeated until the thin film is prepared (as shown in Figure 9a). However, in the actual growth process, due to the influence of external environments such as temperature, some atoms in the beam flow may not be able to reach the position with the lowest energy, causing the original layer-by-layer growth to become an island growth mode. As shown in Figure 9b, the island growth mode refers to the state where the atoms in the beam flux are adsorbed by the substrate, first forming three-dimensional island-like crystal nuclei with a certain thickness on the substrate, and then the island-like crystal nuclei grow and connect into rough polycrystalline films. Sometimes, the thin films prepared by epitaxy are not purely layer-by-layer growth or island growth, but a mixed growth mode of layer and island growth, as shown in Figure 9c. Under the mixed growth mode, the material shows a layer-by-layer growth mode at the initial few layers of thickness, and then becomes island growth. This is caused by the large lattice mismatch between the substrate and the growth material, resulting in stress inside the thin film. As the thickness of the thin film gradually increases, when the stress accumulates to a certain degree, the growth mode will change to island growth to release the stress.

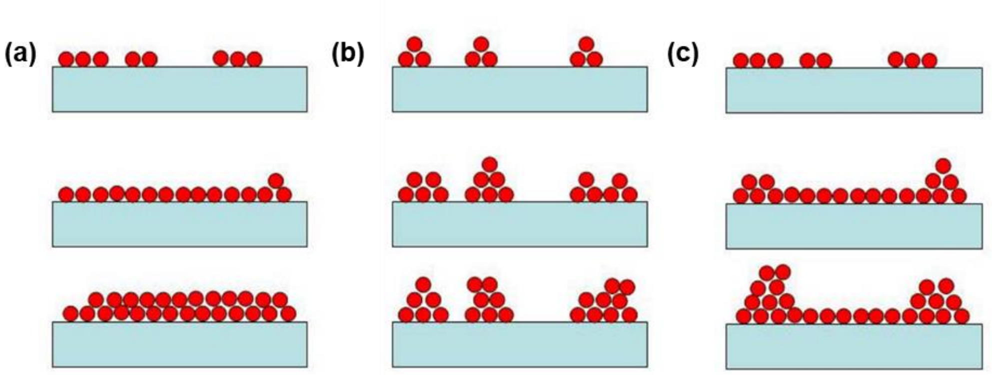

Figure 9. Three thin film growth modes: (a) Layer-by-layer growth (b) Island growth (c) Mixed growth

2.2 Morphology and crystal structure characterization equipment

During the epitaxial preparation process, it is necessary to use in-situ RHEED for real-time monitoring. Characterization methods for morphology and crystal structure, such as AFM, XRD, and TEM, are always used to perform microstructure and composition analysis on the sample. The characterization results will be analyzed to feedback the growth process, improving the growth conditions and obtaining higher-quality samples.

2.2.1 Reflection high-energy electron diffraction (RHEED)

Reflection high-energy electron diffraction (RHEED) is a real-time technique to characterize the surface morphology of epitaxial thin films. A high-energy electrons beam (about 20 keV) is slightly incident on the surface of the film at a small angle, due to the diffraction by the crystal lattice of the sample, the incident electrons will be diffracted and reflected to the detector to form regular diffraction fringes. By analyzing the temporal and spatial variations of the diffraction stripes, we can characterize the lattice constant, crystal quality, surface reconstruction process, and growth dynamics of the epitaxial thin film. As the incident angle of the high-energy electron beam is small and it can only penetrate a thickness of 1-2 nm on the surface. Therefore, the RHEED is regard as a surface characterization method for the epitaxial film.

The basic principle of RHEED is Bragg diffraction in real space, i.e., $n\lambda=2d\sin\theta$, where λ is the wavelength of the electron, d is the interplanar spacing of the sample to be tested, and θ is the angle of incidence. When the electron beam enters the ordered lattice, a path difference is generated on the reflections from adjacent crystal planes. When this path difference is an integer multiple of the wavelength of the electron beam, a diffraction enhancement phenomenon occurs. The type and spacing of the diffraction stripe pattern can be used to determine the crystal structure and lattice constant of the sample at this time. When sharp and bright linear stripes are observed, it indicates that the sample is in a 2D growth mode and has a flat single-crystal surface, then the lattice constant of the sample can be calculated through the stripe spacing. When the RHEED pattern is spotty, it indicates that the sample is in island growth mode. Although its surface is a single crystal, it is not smooth enough. When the pattern is ring-shaped, it proves that the sample is in polycrystalline growth mode, and the crystal structure and smoothness of the surface do not meet the experimental requirements.

2.2.2 X-ray diffraction (XRD)

X-ray diffraction (XRD) is a common tool used for the characterization of crystalline materials and is widely used to measure the thickness, lattice constant, internal strain, and composition of various semiconductor single crystals or 2D heterostructures. The basic working principle of XRD is also based on Bragg's Law, $n\lambda=2d\sin\theta$. Initially, the cathode ray tube in the XRD equipment produces X-rays of a specific wavelength that irradiate the sample. Due to the coherent interference of the incident light, there is a certain functional relationship between the wavelength of the X-ray and the diffraction angle and lattice spacing of the sample. Therefore, by analyzing the XRD results obtained, the crystal structure of the sample can be determined. However, since the wavelength of the X-ray is relatively short (0.01-10 nm), XRD has a deeper transmission depth compared to RHEED and can provide more information about the crystal structure inside the thin film. Theoretically, the XRD result of a single crystal sample should be periodically distributed lines, each line representing a diffraction peak of the crystal orientation. However, when there is stress or defects such as dislocations in the crystal, the strictly parallel crystal planes will have a slight deviation, leading to an increase in the width of the diffraction peak. Therefore, the two most intuitive parameters in the XRD results are the position of the diffraction peak 2θ and the Full Width at Half Maximum (FWHM) of the diffraction peak. The peak position reflects the crystal orientation and lattice constant of the sample, and the FWHM represents the quality of the sample's crystal quality. Moreover, the XRD spectrum of different single-crystal materials is unique, and the positions of their diffraction peaks can be found from the standard spectrum. Therefore, XRD can also be used for the qualitative analysis of the phase of unknown samples.

The XRD equipment used in this paper is the PANalytical X'Pert PRO MRD diffractometer (as shown in Figure 10), with an X-ray source of Cu Kα. The voltage and current of the X-ray generator are set to 45 kV and 40 mA respectively, the scanning range is from 10° to 90°, the scanning step is 0.03°, and the scanning speed is 20 seconds per step.

Figure 10. The XRD system PANalytical X'Pert PRO MRD used in this work.

2.2.3 Atomic force microscope (AFM)

Atomic force microscope (AFM) is a characterization technique that measures the surface of a sample through interatomic forces, achieving nanometer-level resolution of the sample surface morphology. By choosing different probes, it can also measure the physical properties of the sample surface (such as magnetic domain walls, etc.). The AFM has low requirements for the testing environment and sample quality and can measure samples like biological materials, liquids, and powders. It is widely used in the detection and characterization of materials, microbiology, medicine, and other fields. The core component of the AFM device is a cantilever device, with a nanoscale probe tip at its end. When using AFM to scan the surface of a sample, the interaction between the tip and the surface atoms causes the cantilever to move up and down with the surface morphology of the sample. By optically quantifying this up and down process, the vibration of the cantilever is converted into an electrical signal, which enables the depiction of the sample surface morphology.

The working modes of AFM include contact mode and tapping mode. As the name suggests, in contact mode, the probe is always in contact with the sample surface, and it remains in contact during the scanning process, sliding across the sample surface. Thus, contact mode tends to cause wear on the probe. In tapping mode, the cantilever is always in a state of oscillation. Hence, the probe is not always in contact with the sample surface. When working, the probe's up and down movement during the scanning process causes a corresponding change in the magnitude of the cantilever's oscillation, thereby obtaining a discrete lattice of the sample surface height. When there are enough points, the surface morphology information can also be obtained. Since the probe only taps the sample in tapping mode, it significantly reduces the damage to the probe tip and the sample surface during the testing process.

In this paper, we use the Dimension Edge atomic force microscope manufactured by Bruker, shown in Figure 11. After preparing thin films using MBE, we first use AFM to characterize the surface morphology of the samples and obtain features such as surface roughness. Due to the high precision of AFM, we also use this device for characterizing the thickness of thin films, which is used to estimate the growth rate of the samples.

Figure 11. The AFM system Bruker Dimension Edge used in this work.

2.2.4 Transmission electron microscopy (TEM)

The imaging principle of transmission electron microscopy is the angular dispersion induced by electrons scattering during the electron beam transmission. The scattering angle size is related to the sample's density and thickness, so it can form images with different degrees of brightness. When electrons pass through atoms with larger density, they undergo larger scattering, resulting in darker imaging, while when they pass through smaller atoms, they undergo smaller scattering, resulting in brighter imaging. Therefore, TEM images usually present patterns with clear brightness differences. Due to the extremely short de Broglie wavelength of electrons, the resolution of TEM is much higher than that of optical microscopy, usually reaching 0.1-0.2 nm. Therefore, TEM is often used in biological fields such as virus observation and cell observation. In the field of semiconductor, because TEM can clearly show the crystal structure and element distribution results of the sample, it is often used to detect the crystal structure, electronic structure, or chemical composition of the crystalline thin films.

In this paper, the TEM equipment used is JEOL-ARM 200F transmission electron microscope from Tokyo Electron, as shown in Figure 12. The scanning working voltage is 200 kV, and the point resolution is 0.12 nm. To analyze the element distribution results of the sample, after obtaining the TEM results, we used the Carl Zeiss NVision 40 SEM/EDS workstation to analyze the energy-dispersive X-ray spectroscopy (EDS) diagram of the sample. We mainly collected spectra of elements like Fe (K), Ge (K), Te (L), O (K), and Al (K).

Figure 12. The TEM system JEOL-ARM 200F used in this work

2.3 Magnetic and transport properties characterization systems

After confirming the quality of the samples using characterization methods, we need to design and grow samples with different structures and measure the physical properties of these samples by magnetic and transport characterization systems.

2.3.1 Magneto-optic Kerr effect system (MOKE)

The basic principle of the magneto-optic Kerr effect system (MOKE) is that the direction of polarized light changes after being reflected off the surface of a magnetic material. By using a polarizer to linearly polarize incident light and filtering the reflected light through an analyzer, the magnetization of the sample surface can be extracted from the detected light intensity information. By fixing the position of the light source and the sample, and scanning the magnetic field, the hysteresis loop of the sample can be obtained. The MOKE systems are divided into polar, longitudinal, and transverse types, each obtaining the hysteresis loop in the vertical and in-plane direction respectively. As shown in Figure 13, both polar and longitudinal MOKE require the light source incident plane to be parallel to the direction of magnetization of the sample, while the transverse MOKE requires the light source incident plane to be perpendicular to the direction of sample magnetization. The three types of MOKE are applicable to different scenarios and needs.

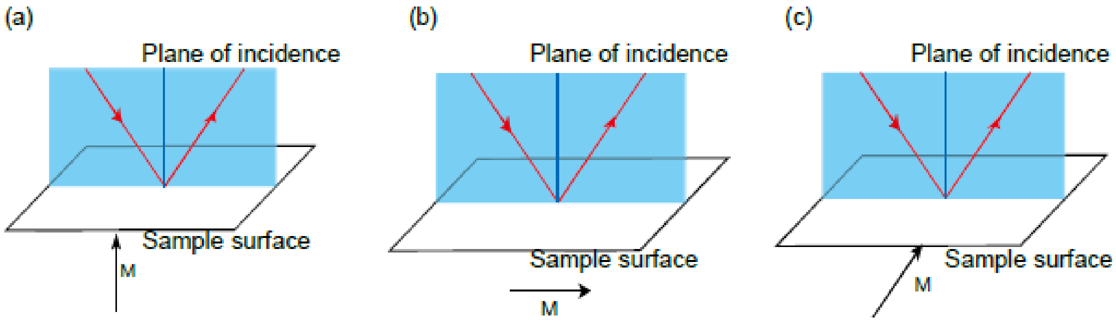

Figure 13. Three types of MOKE

The MOKE system used in this study is self-built and consists of a helium-neon laser, a photoelastic modulator (PEM), an electromagnet, an analyzer, and a photodetector, as shown in Figure 15. When using it, the sample is first placed between the two poles of the electromagnet. By changing the position of the sample and the incident light, longitudinal (in-plane) or polar (out-of-plane) MOKE signals can be measured respectively. The scanning range of the magnetic field is from -2 kOe to 2 kOe, with a step size of 100 Oe.

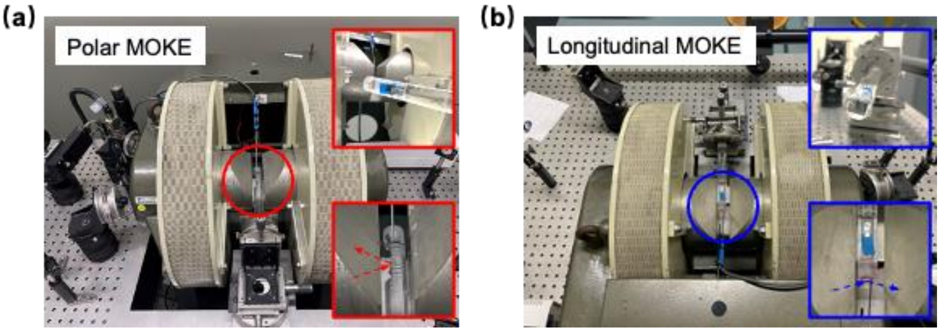

Figure 14. The MOKE system used in this work.

2.3.2 Vibrating sample magnetometer (VSM)

The vibrating sample magnetometer primarily utilizes Faraday's law of electromagnetic induction to measure the magnetism. If a magnet is placed in a constant magnetic field, its magnetization direction will be aligned spontaneous along with the external field. At the same time, the internal magnetic dipole moment of the sample will generate a magnetic field that varies as the sample moves up and down in a regular oscillation. Furthermore, this alternating magnetic field induces an electric field in the pickup coil of the VSM, and the current strength in the coil is proportional to the magnetization of the sample. Therefore, the magnetic properties of the tested sample can be calculated by measuring the induced current. VSM offers advantages such as high temperature support, ease of operation, and high measurement accuracy, with a resolution of up to 10^{-5} emu. Additionally, VSM equipment allows for measurments at different angles, enabling the simultaneous measurement of magnetization components in both longitudinal and transverse directions.

In this paper, we primarily used the Microsense VSM (Figure 15a) to characterize the high-temperature (above 300 K) magnetic properties of our samples. By selecting an appropriate sample cup, it is possible to measure the in-plane or out-of-plane magnetization curves of the sample. Generally, the magnetic field range for the VSM in this paper is -2 T to 2 T, with a scan step of 500 Oe.

2.3.3 Superconducting quantum interference device (SQUID) and physical property measurement system (PPMS)

The Superconducting Quantum Interference Device is a highly sensitive magnetic characterization device that operates based on the Josephson effect and the flux quantization phenomenon in superconductors. The SQUID system consists of a magnetic moment detection system, a cryogenic chamber, and a superconducting magnet, with a resolution of up to 10^{-7} emu. In this paper, we mainly used the MPMS3 SQUID system from Quantum Design (Figure 15b) to characterize the low-temperature (2-300 K) magnetization behavior of 2D magnetic samples. The MPMS3 system can achieve a maximum magnetic field of 7 T and operates in a temperature range of 1.8 K to 400 K. In the measurement of magnetization loops, all field scans are performed in a zero-field-cooling and field-cooling mode. For M-T measurements, the temperature scan rate is 3 K per minute.

Similar to the SQUID system, the Physical Property Measurement System (PPMS) is a low-temperature electromagnetic characterization equipment which is also developed by Quantum Design. It consists of a cryogenic chamber and a superconducting magnet. With various accessories, the PPMS can measure magnetic properties, electrical transport properties, thermal properties, and other physical properties. In this paper, we mainly used the Quantum Design PPMS-7T system (Figure 15c) to measure the magnetic and electrical transport properties of 2D magnets, including anomalous Hall curves, current-voltage curves, and ferromagnetic resonance curves.

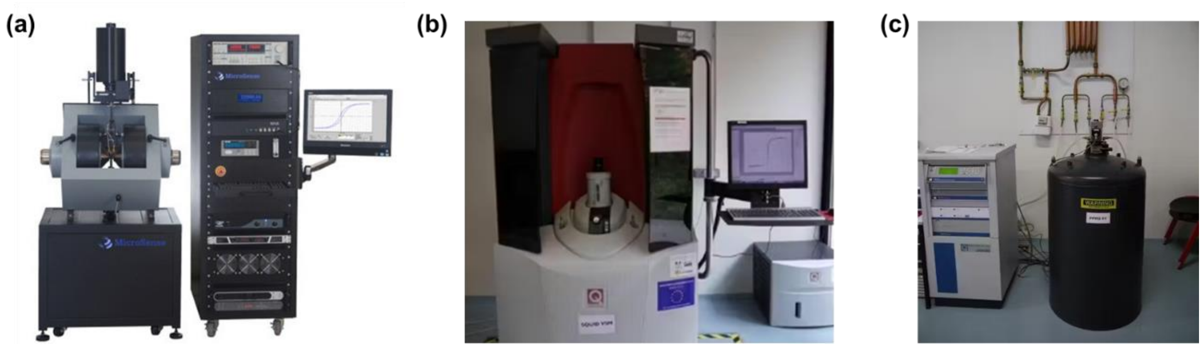

Figure 15. The VSM, SQUID and MMPS system used in this work

2.4 Chapter summary

In this chapter, we have introduced the molecular beam epitaxy (MBE) technique, which is the major method for the fabrication of 2D magnets, topological insulators, and their heterostructures. We have also briefly discussed several characterization equipment for morphology and crystal structure of the samples. Furthermore, after obtaining high-quality thin films, we will utilize various magnetic, electrical, and optical characterization equipment to measure the physical properties of the films. In the following four chapters, we will provide detailed explanations of these experimental results.

Chapter 3. Controlling Magnetism in 2D FGT by Magnetic Doping

3.1 Introduction to 2D FGT

2D materials are considered important materials supporting the development of integrated circuit manufacturing technology in the post-Moore's era. Due to their unique layered structure, 2D materials exhibit superior electrical[101], optical[102], and magnetic properties[103,104] in limited vertical dimensions. Particularly, 2D magnets have attracted widespread attention in long-distance spin transport and efficient spin operation due to their intrinsic spin characteristics, which combine the advantages of spintronics in terms of low power consumption and non-volatility, thereby stimulating numerous innovations in the spin field, such as low-dimensional spin filters[3], spin transistors[4], and magnetoresistive devices[105]. However, recent research on 2D magnets (such as CrI_3[49], $Cr_2Ge_2Te_6$[96], $Cr_2Si_2Te_6$[106], VSe_2[107], etc.) indicates that the Curie temperature (T_c) is far below room temperature. More fatally, these 2D magnets are all prepared by mechanical exfoliation, which is not conducive to subsequent device design and processing. Therefore, it is urgent to carry out large-scale, wafer-level preparation of 2D magnetic thin films that can operate at room temperature to further realize 2D spintronic devices that meet industrial needs.

The emergence of ternary 2D magnet Fe-Ge-Te (FGT) may break this dilemma. As the first discovered FGT material, Fe_3GeTe_2 has a higher T_c (220 K) than previously discovered 2D magnet[43-46]. The good conductivity makes this material be a perfect candidate to study the electron-spin interactions within 2D scale. However, as the thickness of Fe_3GeTe_2 decreases, the long-range ferromagnetic order is hard to exist due to the limitation of dimension effects[40], leading to a lower T_c (<20 K) when its thickness is below 10 nm, which severely hinders the development of 2D spintronic devices based on FGT. Although previous research has proved that the T_c of Fe_3GeTe_2 can be controlled by external modulation methods, such as ion gating[46], laser excitation[9], or proximity effects[24], these enhancement effects are not ideal and cannot meet the room temperature working needs of spintronic devices. More importantly, the experimental conditions of external control methods are complex, which may cause damage to the Van der Waals crystal structure or introduce impurities, and it is difficult to be compatible with modern integrated circuit manufacturing technology. Recent work has proved that introducing additional ferromagnetic doping into the FGT structure can obtain a new ternary 2D magnetic phase Fe_4GeTe_2[57,108-110]. Since more Fe is introduced into the system, its internal spin interaction is enhanced, leading to an enhancement of the magnetism. Figure 16 shows several 2D magnetic phase of FGT, and the numbers below represent how many Fe atoms are included in the basic unit of each phase. Experiments have proved that even at a thickness of several nanometers, the T_c of Fe_4GeTe_2 can be as high as 270 K. In addition, due to the competition between magnetic crystal anisotropy and shape anisotropy in Fe_4GeTe_2, its effective magnetic anisotropy shows temperature dependence and can be tuned to any direction. These superior magnetic properties make Fe_4GeTe_2 a universal candidate material for high-density magnetic memory and efficient spin generators.

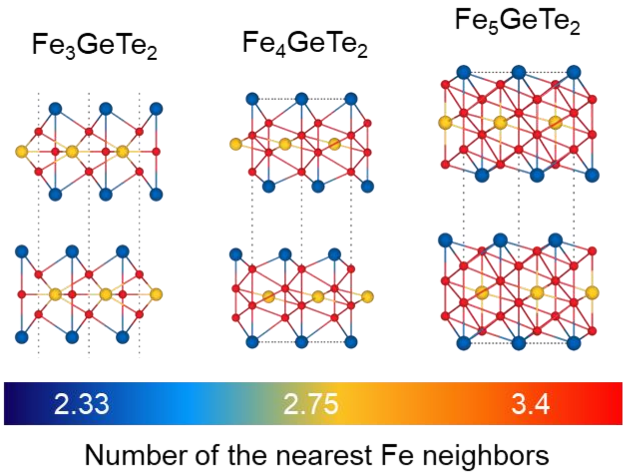

Figure 16. Various 2D ferromagnetic phases of FGT

In previous work, we successfully realized the high-quality preparation of wafer-level Fe_3GeTe_2 thin films[24]. Therefore, in this paper, we mainly focus on the preparation and magnetism manipulation of Fe_4GeTe_2. Firstly, we successfully prepared wafer-level Fe_4GeTe_2 thin films with controllable thickness using MBE, and through precise control of the growth conditions, we achieved control of the ferromagnetic order of Fe_4GeTe_2, including raising the

T_c and tunning the magnetic anisotropy. The magnetic characterization results confirmed that the T_c of our Fe_4GeTe_2 can reach above room temperature, and we also theoretically proved that magnetic doping is the fundamental mechanism of this modulation. While maintaining a high T_c, our Fe_4GeTe_2 thin film also exhibits stable and controllable magnetic anisotropy. As the Fe concentration increases, its magnetic anisotropy shifts from out-of-plane to in-plane, without any impurity phase introduction. In summary, this chapter confirms that by precisely controlling the growth process, high-quality, wafer-level 2D magnet FGT with high T_c and adjustable magnetic anisotropy can be achieved, which will give unprecedented momentum to the realization and application of 2D materials and related spintronic devices.

3.2 Sample growth of Fe_4GeTe_2

3.2.1 Epitaxial preparation process

To obtain high-quality Fe_4GeTe_2 thin films with controllable thickness, we first need to explore the large-area preparation process for Fe_4GeTe_2. In this paper, the preparation of Fe_4GeTe_2 thin films is mainly carried out in the Smart-100 molecular beam epitaxy system (as shown in Figure 8). In the epitaxy process, the most important parameter is the crystal structure of the substrate. Although Fe_4GeTe_2 belongs to the van der Waals structure and can overcome large lattice mismatches during layer-by-layer growth, experimental results show that van der Waals materials still inherit the crystal structure of the substrate during epitaxy. Therefore, choosing a suitable epitaxy substrate is the first step to realize high-quality films. Considering that Fe_4GeTe_2 belongs to the hexagonal crystal structure, we chose c-axis sapphire (Al_2O_3-0001) as the epitaxial substrate for Fe_4GeTe_2. The specific growth process is as follows:

(1) Cut a 2-inch sapphire substrate into 1 cm×1 cm square small pieces, then use acetone, IPA (isopropyl alcohol), and DI (deionized water) to ultrasonically treat the substrate for 10 minutes to remove surface impurities and pollutants. Use nitrogen to dry the substrate, then fix the substrate on a molybdenum sample holder.

(2) Put the processed substrate into the load lock chamber, close the chamber gas valve and the chamber door, turn on the rotary pump and the molecular pump, make the vacuum

degree of the sample introduction chamber reach below 10^{-7} Torr, and transfer the substrate into the growth chamber.

(3) Turn on the RHHED switch and set the working voltage and current to 1.5 A and 15 kV. Focus the RHEED electron beam on the substrate and adjust the sample angle. After observing clear and bright stripes, record the RHEED pattern of the substrate at this time.

(4) Turn on the filament current and raise the substrate temperature to 600℃ for in-situ annealing for 60 minutes. The main purpose of this step is to remove the pollutants adsorbed on the surface of alumina, and then record the RHEED pattern of the substrate at this time.

(5) Lower the substrate temperature to 280℃, and then heat the Fe, Ge, and Te sources respectively. After all temperatures are stable, open the effusion cells' shutters in turn and use the quartz to measure the flux rate of the three elements. Then, adjust the temperature to get the desired beam flow ratio (Fe:Ge:Te=4:1:10). Note that the substrate shutter is not open at this time, so it will not affect subsequent growth.

(6) Open the shutter blocking the substrate in the growth chamber, start epitaxial growth, and use RHEED to monitor the growth status in real time and in-situ, and use the c quartz to monitor the growth rate in-situ.

(7) Record key parameters such as growth time, RHEED pattern, vacuum level, source temperature, etc. during the growth process. After the growth is completed, close the substrate shutter and the three source shutters in turn, and restore the temperature to room temperature. If necessary, after the growth is completed, the sample can be annealed at 280℃ for five minutes to obtain better crystal quality.

(8) After all temperatures have dropped to room temperature and the growth chamber environment is stable, transfer the sample into the load lock chamber and take out the sample, and the growth is over.

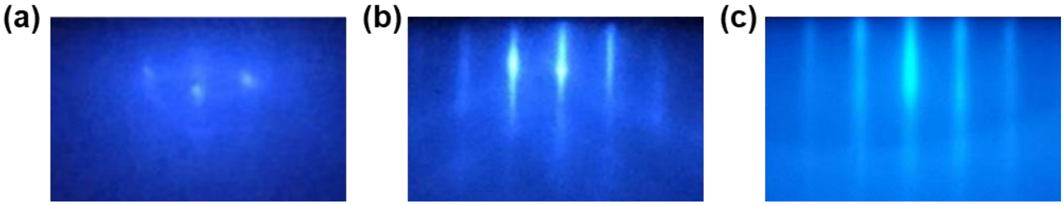

Figure 17. Several typical RHEED patterns (a) Alumina substrate before annealing; (b) Alumina substrate after annealing; (c) 10 nm Fe_4GeTe_2 thin film.

3.2.2 The epitaxy mechanism of Fe_4GeTe_2

To explore the crystal quality of Fe_4GeTe_2 on the substrate (α-Al_2O_3), the lattice match scheme of Fe_4GeTe_2 must be figured out. Considering the relatively high lattice mismatch (~20%), a special epitaxial mode $Fe_4GeTe_2{:}Al_2O_3=2{:}\sqrt{3}$ was proposed as shown in Figure 18a. By rotating 30°, the lattice mismatch of the $Fe_4GeTe_2|Al_2O_3$ heterostructure is suppressed to 2%. After rotating 30°, the Fe_4GeTe_2 crystal demonstrates the same in-plane orientation as the Al_2O_3 crystal, as shown in the black arrow. For crystals with a hexagonal structure, the RHEED result may demonstrate a pattern along either [11-20] or [1-100] direction, according to the incident direction of the electron beam. The key feature to distinguish these patterns is the distance between the streaky lines (*D*), which was determined by the interplanar spacing (or *d*-spacing, *d*) of the crystal structure along the direction, and they always follow a relation as $D{\sim}1/d$. Because the [11-20] direction has a larger *d*-spacing, more streaky lines can be observed in the RHEED pattern, while the [1-100] direction has fewer streaky lines. Therefore, the Fe_4GeTe_2 in Figure 18a is expected to present an RHEED feature of the same direction as the Al_2O_3 substrate, due to the same structural arrangement of the crystals. By contrast, if no rotation during the growth, the Fe_4GeTe_2 will keep a strict 1:1 epitaxial mode along with the structure of Al_2O_3. Under this growth mode, the RHEED of Fe_4GeTe_2 will demonstrate a different feature from that of Al_2O_3 because the angle between the crystal directions of the Fe_4GeTe_2 and the substrate is 30°, as shown in Figure 18b. The epitaxial mode in Figure 18a can be proved by the experimental results in Figure 18c. After deposition, the RHEED of Fe_4GeTe_2 demonstrates the same line density as that of Al_2O_3 despite the different original RHEED directions, indicating the alignment of Al_2O_3 substrate and Fe_4GeTe_2 film, and proving the presence of crystal rotation of Fe_4GeTe_2 during the deposition.

The rotation epitaxial mode secures a relatively small mismatch as well as the strain during the Fe_4GeTe_2 growth. The in-plane thickness-dependent lattice constants (a) of Fe_4GeTe_2 can be roughly extracted from the time-resolution RHEED pattern by $a_{\mathrm{Fe_4GeTe_2}}:a_{\mathrm{Al_2O_3}}=D_{\mathrm{Al_2O_3}}:D_{\mathrm{Fe_4GeTe_2}}$, which is shown in the inset of Figure 18d. The initial Fe_4GeTe_2 suffers a trivial lattice extension and it shrinks quickly as the thickness increases, indicating the small lattice mismatch and strain during the growth.

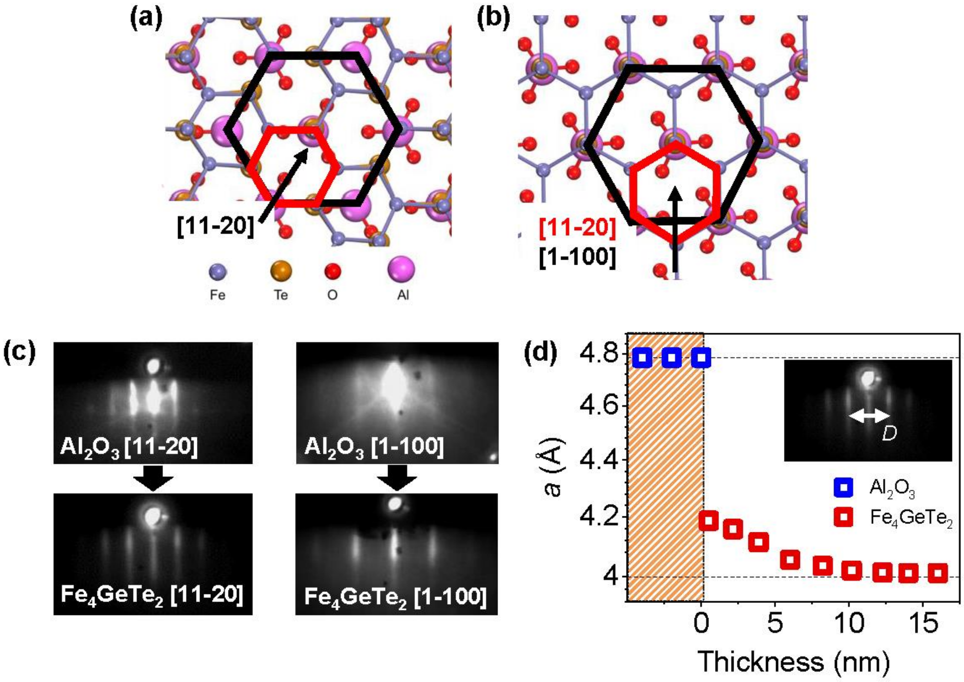

Figure 18. The epitaxy mode of Fe_4GeTe_2 (a, b) Two different epitaxy patterns of Fe_4GeTe_2; (c) RHEED patterns of sapphire substrates with different initial crystal orientations and after the growth of Fe_4GeTe_2; (d) The trend of the change in the in-plane lattice constant of Fe_4GeTe_2 with thickness.

3.3 Characterization of Fe_4GeTe_2

Fe_4GeTe_2 has a rhombohedral crystal structure which belongs to the R-3m space group, as shown in Figure 19. Similar to Fe_3GeTe_2, Fe_4GeTe_2 also has Fe-Fe dumbbell structural units, which alternate off the horizontal line and form a honeycomb lattice with a Ge atom in the center of the honeycomb. As a van der Waals material, the basic structure of Fe_4GeTe_2 is also made up of overlapping layers of Fe-Ge-Te atoms (ML), each layer contains a layer of Fe4Ge atoms bonded by covalent bonds and two Te interlayers. Specifically, the thickness of each ML is approximately 9.7 Å, and adjacent MLs are separated by van der Waals gaps.

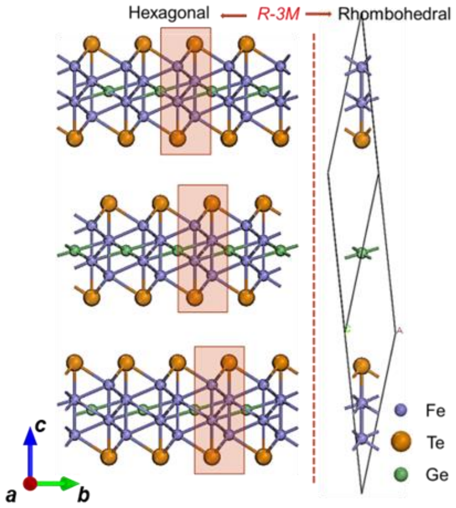

Figure 19. Crystal structure of Fe_4GeTe_2. Left: The crystal of Fe_4GeTe_2 with ABC stacking; Right: A schematic diagram of the rhombohedral unit of Fe_4GeTe_2 crystal.

3.3.1 Crystal structure characterization of Fe_4GeTe_2

As Fe_4GeTe_2 is a ternary compound, it is necessary to precisely control the composition of the three elements during the growth process, otherwise different FGT phases (Fe_3GeTe_2, Fe_4GeTe_2) will occur, or even non-ferromagnetic phase (FeTe). After the growth, it is necessary to characterize the crystal structure of the samples using XRD to explore the contribution of the growth condition to the formation of 2D magnetic phases. As shown in Figure 20, our sample shows clear XRD peaks, and further studies have confirmed that all the peaks come from the {003} crystal plane of Fe_4GeTe_2[110], proving that our Fe_4GeTe_2 have a good crystalline quality.

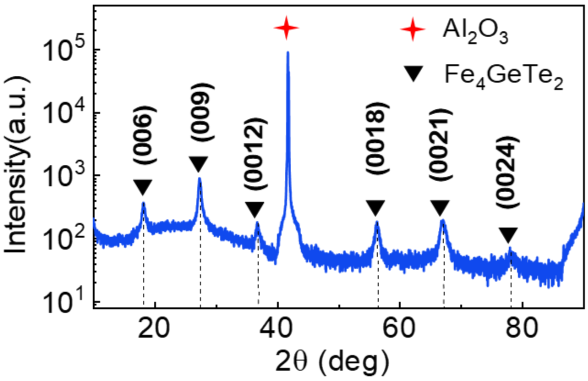

Figure 20. The XRD result of Fe_4GeTe_2

In order to separate the Fe_3GeTe_2 and Fe_4GeTe_2 phases, we prepared thin films of Fe_3GeTe_2 and Fe_4GeTe_2 of the same thickness by precisely controlling the growth conditions, and compared their crystal structures using XRD methods. As shown in Figure 21a, in Fe_3GeTe_2 (space group P6$_3$/mmc), Fe-Fe dumbbells form a triangular lattice that interpenetrates to the Fe-Ge honeycomb lattice. While in Fe_4GeTe_2 (space group R-3m), Fe-Fe dumbbells form a corrugated honeycomb lattice hosting one Ge atom at the center. Therefore, Fe_4GeTe_2 is expected to present a different peak positions from Fe_3GeTe_2 in XRD results. As shown in Figure 21b, the Fe_3GeTe_2 shows the peaks belong to the {002} family, while only the {003} family peaks were obtained in Fe_4GeTe_2, indicating that no disorder and impurity phase is induced during the iron-enrichment epitaxy in this work.

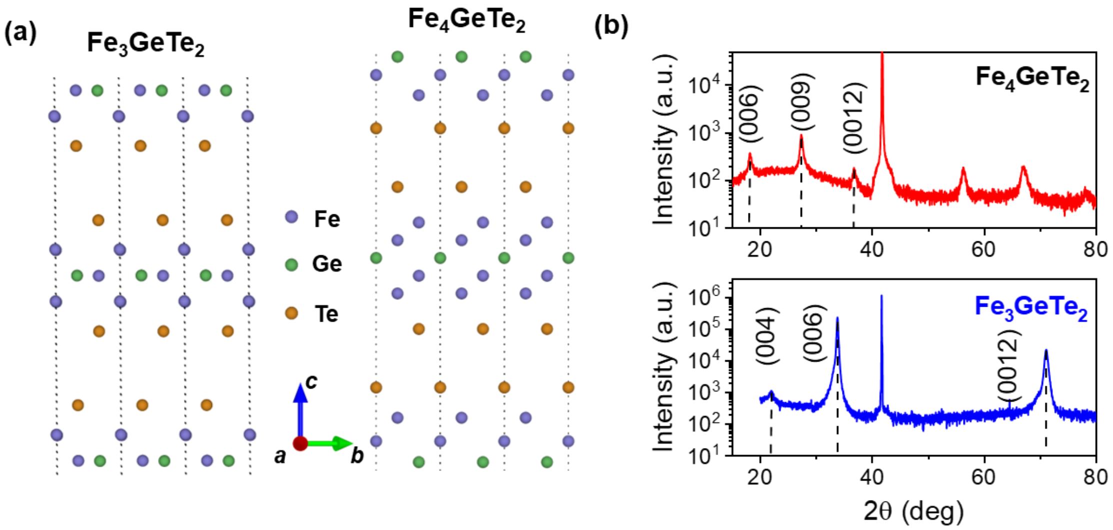

Figure 21. Schematic diagrams of the crystal structures of Fe_3GeTe_2 and Fe_4GeTe_2 and the corresponding XRD results

After determining the crystal structure of the prepared Fe_4GeTe_2 sample, we used a transmission electron microscope (TEM) to study the crystalline quality and layer-by-layer growth pattern of the sample. Figure 22 shows the result of our high-angle annular dark-field scanning transmission electron microscopy (HAADF-STEM) measurement results of our Fe_4GeTe_2. It is obvious that our Fe_4GeTe_2 thin film shows a clear 2D layered structure with van der Waals gaps between layers, which is consistent with the definition of a 2D van der Waals material. At the same time, we used the EDS system to analyze the chemical composition of the obtained Fe_4GeTe_2, confirming that its Fe content is 57%, which is consistent with the expected ratio of Fe:Ge:Te=4:1:2. Further EDX spectra proved that elements Fe, Ge, and Te are evenly distributed on the thin film, demonstrating that our Fe_4GeTe_2 has high quality and uniformity.

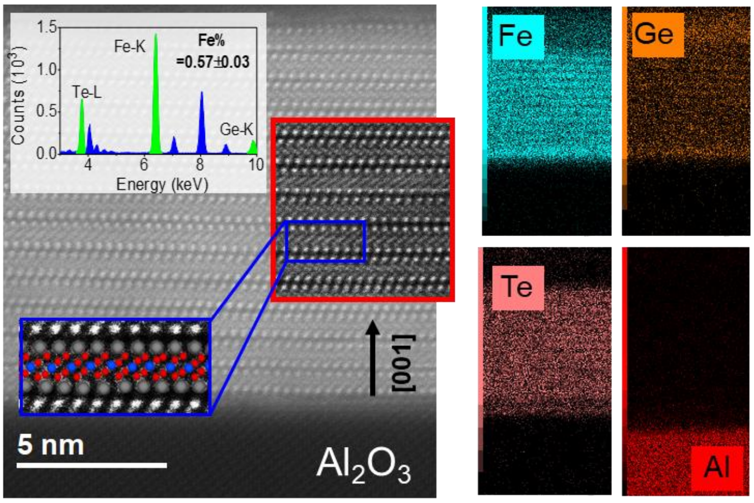

Figure 22. TEM and EDX results of Fe_4GeTe_2

3.3.2 Magnetic characterization of Fe_4GeTe_2

After obtaining high-quality Fe_4GeTe_2 thin films, the core goal of this thesis is to achieve a high T_c Fe_4GeTe_2 film to achieve 2D spin devices operating above room temperature. Therefore, it is necessary to characterize the magnetic properties of the obtained Fe_4GeTe_2 thin films.

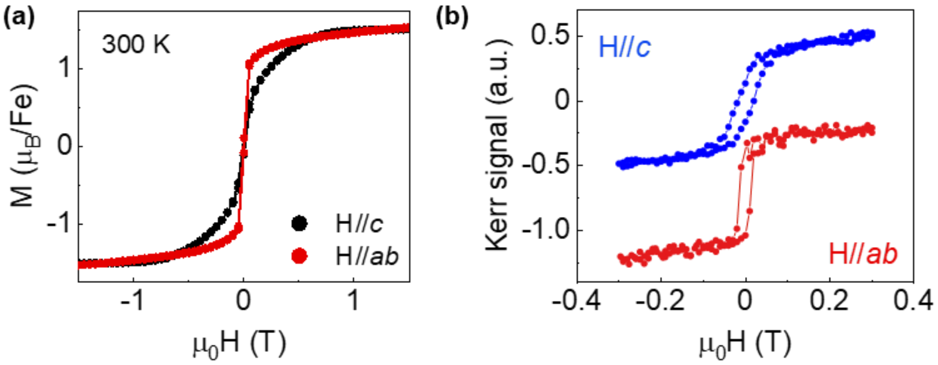

Figure 23. The M-H curves for 4 nm Fe_4GeTe_2 at room temperature (a) VSM result; (b) MOKE result

Firstly, we prepared a 10 nm Fe_4GeTe_2 thin film using MBE equipment, and used a VSM device to measure its room temperature magnetic hysteresis curve (M-H curve), as shown in Figure 23. At room temperature, Fe_4GeTe_2 exhibits stable in-plane magnetic anisotropy, and its effective magnetic anisotropy (K_{eff}) can be calculated by the following formula: $K_{eff}=1/2M_s\times H_{sat}$, where M_s and H_s represent the saturation magnetization strength and saturated field of the hard axis, respectively. Since the hard axis of Fe_4GeTe_2 is vertical, the effective magnetic anisotropy of Fe_4GeTe_2 at 300 K can be calculated as -0.12 J/cm^2. The results of MOKE are similar to those of VSM. At room temperature, the in-plane magnetization flipping energy is less than that in the out-of-plane direction for Fe_4GeTe_2, proving that the film has in-plane magnetic anisotropy. In order to study the magnetic properties of Fe_4GeTe_2 at low temperatures, we used a SQUID to measure the M-T curve of the sample, as shown in Figure 24. The result of VSM shows that the coercive field of Fe_4GeTe_2 is small, so we first used a 1T in-plane magnetic field to saturate the sample's magnetization. Subsequently, while keeping the magnetic field constant at 1T, we reduced the sample temperature from 300 K to 2 K, and used SQUID to continuously measure the magnetization of the sample. Figure 24 shows that at 2 K, the saturated magnetization of the sample is 2.13 μ_B/Fe, which is greater than the previously reported value for Fe_3GeTe_2[44].

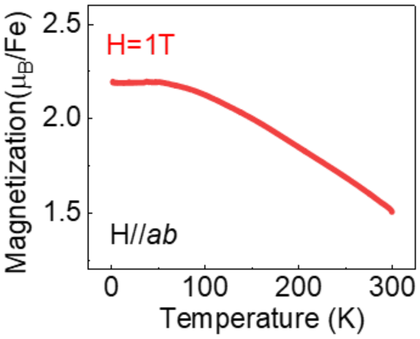

Figure 24. The in-plane M-T curve for 4 nm Fe_4GeTe_2 at H=1T.

Previous studies have shown that Fe_4GeTe_2 exhibits a temperature-dependent magnetic anisotropy, which shows an in-plane anisotropy at higher temperatures and out-of-plane magnetic anisotropy at low temperatures. Our experimental results also confirm this conclusion. When using SQUID to measure the hysteresis loop of our Fe_4GeTe_2, it was found that the sample shows a different easy-axis at low (2 K) and high (300 K) temperatures. Figure 25a clearly shows the temperature-dependent magnetic anisotropy of Fe_4GeTe_2, which may originate from the energy competition within Fe_4GeTe_2. The effective magnetic anisotropy energy of a magnetic thin film mainly includes two parts: magnetocrystalline anisotropy energy (K_m) and shape anisotropy energy (K_{sh}, also known as demagnetizing field energy), where K_m always follows the direction of the easy axis (out-of-plane direction), and K_{sh} always points to the in-plane direction. K_{eff}, K_m and K_{sh} satisfy the following relationship:

$$K_{eff} = K_m + K_{sh} = K_m - (\mu_0 / 2) M_S^2 \tag{3.1}$$

Because the magnetization of Fe_4GeTe_2 changes greatly with temperature, its effective magnetic anisotropy also shows strong temperature dependence. We calculated the effective magnetic anisotropy K_{eff} of Fe_4GeTe_2 at different temperatures, as shown in Figure 25b. Here, the positive sign of K_{eff} indicates that the sample is in an out-of-plane magnetic anisotropy, and the negative sign indicates that the sample is in an in-plane magnetic anisotropy state. At lower temperatures, due to the contribution of K_m is far greater than that of K_{sh} (at 5 K, K_{sh}=-0.4 J/cm^2 and K_m =0.88 J/cm^2), the value of K_{eff} is positive, and the sample shows out-of-plane magnetic anisotropy. While at 300 K, the contribution of K_{sh} is greater than K_m (at 300 K, K_{sh} =-0.23

J/cm^2 and K_m =0.08 J/cm^2), the value of K_{eff} is negative, and the sample shows in-plane magnetic anisotropy.

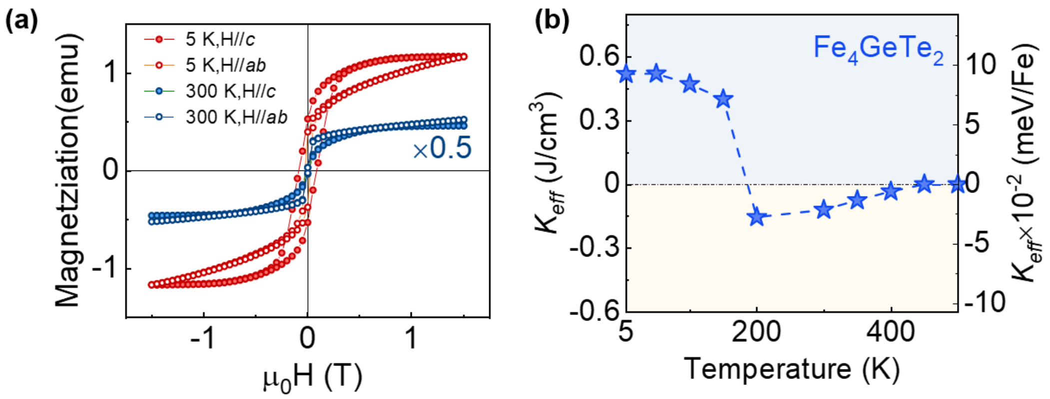

Figure 25. Magnetic anisotropy of Fe_4GeTe_2 with temperature (a) Hysteresis loop of Fe_4GeTe_2 at 5 K and 300 K; (b) Effective magnetic anisotropies K_{eff} as a function of temperature

Furthermore, the magnetic properties of the sample can be characterized by transport measurements. Generally speaking, the Hall resistance R_{xy} of magnetic materials can be divided into two parts: normal Hall component and anomalous Hall component:

$$R_{xy}=R_N\cdot H+R_A\cdot M \tag{3.2}$$

Where the first and second terms represent the normal and anomalous Hall components respectively, R_N represents the normal Hall coefficient, and R_A represents the anomalous Hall coefficient. Obviously, when the external magnetic field is small, the anomalous Hall component dominates the Hall resistance of the sample, and is positively correlated with its magnetization. Since Fe_4GeTe_2 exhibits metallic characteristics, the normal Hall resistance of the film is very small and can be ignored compared to the anomalous Hall resistance. Therefore, the magnetization of the sample can be characterized by studying the change of R_{xy}. In addition, from Eq (3.2), it is known that when the temperature of the magnetic sample reaches the T_c, the magnetization becomes zero. At this time, the Hall resistance only contains the normal Hall effect, and its resistance hysteresis loop appears as a straight line. Therefore, the T_c of the material can be identified by the temperature-dependent Hall curves. When the Hall resistance of the sample passes through the origin, it means that there is no spontaneous magnetization in the system at this time, and the corresponding temperature is the magnetic transition temperature, that is T_c.

In this paper, we prepared a 10 nm Fe_4GeTe_2 into a Hall bar structure and used a physical property measurement system (PPMS) to characterize its transport properties. As shown in Figure 26a, the resistance of the sample increases with the rise of temperature, which is consistent with the transport characteristics of metallic films. Figure 26b shows the Hall resistance (R-H curve) of the sample at different temperatures. At 20-300 K, the R-H curve shows clear hysteresis characteristics, proving that our Fe_4GeTe_2 sample has a T_c higher than room temperature, which is consistent with the magnetic measurement results (Figure 26). Obviously, when the temperature is between 20-200 K, the sample's coercive field is larger (over 3000 Oe), which means that the sample has a large M_r. Conversely, as the temperature continues to rise, the sample's coercive field quickly drops to 100 Oe, while the M_r also rapidly decreases. This temperature-dependent transition comes from the change in the magnetic anisotropy of Fe_4GeTe_2. Below 200 K, the magnetic anisotropy of Fe_4GeTe_2 points in the out-of-plane direction, resulting in a larger remanent magnetization when the filed along *c* direction. When the temperature reaches above 200 K, Fe_4GeTe_2 shifts from out-of-plane anisotropy to in-plane anisotropy, resulting in a smaller remanent magnetization when the filed along *ab* direction.

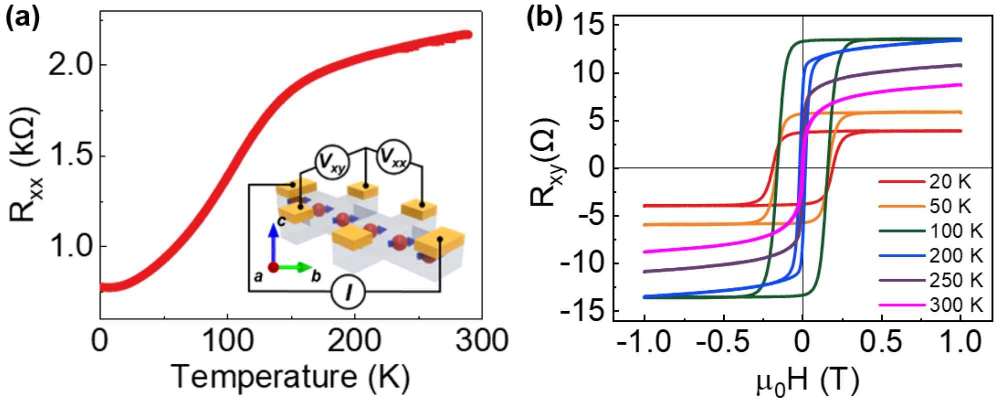

Figure 26. The transport properties of Fe_4GeTe_2: (a) Temperature dependence of the longitudinal resistance. Inset: the schematic image of the Hall bar device. (b) Anomalous Hall resistance R_{xy} as a function of temperature

3.4 Doping-modulated magnetism in Fe_4GeTe_2

According to the Mermin-Wagner theorem, due to the influence of thermal fluctuations, a 2D system cannot maintain its long-range ferromagnetic order at finite temperatures[40]. However, the magnetic anisotropy of 2D magnetic materials can break this limitation, and a gap can be opened in the spin spectrum to suppress the impact of thermal fluctuations. Specifically, the larger magnetic anisotropy of FGT grants this material the highest T_c among the 2D magnet family[46]. More importantly, with the increase of Fe components, the excess Fe atoms will form a quasi-3D arrangement inside the crystal structure, which significantly enhances the magnetic exchange interaction, and can also increase the T_c of the sample, which is why Fe_4GeTe_2 has a higher T_c than Fe_3GeTe_2. Our experimental results demonstrate that by increasing the concentration of Fe elements during growth, it is possible to achieve 2D magnetism in FGT near room temperature.

In the previous section, we discussed the temperature-dependent magnetic anisotropy of Fe_4GeTe_2. In fact, achieving stable, adjustable magnetic anisotropy in 2D magnets is of great significance for realizing universal spintronic devices. For instance, for magnetic random-access memory (MRAM), magnetic films with perpendicular magnetic anisotropy exhibit lower switching currents and smaller device sizes compared to these with in-plane magnetic anisotropy. In magnetic sensors, materials with in-plane anisotropy are often used to enhance the sensitivity[111]. Therefore, exploring how to achieve stable and controllable magnetic anisotropy is one of the key research contents of Fe_4GeTe_2. In this section, we will discuss how to realize stable magnetic anisotropy in Fe_4GeTe_2 by magnetic doping.

3.4.1 Generation of 2D magnetism and the Heisenberg model

In section 1.3, we discussed how to use the Heisenberg model to describe two-dimensional magnetism:

$$H = \sum\nolimits_{ij} J_{ij} S_i \cdot S_j + \sum_i A(s_i^z)^2 \tag{3.3}$$

Eq (3.3) explains the relationship between ferromagnetism and spin-exchange interactions. Here, we also use Eq (3.3) to describe the origin of magnetism in Fe_4GeTe_2 and employ methods like density functional theory (DFT) calculations to explain the intrinsic mechanisms of magnetism generation and manipulation in the material. Although the Stoner model has been widely used to explain itinerant ferromagnetism in magnetic materials [77], considering the sufficient local magnetic moments of Fe atoms, previous research on Fe_3GeTe_2 has proven that the 2D magnetism of FGT can be explained by a Heisenberg model with RKKY exchange interactions [46].

In the earliest Heisenberg model, only the magnetic order induced by direct exchange interactions of *d*-orbit electrons was considered. When the distance between magnetic sites in the lattice increases, the magnitude of the direct exchange interaction weakens, and theoretically, the magnetism of the material will also decrease correspondingly. However, some materials can also present a strong magnetism even the direct exchange interactions do not dominate the magnetism because of indirect RKKY interactions. In 1954, Ruderman and Kittel proposed that *s*-orbital electrons could serve as mediators of magnetic coupling interactions [112]; in 1956, Kasuya and Yosida expanded this model to explain the magnetic source in rare earth elements, positing that indirect exchange interactions between *4f* electrons are the reason for the ferromagnetism in rare earth and some alloy materials [113,114]. This indirect exchange interaction, established between two localized magnetic moments through the conductive electrons in the material, is known as the Ruderman-Kittel-Kasuya-Yosida interaction (RKKY). RKKY is an important and common effect in spintronics. For non-magnetic materials (like semiconductors, insulators, etc.), when magnetic elements are doped within them, magnetic atoms can perform RKKY exchanges through conductive electrons within the material, thus achieving magnetic order. According to the original RKKY theory, the RKKY exchange interaction produced by conductive electrons between localized magnetic moments $\boldsymbol{S_1}$, $\boldsymbol{S_2}$ located at different lattice is $H_{RKKY}=J_{12}(\boldsymbol{S_1}\cdot\boldsymbol{S_2})$, where J represents the interaction between $\boldsymbol{S_1}$ and $\boldsymbol{S_2}$. Generally, the size of J decreases as the distance r between $\boldsymbol{S_1}$ and $\boldsymbol{S_2}$ increases, its relationship is approximately $J{\sim}r^{-3}$.

Figure 27a shows the atomic structure of a single layer of Fe_4GeTe_2, where there are two different Fe sites, named α-Fe and β-Fe respectively. Since α-Fe is more localized than β-Fe, it has a larger spin. Our calculation shows that the spin of α-Fe is 3/2, while the spin of β-Fe is 1/2. Therefore, it can be calculated that the average magnetic moment per Fe atom near 0 K is 2.5 μ_B, which is close to the results we obtained in the experiment (Figure 24). In Figure 27a, there are three pairs of nearest exchange interactions, which we name as J_1, J_2, and $J_{2\beta}$. Their spatial distances are approximately 2.5 Å. The naming comes from the relative position of the Fe atoms in the lattice, as shown in the insert of Figure 27b. In the hexagonal grid composed of Fe atoms, countless circles can be drawn with a certain Fe atom as the center. Therefore, J_i represents the exchange interaction of the α-Fe (or β-Fe) at the center of the circle with the β-Fe (or α-Fe) in the i_{th} circle; $J_{i\beta}$ represents the exchange interaction of the β-Fe at the center of the circle with the β-Fe in the i_{th} circle. Therefore, the internal exchange interaction of Fe4GeTe2 can be represented as [115]:

$$J(r) = -J^2 \times \frac{sin(2k_F r) - 2k_F r cos(2k_F r)}{(k_F r)^4} \tag{3.4}$$

where r is the distance between the two spin sites and k_F is the Fermi momentum of the itinerant electrons. Kondo model treats localized electrons as magnetic impurities embedded in the itinerant conducting electrons and J describes the exchange interaction of a localized spin coupled to delocalized electrons. The RKKY model further describes the interaction between two localized spins via the conduction electrons. Figure 27b shows $J(r)$ relations from the nearest exchanges to far above 8 Å.

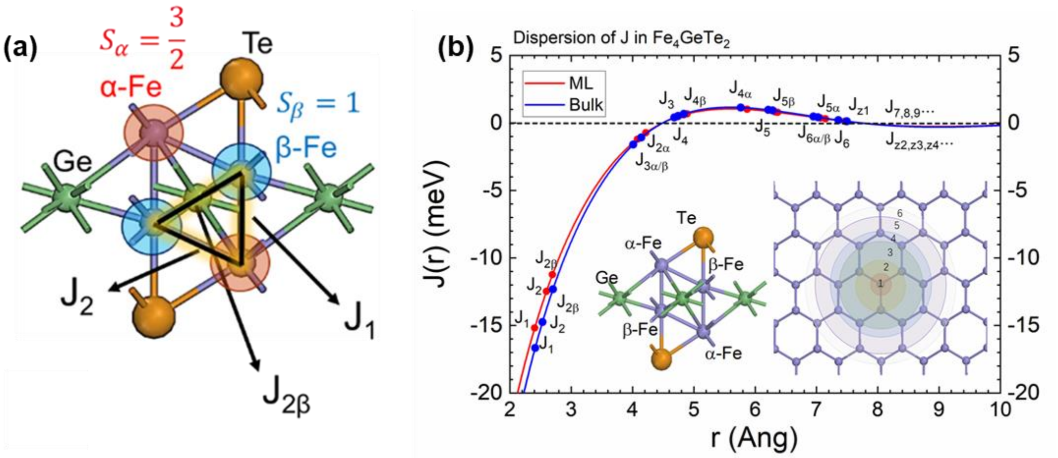

Figure 27. First-principle calculation of the magnetic properties of Fe_4GeTe_2

3.4.2 Doping-modulated magnetism in Fe_4GeTe_2

According to Eq (3.3), the magnetism of Fe_4GeTe_2 is related to the interaction between magnetic atoms. Therefore, when the Fe concentration in Fe_4GeTe_2 is increased, the number of spin interactions increases, directly enhancing the magnetism of Fe_4GeTe_2. At the same time, the increase in the number of Fe atoms will inevitably lead to a decrease in the distance r between magnetic atoms in the lattice, further enhancing the magnetism of the material. Our experimental results confirm this theoretical prediction. Three thin films with the same thickness (10 nm) but different Fe concentrations were prepared (named $Fe_{4\text{-}x}GeTe_2$, Fe_4GeTe_2, and $Fe_{4+x}GeTe_2$). Then we used SQUID to measure their hysteresis loops at different temperatures, as shown in Figure 28. With the increase of temperature, $Fe_{4+x}GeTe_2$ still maintains good hysteresis characteristics, followed by Fe_4GeTe_2. The temperature stability of $Fe_{4\text{-}x}GeTe_2$ is the worst, which is nearly linear at 300 K, proving that the temperature is approaching the T_c of the sample.

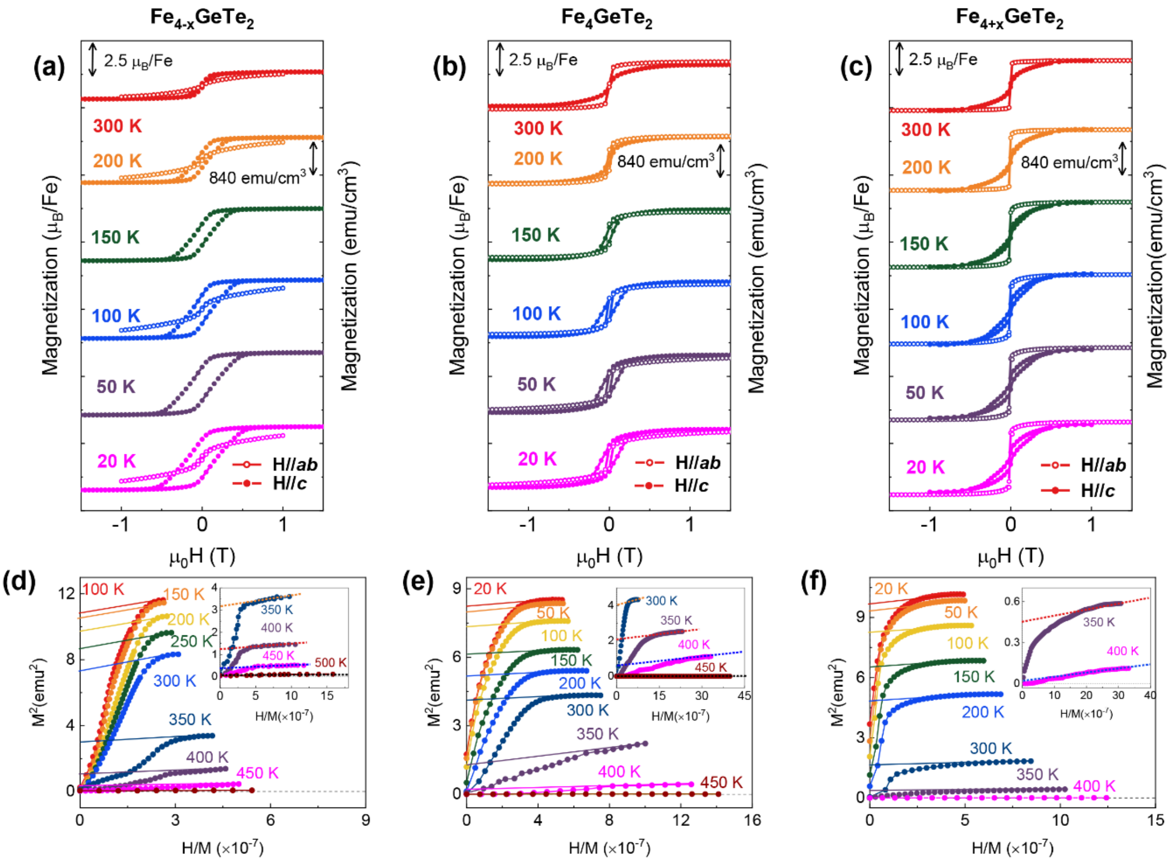

Figure 28. Stoichiometry-dependent T_c of Fe_4GeTe_2 films with different Fe concentrations

To calculate the specific T_c of the three samples, we used the Arrott plot to fit the hysteresis loops of the three samples. According to the theory proposed by Arrott, the relationship at the phase transition temperature of a ferromagnetic material is:

$$M^2 = \frac{1}{4b}\frac{H}{M} - \frac{a}{2b}e \qquad (3.5)$$

Plotting the square of magnetization (M^2) on the y-axis and the ratio of the external magnetic field to the magnetization (H/M) on the x-axis for different temperatures, we can get an Arrott plot. From Eq (3.5), it is obvious that when $T=T_c$, the curve passes through the origin. Therefore, in the Arrott curves obtained at different temperatures, the temperature corresponding to the curve passing through the origin is the T_c of the sample. Figure 28d-f summarize the Arrott curves of the three samples $Fe_{4-x}GeTe_2$, Fe_4GeTe_2 and $Fe_{4+x}GeTe_2$. Obviously, as the Fe concentration increases, the magnetism of Fe_4GeTe_2 becomes stronger and its T_c keeps rising.

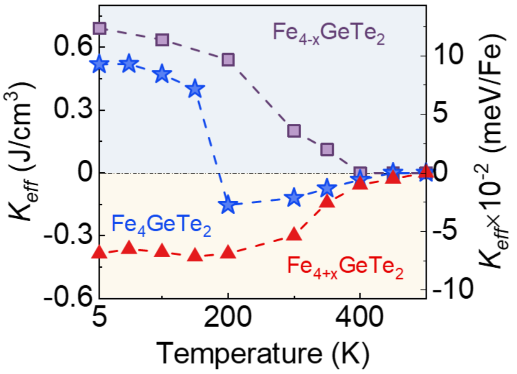

Figure 29. Effective magnetic anisotropies K_{eff} as a function of temperature for the samples

Different from $Fe_{4-x}GeTe_2$ or $Fe_{4+x}GeTe_2$, which always present a specific direction of magnetic anisotropy at all temperatures, Fe_4GeTe_2 shows a temperature-dependent transition from perpendicular magnetic anisotropy to in-plane anisotropy, which is consistent with previous results (Figure 25). Similar to Fe_3GeTe_2 reported previously [116,117], our $Fe_{4-x}GeTe_2$ also shows strong perpendicular magnetic anisotropy, with a magnetocrystalline anisotropy K_m greater than 1 J/cm^2 at 20 K. However, the magnetocrystalline anisotropy in Fe_4GeTe_2 is only 0.88 J/cm^2, and in $Fe_{4+x}GeTe_2$, it is only 0.23 J/cm^2. However, the shape anisotropy K_{sh} of $Fe_{4+x}GeTe_2$ is greater than -0.6 J/cm^2. The smaller magnetocrystalline anisotropy combined with the larger shape anisotropy ensures that $Fe_{4+x}GeTe_2$ can maintain a stable in-plane magnetic anisotropy at all temperature ranges. Thus, we propose that as the Fe concentration increases, the magnetocrystalline anisotropy K_m inclines towards the in-plane direction, leading to an increase in K_{sh}, and ultimately causing the magnetic anisotropy to shift from the out-of-plane to the in-plane direction. Figure 29 summarizes the effective magnetic anisotropy of the three samples $Fe_{4-x}GeTe_2$, Fe_4GeTe_2, and $Fe_{4+x}GeTe_2$ as a function of temperature, confirming that magnetic doping can effectively tune the magnetic anisotropy of Fe_4GeTe_2.

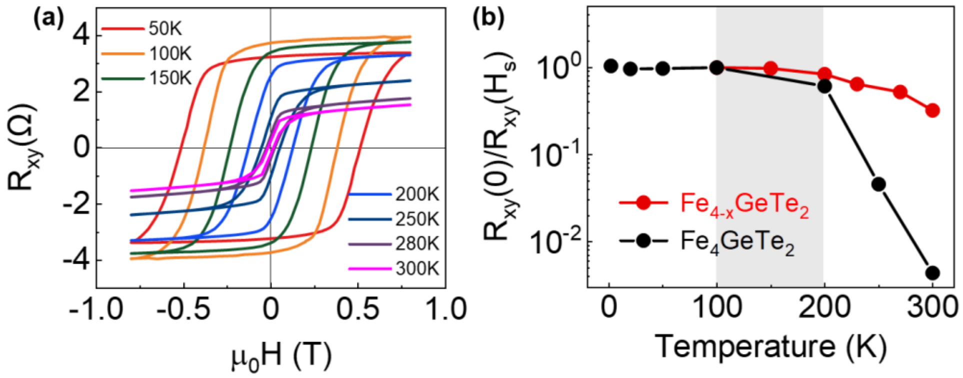

Figure 30. The magnetic properties of $Fe_{4-x}GeTe_2$ and Fe_4GeTe_2: (a) Hall resistance of $Fe_{4-x}GeTe_2$; (b) $R_{xy}(0)/R_{xy}(H_s)$ curves as a function of temperatures for the two samples

In section 3.3, we demonstrated that transport results can be used to verify the magnetic anisotropy transition in Fe_4GeTe_2, which has been observed in Figure 25. Figure 30a shows the Hall resistance of $Fe_{4-x}GeTe_2$ at different temperatures. Unlike Fe_4GeTe_2, $Fe_{4-x}GeTe_2$ always maintains a relatively large coercive field, and a series of clear hysteresis loops can be observed even at high temperatures. Figure 30b compares the normalized remnant anomalous Hall resistance $R_{xy}(0)/R_{xy}(H_s)$ versus the temperatures for $Fe_{4-x}GeTe_2$ and Fe_4GeTe_2, where the $R_{xy}(0)$ and the $R_{xy}(H_s)$ are defined as the anomalous Hall resistance at zero and out-of-plane saturated magnetic field, and the values were extracted from the Hall curves in Figure 30a and Figure 26b. At all temperature ranges, the $Fe_{4-x}GeTe_2$ always demonstrates a robust value of ~1, indicating the relatively high remanent magnetization due to the strong PMA. For Fe_4GeTe_2, despite the value of $R_{xy}(0)/R_{xy}(H_s)$ close to 1 at low temperatures, it decreases substantially from 100 K and finally vanishes when the temperature reaches 250 K. The decrease in the remanent magnetization results from the spin reorientation in the Fe_4GeTe_2, which gives rise to the IMA while suppressing the PMA term in the magnetism.

3.4.3 Doping-modulated crystal structure of Fe_4GeTe_2

Figure 21 compares the crystal structures of Fe_4GeTe_2 and Fe_3GeTe_2. Since it contains more Fe atoms, Fe_4GeTe_2 (a=4.08 Å) has a larger cell volume than Fe_3GeTe_2 (a=3.995 Å). Therefore, as the Fe concentration increases, $Fe_{4+x}GeTe_2$ is expected to have a larger lattice constant than Fe_4GeTe_2, while $Fe_{4-x}GeTe_2$ will have a smaller value than Fe_4GeTe_2 due to fewer Fe atoms. Here, we use vertical XRD to test the three samples $Fe_{4-x}GeTe_2$, Fe_4GeTe_2, and $Fe_{4+x}GeTe_2$, to determine the manipulation of doping on the crystal structure of FGT.

In section 2.5, we discussed the basic principle of XRD. When X-rays are incident on the surface of a crystal with a plane spacing of d at a certain angle θ, if the incident condition satisfies Bragg's equation $n\lambda=2d\sin\theta$, its intensity will add up in the reflection direction. Here, d represents the interplanar spacing of the crystal, θ is the angle of incidence of the X-ray, λ represents the wavelength of the X-ray, and n is the diffraction level corresponding to the crystal plane. Therefore, after obtaining the XRD spectrum of the sample, the interplanar spacing of the crystal can be inferred through Bragg's formula, that is, the lattice constant along the c-axis direction.

As shown in Figure 31a, although the Fe concentrations are different, all the three samples $Fe_{4-x}GeTe_2$, Fe_4GeTe_2 and $Fe_{4+x}GeTe_2$ only show peaks of {003} family, proving that the magnetic doping will not introduce other impurify phases into Fe_4GeTe_2. Upon careful observation, we found that as the concentration of Fe in the sample increased, there was a slight shift to the right in the XRD peak position, as shown in the inset of Figure 32a. According to Bragg's Law, a shift to the right in the peak position represents an extension of the crystal lattice in the c direction, which is consistent with our prediction. Further, by incorporating the XRD data of the three samples into the Bragg's Law formula, we calculated the c-axis lattice constants of the three samples as approximately 29 Å for $Fe_{4-x}GeTe_2$, 29.1 Å for Fe_4GeTe_2, and 29.2 Å for $Fe_{4+x}GeTe_2$. Figure 31b summarizes the variation in T_c and c-axis lattice constant of 10 nm Fe_4GeTe_2 with different Fe concentrations. As the proportion of Fe in the sample increases, more magnetic atoms entered the unit cell, enlarging the lattice constant of the sample; simultaneously, the increased number of magnetic atoms also strengthened the spin-spin interaction *J* within the magnetic material, leading to an enhancement of the T_c.

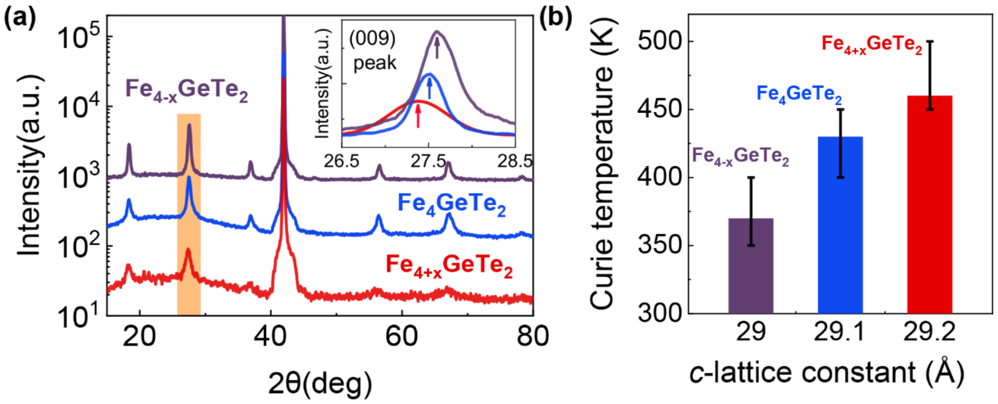

Figure 31. Doping-modulated magnetism in Fe_4GeTe_2 (a) XRD scan of the samples with different Fe doping concentrations. (b) The *c*-lattice constants and T_c of all the samples

Table 2. The parameters of Fe_4GeTe_2 with different Fe concentration

Fe concentration	2θ (009) [deg]	*c* [Å]	T_C [K]	Easy axis
4-x	27.420	29	400	*c*
4	27.362	29.1	400-450	*c*
4+x	27.323	29.2	460	*ab*

3.5 Chapter summary

In this chapter, we have achieved the large-area preparation of the 2D magnet Fe_4GeTe_2 using MBE, and the film has shown good surface morphology and crystalline quality as proven by various characterization methods. Consistent with previous research results, our Fe_4GeTe_2 also exhibits temperature-dependent magnetic anisotropy. Through a careful analysis of the results, we confirmed that this shift in magnetic anisotropy originates from the competition between the magnetocrystalline anisotropy and shape anisotropy within the film. Further, we have established a Heisenberg model that includes RKKY exchange interactions to describe the 2D ferromagnetism of Fe_4GeTe_2. Based on this model, we have proposed a method for controlling its magnetic properties through magnetic doping, and discovered three 2D magnetic phases of Fe_4GeTe_2: Fe_4GeTe_2, $Fe_{4+x}GeTe_2$, and $Fe_{4-x}GeTe_2$. Through electrical and magnetic characterization on these three samples, we have unveiled that the T_c and magnetic anisotropy of Fe_4GeTe_2 has a positive correlation with the Fe doping concentration.

Chapter 4. Interfacial Engineering of the Magnetism in Fe_4GeTe_2

For 2D magnets, the T_c is undoubtedly one of the most important parameters. Achieving high T_c magnetism is the foundation for developing low-dimensional spintronic devices for industry. Generally speaking, to meet the working requirements of the industry, the temperature tolerance of the spintronic device must reach at least 125℃ (400 K) [115]. However, almost no intrinsic 2D magnets can meet this standard. Therefore, finding new ways to greatly increase the T_c of 2D magnetic thin films is becoming a hot direction in this field.

In the previous chapter, we introduced the preparation of Fe_4GeTe_2 thin films and analyzed the effects of magnetic doping on the T_c and crystal structure of the sample. It's worth noting that during the testing of the magnetic properties of Fe_4GeTe_2, it was found that the T_c of Fe_4GeTe_2 we prepared is above 400 K under any doping concentration (as shown in Table 2), which far exceeds the past reports about mechanically exfoliated Fe_4GeTe_2. Considering the difference between epitaxially prepared 2D thin films and mechanically exfoliated samples, we speculate that this high-temperature magnetism comes from the interfacial effect between Fe_4GeTe_2 and the sapphire substrate. In this chapter, we plan to determine the interfacial enhancement effect on Fe_4GeTe_2 magnetism by preparing a series of thickness-dependent samples.

4.1 Thickness-dependent T_c of Fe_4GeTe_2 thin films

In Table 2, we summarized the T_c of 10 nm Fe_4GeTe_2 with different Fe concentrations. Obviously, the T_c of our Fe_4GeTe_2 is higher than that of mechanically exfoliated samples (T_c~270 K)[109]. Compared to the mechanical stripping method that prepares thin film samples through external force transfer, epitaxially prepared samples have better Fe_4GeTe_2/Al_2O_3 interface quality, which contributes to the formation of various novel interface effects. This might be the fundamental reason for the increase in the T_c of Fe_4GeTe_2 in this paper. Since the interfacial effect only exists at the thin film interface, its contribution decreases with the increase of the sample thickness. Therefore, we plan to determine the contribution of the interface to the T_c by studying the magnetic properties of thickness-dependent Fe_4GeTe_2. Further, by screening the samples with the highest T_c, we will quantify this enhancement effect by various magnetic characterization methods.

Firstly, we prepared Fe_4GeTe_2 thin films of 4 nm and 16 nm thickness under the same conditions (Fe:Ge=1:4), and used SQUID (Figure 32a) and VSM system (Figure 32b) to test the temperature-dependent remnant magnetization of the thin film (M_r-T). According to the mean field theory, the M_r with $M_r(T) \propto (T_c\text{-}T)^{\beta}$. When the temperature is higher than T_c, the material transitions from ferromagnetism to paramagnetism, and M_r becomes 0. Therefore, by observing the point where $M_r=0$ in the M_r -T curve, the Curie temperature of the thin film can be known. In this experiment, to accurately measure the remnant magnetization, we first cooled the sample to low temperature in a 1T in-plane field to fully saturate the magnetization, then reduced the external field to 0, and tested the magnetization with temperature. The M_r -T curve of the 16 nm Fe_4GeTe_2 thin film is similar to the previous reports, with its T_c around 300 K. However, the T_c of the 4 nm Fe_4GeTe_2 thin film is far beyond the 16 nm sample, which reachws over 500 K. Generally speaking, the T_c of a 2D magnetic film will decrease with the reduction of sample thickness, this is due to the suppression of the system's long-range ferromagnetic order by thermal fluctuations when the dimension is reduced[40]. Therefore, it can be speculated that the abnormal increase in the T_c shown in Figure 32 is due to the enhancement of Fe_4GeTe_2's magnetism by the Fe_4GeTe_2/Al_2O_3 interface. When the sample thickness is small, the interfacial effect can cover the entire sample thickness, leading to a significant increase in the T_c; when the sample thickness is large, the contribution of the interfacial effect is relatively small, and the magnetic properties of the sample tend to its intrinsic properties, therefore the T_c of the 16 nm Fe_4GeTe_2 is almost consistent with that of the mechanically exfoliated sample.

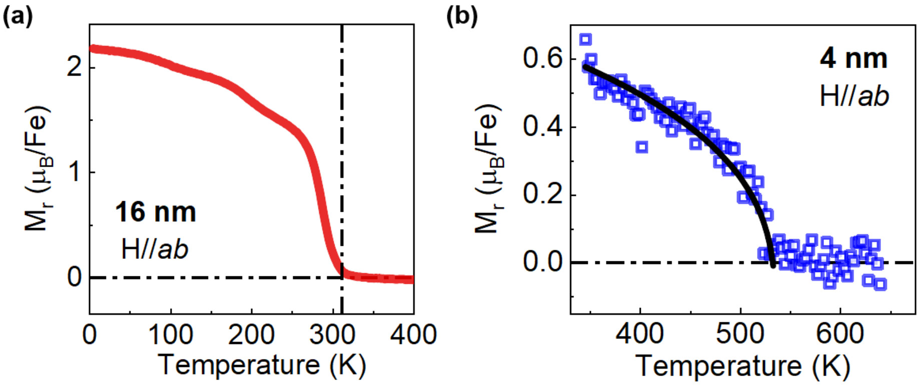

Figure 32. M_r-T curves of Fe_4GeTe_2 with two different thicknesses

To verify the authenticity of the high T_c of the 4 nm sample, we used multiple methods to characterize its magnetic properties. Figure 33a shows the in-plane M-H curve of 4 nm Fe_4GeTe_2 as a function of temperature obtained by VSM, demonstrating clear hysteresis characteristics up to 500 K. This confirms the existence of a high T_c in its internal long-range magnetic moment. Additionally, the square shape of the M-H curve proves that the sample can maintain good in-plane anisotropy even at high temperatures. Further temperature-dependent MOKE results also verify this conclusion. As shown in Figure 33b, under an in-plane magnetic field, when the temperature rises from 300 K to 400 K, the 4 nm Fe_4GeTe_2 sample can maintain a clear and distinct M-H curve. Conversely, under a vertical magnetic field, the sample struggles to maintain the shape of its hysteresis loop while heating (Figure 33c). These results confirm that 4 nm Fe_4GeTe_2 possesses stable in-plane magnetic anisotropy above room temperature, consistent with the results in Figure 33a.

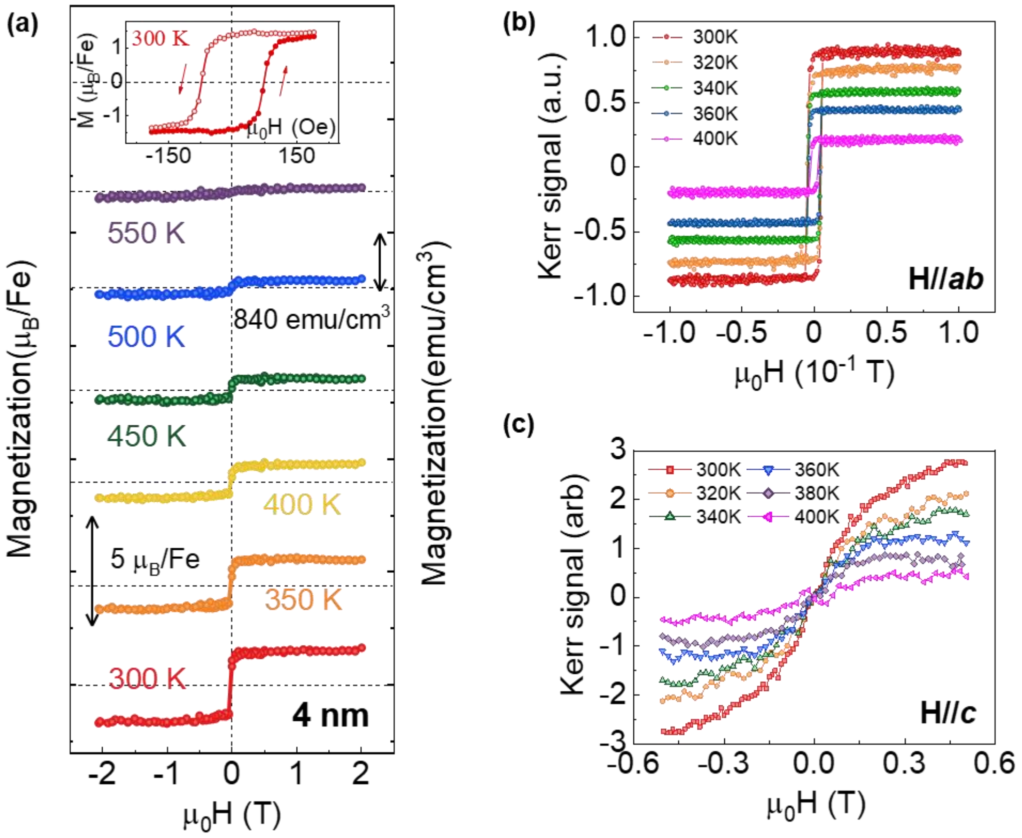

Figure 33. Hysteresis loop of 4 nm Fe_4GeTe_2 at high temperatures

To confirm that the enhancement of the T_c originates from the interface, we prepared a series of Fe_4GeTe_2 thin films with different thicknesses (4 nm, 8 nm, 10 nm, 12 nm, 16 nm), and measured their M_r-T curves using VSM, as shown in Figure 34a. Clearly, the T_c of our Fe_4GeTe_2 negatively correlates with the sample thickness. The 4 nm sample shows the highest T_c, maintaining its ferromagnetism up to ~530 K, while the 16 nm sample exhibits the lowest value, around only 270 K. The thickness dependence of the T_c again identifies the contribution of the interface on magnetism manipulation. Figure 34b compares the T_c and effective magnetic anisotropy of Fe_4GeTe_2 prepared in this study with those reported in the literature for 2D magnets. Compared to mechanically exfoliated samples, our epitaxially grown Fe_4GeTe_2 exhibits the highest T_c, while also maintaining a strong magnetic anisotropy, demonstrating great potential for use in high-temperature spintronic devices.

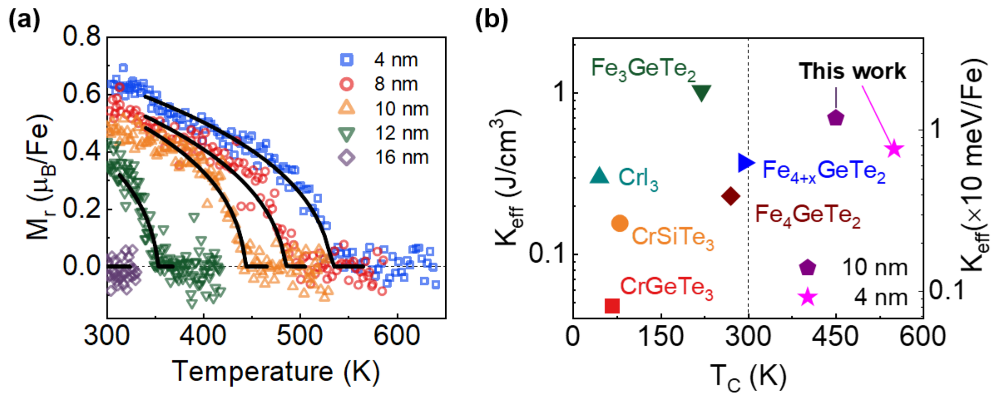

Figure 34. Interface-enhanced high-temperature magnetism in Fe_4GeTe_2

4.2 Interfacial exchange in Fe_4GeTe_2

4.2.1 Electronic structure of Fe_4GeTe_2

In the previous section, we learned that the fundamental mechanism of interface effects is to change the electronic structure of magnetic materials, thereby controlling their ferromagnetism. Therefore, before starting to study the Fe_4GeTe_2/Al_2O_3 interface, we first calculated the electronic structure of pure Fe_4GeTe_2 using DFT methods. Figure 35a shows the spin-related band structure on the surface of a single layer of Fe_4GeTe_2 (lattice constants a=b=4.08 Å), where the blue lines represent the majority spin bands, mainly occupied by Fe *d*-orbital electrons; the red lines represent the minority spin bands, which are mostly unoccupied. Figure 35b shows the partial density of states (PDOS) of a single layer of Fe_4GeTe_2. Obviously, near the valence band, the material's density of states (DOS) mainly comes from the contribution of Fe atom's *d*-orbital electrons, and its localized states (E_d) determine the magnetism of the material, where the localized state electrons here are the unpaired Fe *d*-orbital electrons.

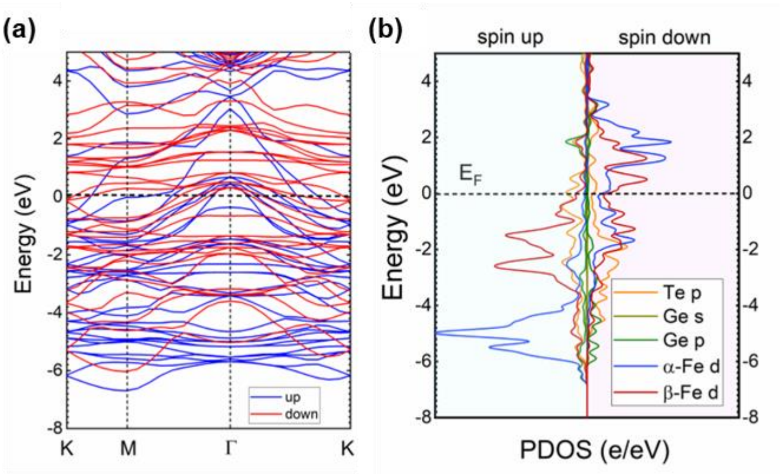

Figure 35. Band structure of Fe_4GeTe_2 monolayer

4.2.2 Interfacial exchange model in Fe_4GeTe_2/Al_2O_3

In section 3.4, we proposed a Heisenberg model including RKKY interaction to describe the magnetism of Fe_4GeTe_2:

$$H = \sum_{ij} J_{ij} S_i \cdot S_j + \sum_i A(s_i^z)^2 \tag{4.1}$$

According to the RKKY model, the exchange interaction J between localized magnetic moments $\boldsymbol{S_1}$, $\boldsymbol{S_2}$ located at two different lattice points in Fe_4GeTe_2 can be expressed as

$$J(r) = -J^2 \times \frac{sin(2k_F r) - 2k_F r cos(2k_F r)}{(k_F r)^4} \tag{4.2}$$

Based on Eq. (4.1) and (4.2), we used Metropolis Monte Carlo (MMC) simulations to simulate the temperature-dependent magnetization for a monolayer Fe_4GeTe_2, bulk Fe_4GeTe_2, and the Fe_4GeTe_2/Al_2O_3 interface. As shown in Figure 36, MMC calculations predict that the T_c of monolayer Fe_4GeTe_2 is about 200 K, while that of bulk Fe_4GeTe_2 is 270 K. This value is basically consistent with previous literature. However, after forming an interface with Al_2O_3, the T_c of monolayer Fe_4GeTe_2 would be elevated to nearly 600 K. It is worth mentioning that in MMC calculations, we simplify the flipping of the anisotropy of Fe_4GeTe_2 to maintain stable perpendicular magnetic anisotropy at low temperatures (0-100 K), in-plane anisotropy at high temperatures (above 200 K). Figure 36 verifies that the Fe_4GeTe_2/Al_2O_3 interface can indeed enhance the magnetism of Fe_4GeTe_2, which is in line with our experimental results.

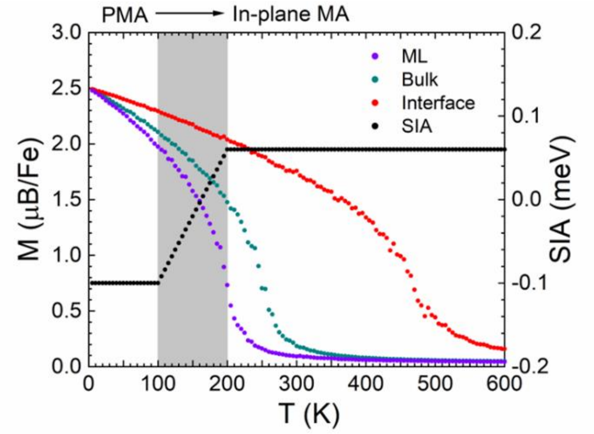

Figure 36. Average magnetization per Fe versus temperature for the ML, bulk, and interface-modulated Fe_4GeTe_2

According to Eq. (4.1), the enhancement of the exchange interactions is the main reason for the dramatic T_c increase. Notably, the change of the exchange interactions stems from J rather than the Fe-Fe distances r as it cannot be changed a lot. According to the Anderson model, J is related to the distance between the Fermi level (E_F) and the localized states that contribute to the formation of magnetic moments (E_d), as well as the Hubbard U which denotes the onsite Coulomb repulsion[116,117]:

$$J \sim -\frac{1}{E_F - E_d} + \frac{1}{E_F - E_d - U} \tag{4.3}$$

This is under the condition that $E_d < E_F < E_d + U$, where the magnetic moment arises from single occupation of the localized level rather than zero or two. The J^2 has a local minimum when the E_F is in the mid of E_d and E_d+U. In Fe_4GeTe_2, the E_d is the energy level of the unpaired d electrons in Fe.

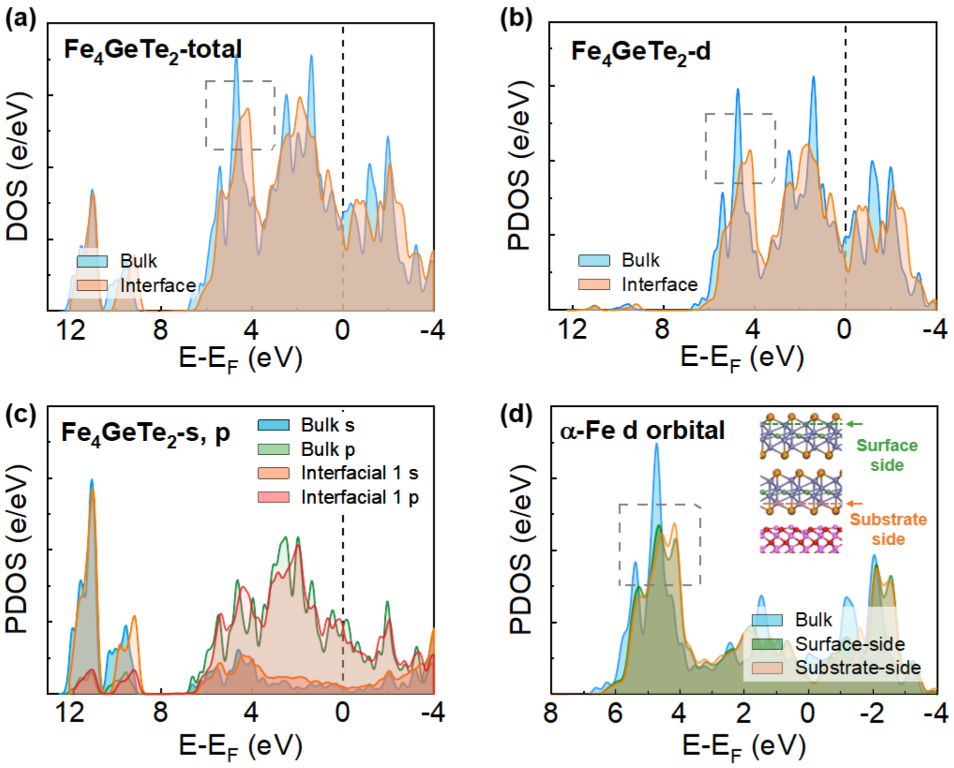

Figure 37. The calculated (a) total DOS, (b) *d* orbital electrons PDOS, (c) *s* and *p* orbital electrons PDOS, and (d) α-Fe d orbital PDOS for Fe_4GeTe_2 with and without the interface.

Considering the thickness dependency of the T_c in Figure 34, we assume that the shift of E_d induced by the interface is the reason for the T_c enhancement. Here we calculate the DOS of Fe_4GeTe_2 with and without interface. After integration with the sapphire, the valence band DOS moves towards E_F, as shown in Figure 37a. Figure 35b has indicated that the valence band of Fe_4GeTe_2 is dominated by Fe *d* bands, therefore, the DOS shift mainly comes from the redistribution of *d* orbital electrons in Fe_4GeTe_2, which indeed presents the same collapse towards E_F on a sapphire substrate (Figure 37b). On the contrary, the PDOS of *s* and *p* orbitals are barely changed with an interface (Figure 37c). Considering that α-Fe provides the largest magnetic moments, we calculate the PDOS of α-Fe *d* electrons to inspect the interface-induced localized states (E_d) shift, as shown in Figure 37d. On the interface, the orbital coupling between Fe_4GeTe_2 and sapphire induces a right shift of Fe *d* PDOS, which will move the E_d towards the E_F, leading to an enhancement of J as well as the T_c. Notably, for Fe atoms on the surface side and the substrate side, their *d* orbitals PDOS suffer different delocalization, as the interfacial effect is more prominent on the substrate side, which is the reason for the thickness dependency in Figure 34.

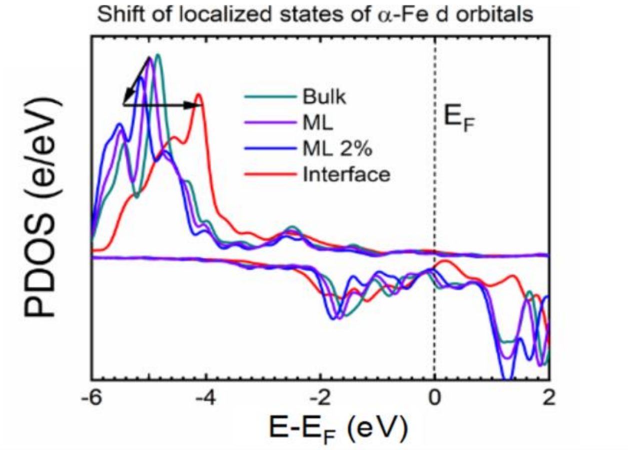

Figure 38. PDOS of the *d* orbitals of the α-Fe in bulk, ML with 2% strain and interface-modulated Fe_4GeTe_2

Here we calculate the PDOS of α-Fe *d* electrons to inspect the interface-induced E_d shift in Fe_4GeTe_2, as shown in Figure 38 (the red curve), compared with the bulk or monolayer forms, the integration with the sapphire induces a right shift of unpaired Fe *d* electrons, which will move the E_d towards the E_F, and is the key factor leading to the enhancement of J.

4.3 Experimental evidence for the interfacial magnetism manipulation

To verify the theoretical model in Section 4.2, we plan to use Ultraviolet Photoelectron Spectroscopy (UPS) and X-ray Photoelectron Spectroscopy (XPS) to measure the changes in the electronic structure of Fe_4GeTe_2 with thickness, to verify the manipulation of the interface. The principles of UPS and XPS are basically the same. Both use light containing a certain amount of energy to irradiate the sample. The electrons in the sample are excited due to the photoelectric effect. By collecting and detecting the excited electrons, key information such as the electronic structure and material composition of the sample can be obtained.

4.3.1 XPS and UPS system

Ultraviolet Photoelectron Spectroscopy (UPS) is a common method to determine the electronic structure of a sample. UPS often uses ionization radiation from helium to generate an ultraviolet light source, where the photon energy of the He I resonance line is 21.21 eV, and He II is 40.82 eV. According to the Einstein photoelectric effect, the electrons in the sample will break the bondage of the atom and become excited after absorbing the energy of the radiated light. This process can be described as $E_k=hv-E_B-\Phi sp$, where E_k is the kinetic energy of the radiated electron, hv is the kinetic energy of the incident photon, E_B is the binding energy of the ionized electron, and Φsp is the work function of the spectrometer (a fixed value, approximately 4 eV). It is worth noting that because ultraviolet light has a very small energy, the electrons excited by UPS only come from the outermost energy level, namely, the valence band electrons. Therefore, UPS is often used to detect the valence band structure of materials, including valence band hybridization, maximum valence band, work function, Fermi energy level, etc. At the same time, due to the shallow transmission depth (1~2 nm), UPS can be used as a surface-sensitive technology to detect surface contamination of the sample.

Compared with UPS, XPS often uses Mg or Al radiation sources, with photon energies greater than 1 keV. X-rays have a high penetration depth (~10 nm) and can characterize the electronic structure of samples throughout the entire thickness. At the same time, due to the larger photon energy of X-rays, it can excite the deep energy level electrons of the material (such as *s* and *p* orbital electrons). Since these electrons have weak interactions, they can reflect the fingerprint information of the atoms they belong to. Therefore, XPS can be used to analyze the elemental composition, valence state, and other information of the material. Compared with the high resolution of UPS (0.01 eV), the resolution of XPS is lower, only reaching ~0.5 eV. It is worth noting that there is no superiority or inferiority between XPS and UPS. They each have their own strengths in terms of detection depth and resolution and can be used to measure different characteristics of materials. Due to their complementarity, they can also be combined in most cases to provide a comprehensive analysis of the sample's structure and chemical characteristics.

The Soleil photoelectron spectroscopy system used in this paper integrates UPS and XPS testing systems, which consists of a vacuum chamber, an ion gun, and a detector. In the UPS test, the equipment mainly uses He-I radiation to generate ultraviolet light, and its photon energy is 21.22 eV; in the XPS test, it mainly uses Al-Kα as a radiation source to generate X-rays, and its photon energy is 1486.6 eV. In addition, the Soleil photoelectron spectroscopy system is also equipped with standard etching equipment, which can remove surface contamination from the sample before the photoelectron spectroscopy measurment. The energy of Ar^+ ion sputtering used is 800 eV.

4.3.2 Thickness-dependent photoelectron spectroscopy

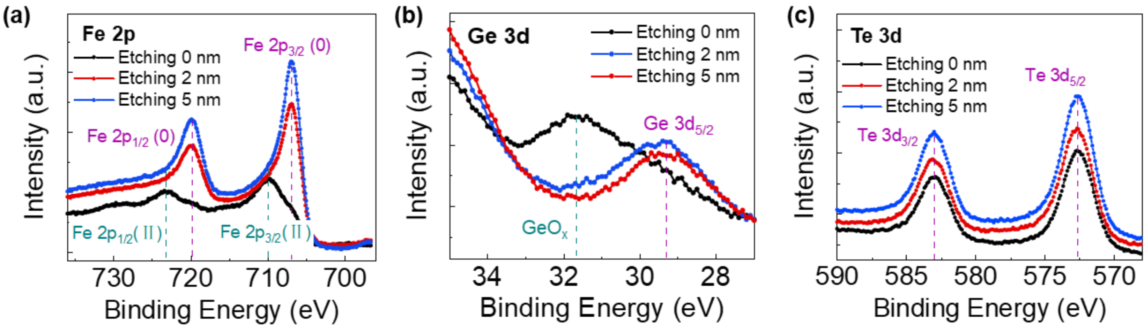

Figure 39. The XPS spectra for Fe 2p, Ge 3d, and Te 3d states after 0 nm, 2 nm, and 5 nm etching in Fe_4GeTe_2 thin film.

To verify our theoretical calculation, we use the UPS spectrum to probe the E_d shift induced by the interface. A 16 nm Fe_4GeTe_2 was deposited on a sapphire substrate firstly, followed by several times of ion etching and UPS measurements. With etching, the film thickness can be decreased in situ and the contribution of the interface will be enhanced. Notably, although etching has been used as an applicable method to control the thickness of 2D materials, it is difficult to achieve it on an atomic scale. In this work, the removed thicknesses may be not so precise, which corresponds to the average etching depth according to our previous calibration. To prove that no impurity phase was introduced into the film after etching, we performed repeated XPS measurements before each UPS measurement. The XPS was performed in the same UHV chamber as UPS and etching, thus, it is in situ and won't introduce any pollution. Figure 39 shows the XPS spectra of Fe, Ge, and Te elements after etching 0 nm, 2 nm, and 5 nm. Before etching, several oxidation peaks could be observed for Fe and Ge elements, then these peaks vanish with the etching. After etching 2 nm and 5 nm, the peaks for all the elements stay stable and the positions are the same as previous work on FGT, indicating that there is no phase change during the etching process.

Figure 40 compares the valence band DOS we obtained by theoretical calculation and the UPS experiments. After etching, a peak appears at ~4.1 eV, which corresponds to the Fe *d* localized states because of the PDOS shift. As the film thickness decreases, the peak becomes stronger due to the enhanced interfacial orbital coupling, as shown in Figure 40b-d. The UPS spectrum is consistent with our calculated PDOS for α-Fe *d* electrons (Figure 40a). A recent work[46] indicated that the T_c of the FGT can be enhanced by electron doping, which shifts the E_F and leads to a modulation in the magnetism as well as the carrier density. However, the contribution of the electron doping can be excluded because no E_F shift was observed in the zoom-in UPS spectrum (the inset of Figure 40).

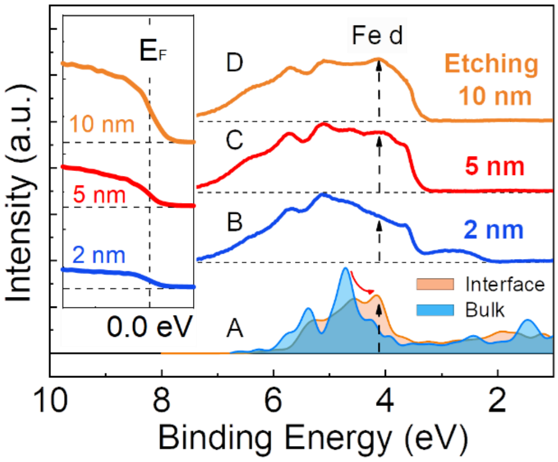

Figure 40. The electronic structure change with film thickness (a) The calculated *d* orbital PDOS for the α-Fe in bulk and interfacial Fe_4GeTe_2. (b, c, d) The UPS spectrums for the valence band DOS after etching 2 nm, 5 nm, and 10 nm. Inset: the DOS near the E_F for b, c, and d.

4.3.3 The effect of etching on FGT quality

Etching, which is referring to the process of selectively removing or thinning specific parts of the deposition layer by physical or chemical, is one of the most important steps in semiconductor manufacturing. Recent research shows that etching can also be used to modify 2D films. As an auxiliary means of 2D preparation technology, etching can be used for defect control and thickness control in 2D materials [118-121]. In the previous section, we achieved the measurement of the photoelectron spectrum of Fe_4GeTe_2 at different thicknesses. The core technology is to thin the Fe_4GeTe_2 sample by in-situ etching. However, due to the extremely sensitive surface of 2D materials, Ar$^+$ etching will inevitably cause damage to the material, such as lattice destruction, component change, valence state change, etc. Whether these damages will change the electronic structure of Fe$_4$GeTe$_2$ and thereby lead to the local state offset shown in Figure 40 is a factor we must exclude. Therefore, in this section, we will focus on the impact of Ar$^+$ etching on the crystal structure and chemical composition of Fe$_4$GeTe$_2$.

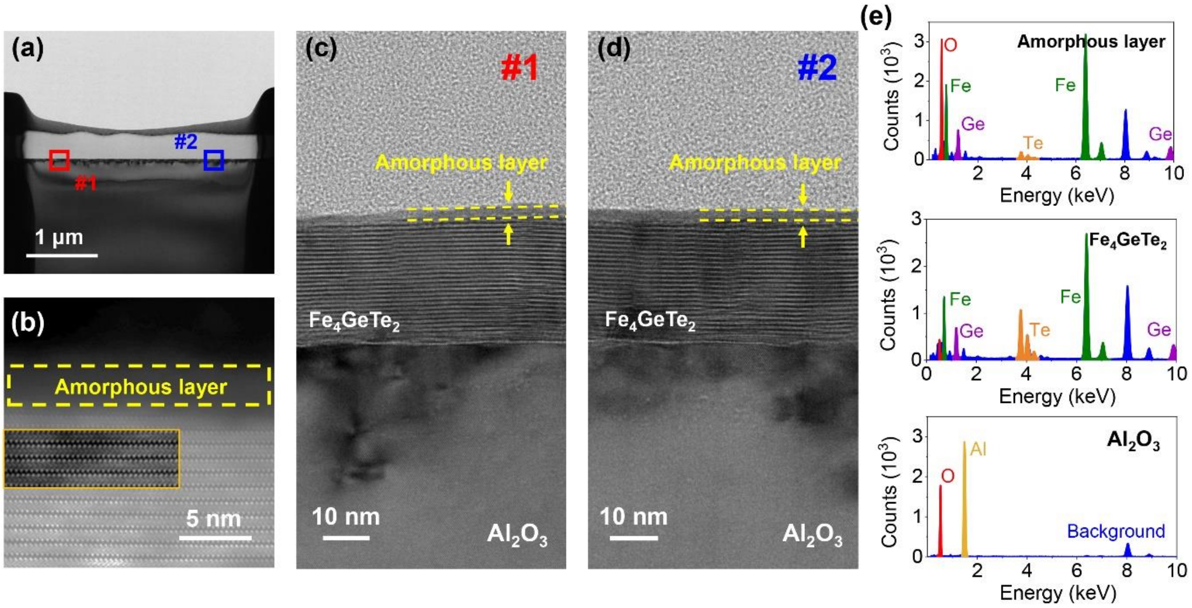

Figure 41. The TEM (a) and EDS (b) results for the Fe$_4$GeTe$_2$ thin film after 5 min Ar etching

Here, a Fe$_4$GeTe$_2$ film was prepared by MBE, followed by 5 min Ar etching to decrease the film thickness (~5 nm etching according to the calibration). Then focused ion beam (FIB) was used to prepare the sample for TEM characterization. As shown in Figure 41, an amorphous layer can be observed on the surface of the film after etching, which uniformly distributes on the sample surface with a thickness of ~2 nm, indicating the etching (or the thickness decreases) for the Fe$_4$GeTe$_2$ film is uniform. EDS spectrum for the etched sample indicates that the upper amorphous layer contains oxygen and a much lower Te/Fe ratio than the bottom Fe$_4$GeTe$_2$ layer (Figure 41e), which proves that the origin of the amorphous layer is a combined result of natural oxidation during the FIB preparation and the Te escape during the etching. However, this layer is limited to 2 nm and can be served as a buffer layer to prevent the underneath damage. Indeed, the bottom Fe$_4$GeTe$_2$ film can still maintain its good crystalline, as shown in Figure 41b. The same conclusion was obtained by Raman spectra, as shown in Figure 42. Raman is a surface-sensitive method that was used in large-scale crystal quality analysis for plasma-treated 2D materials[119,120]. For 8 nm Fe_4GeTe_2 film, the Raman signal does not show any peak shift, either before or after 4 min etching, indicating that the Fe_4GeTe_2 film retains its crystalline structures after plasma treatment.

As for the composition change induced by plasma, the in-situ XPS result (Figure 39) also shows the same peak positions after etching, indicating the etching did not lead to a chemical modification in the remained sample. More importantly, even if there is a contribution from the top damaged layer to the density of states, it should be etching-thickness independent, which does not match our UPS results. Therefore, we conclude that the observed localized state shift should come from the interfacial effect instead of the etching process, and the potential damage by etching is insignificant to our results.

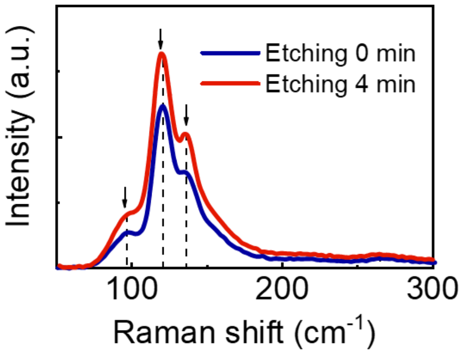

Figure 42. Raman spectra for 8 nm Fe_4GeTe_2 film before and after 4 min Ar etching

4.4 Chapter summary

After obtaining high-quality Fe_4GeTe_2, we found that the Fe_4GeTe_2 prepared in this paper has a T_c above room temperature. High-temperature magnetic characterization results confirmed that the magnetism of our Fe_4GeTe_2 still exists at 500 K, and a series of thickness-dependent experimental results show that this high-temperature ferromagnetic order comes from the interfacial effect between the thin film and the substrate. By simulating the electronic structure of the Fe_4GeTe_2/Al_2O_3 interface with first-principles calculations, we found that the shift of the density of state introduced by the orbital coupling from the interface is the reason for the increase in the T_c. Furthermore, we confirmed the existence of this interface effect by verifying the relationship between the shift of the Fe *d* electron local state and the interface through thickness-dependent photoelectron spectroscopy.

Chapter 5. Topological Insulators and Topological Interfacial Magnetism Manipulation

Following the groundbreaking discovery of graphene, there has been a global wave of interest in 2D materials. As the foundational research of 2D materials matures, their widespread application becomes increasingly important. Among these, topological insulators (TIs) based on bismuth chalcogenides have attracted extensive attention in recent years due to their efficient spin operation effects[63]. Topological insulators have a layered structure similar to graphene or Fe_4GeTe_2. Each layer is connected by weak van der Waals forces, hence, they belong to the family of 2D materials. The unique band structure confers TIs with many fascinating properties, such as massless Dirac fermions[122,123], helical edge states[65], spin-momentum locking[18,19], superconducting proximity effects[15,16], etc. Based on these effects, numerous new topological electronic devices have been developed, such as topological quantum devices, topological superconducting devices, topological terahertz devices, etc.

Due to the spin-momentum locked surface states and strong spin-orbit coupling effects, topological insulators are viewed as efficient spin-charge conversion materials, and are considered important for fabricating next-generation spintronic memories. If ferromagnetism is introduced into topological insulators to form magnetic topological insulators, it is hoped that a band gap can be opened on the existing surface states due to the broken time-reversal symmetry, thereby realizing the quantum anomalous Hall effect [61,65]. The interfacial magnetic proximity effect is a significant method to achieve these magnetic topological insulators, by combining topological insulator materials with magnetic materials into a heterostructure, ferromagnetism can be introduced into the topological insulator through the interfacial exchange effect[71-74]. Moreover, previous research has shown that the interfacial magnetic proximity effect can also enhance the magnetism of the adjacent magnetic materials[22,24,92], laying the groundwork for further enhancing the T_c of 2D magnets.

In this chapter, we will first discuss the ferromagnetism introduced into topological insulators by the interfacial effect. We first prepared a TI thin film by molecular beam epitaxy and characterized its morphology and crystal structure. After obtaining a high-quality TI thin film, we prepared a series of topological/ferromagnetic heterostructures and subsequently used electrical methods to quality the contribution of the interfacial effect on the heterostructure's magnetic properties and topological surface states. Finally, we used terahertz methods to study the surface state characteristics of the TI thin film. The main objective is to study the spin-charge conversion efficiency on the surface states and explore the possibility of using topological/ferromagnetic thin films to fabricate terahertz communication devices and spintronic memory devices.

5.1 Preparation and characterization of topological insulators

5.1.1 Thin film growth

To study the interfacial effects in TI and topological heterostructures, we first need to prepare the single TI think film by MBE system. Bi_2Te_3 and Bi_2Se_3 are two common TI materials from group V-VI, which has been proved to have great potential in various fields. This chapter includes studies on the preparation and physical properties of these two materials. Given that Bi_2Te_3 and Bi_2Se_3 share a similar structure, this section will focus on the preparation process and characterization results of Bi_2Te_3 as an example.

Considering that Bi_2Te_3 belongs to the rhombohedral crystal system (R-3m), we still choose sapphire (Al_2O_3-0001) as the substrate for the epitaxy. Similar to the epitaxial process of Fe_4GeTe_2, we use RHEED (Reflection High Energy Electron Diffraction) and quartz to monitor the growth process in-situ .

(1) Substrate cleaning and annealing: This step is the same as described in Chapter 3. After the substrate annealing is complete, the substrate temperature is restored to room temperature in preparation for the preparation of Bi_2Te_3.

(2) Bi, Te source heating: According to experimental needs, increase the current of the effusion cells of the Bi and Te sources. After the temperature is stable, use the quartz to measure the beam flux of the two elements. Since Bi_2Te_3 needs to be grown in a Te-rich environment,

we need to control the temperature of the two beams to maintain the beam flux ratio at Bi:Te=1:10.

(3) Preparation of Bi_2Te_3: According to previous reports, Bi_2Te_3 has poor adhesion on sapphire substrates. In this work, we adopt a two-step growth model to prepare the Bi_2Te_3 thin film. Firstly, adjust the substrate current to maintain the sample at a lower temperature (170°C) and grow a 1-2 nm Bi_2Te_3 film at this temperature. Then, keep the Te source on, turn off the Bi source, and raise the substrate temperature to the normal growth temperature (230°C). The purpose of this step is to prevent Te evaporation from the film during the heating process. When the substrate temperature reaches 230°C, open the Bi beam shutter to continue growing the remaining thickness.

(4) After the preparation is completed, close all effusion cells shutters and substrate shutters and lower all temperatures to room temperature. After the growth chamber environment is stable, transfer the sample to the load lock chamber and take out the sample.

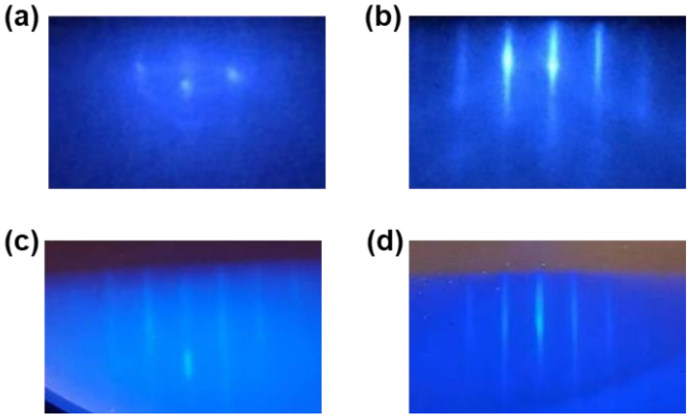

Figure 43. RHEED patterns during the growth: (a) Sapphire substrate-unannealed; (b) Sapphire substrate-annealed; (c) Few-layer Bi_2Te_3 grown at low temperature; (b) 10 nm Bi_2Te_3.

5.1.2 Structural and morphological characterization of Bi_2Te_3

Bi_2Te_3 is a type of V-VI group semiconductor, belonging to the mineral compound of bismuth telluride, and its crystal structure belongs to the hexagonal crystal system, with space group R-3m. Figure 44a illustrates the crystal structure of Bi_2Te_3, the fundamental unit of which is the QL layer composed of five atomic layers, each QL layer being 0.955 nm thick. Figure 44b presents the RHEED patterns of the prepared 10 nm Bi_2Te_3 and sapphire substrate, both showing clear single-crystal features. We then used XRD to characterize the crystal structure of the prepared Bi_2Te_3 thin film. All the peak positions in Figure 44c belong to the {003} crystal plane of $B_{i2}Te_3$ [63], proving that there were no impurify phases or lattice distortions during the growth process. Additionally, we employed AFM to characterize the surface morphology of the prepared Bi_2Te_3, as shown in Figure 44d. Similar to previous results, our Bi_2Te_3 samples possess smooth surfaces, exhibiting noticeable step-like features. Figure 44e shows the step height of the red line part in Figure 44d, each step is approximately ~1 nm, which is consistent with the thickness of a single QL layer of Bi_2Te_3(0.955 nm).

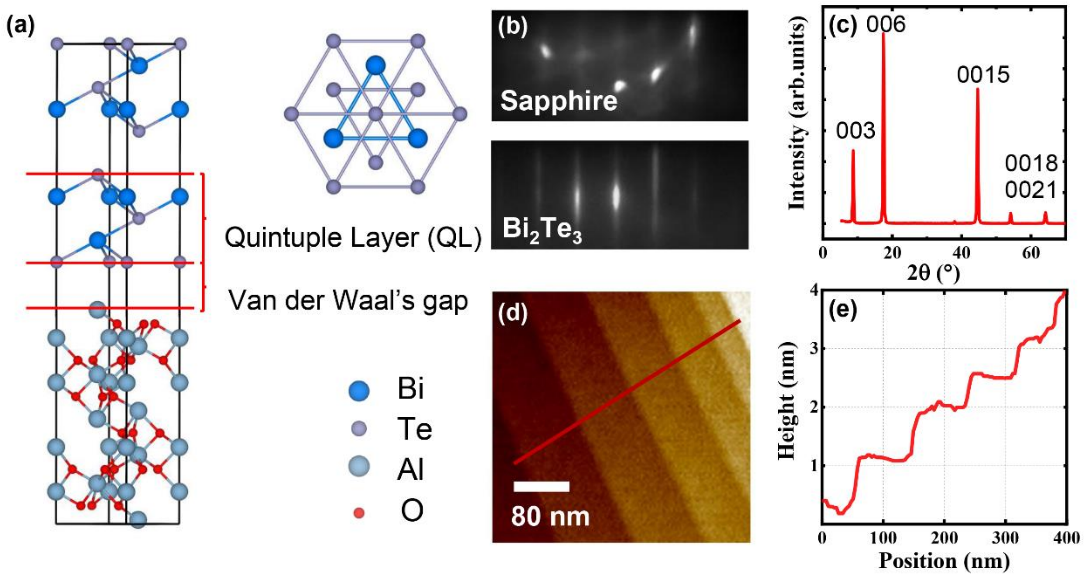

Figure 44. Morphological and crystal structural characterization of the 10 nm Bi_2Te_3

5.2 Interfacial effects of 2D topological heterostructures

Compared with 2D material system, the 2D magnetic material subsystem does not have a long history. In fact, before 2D magnets were obtained from experiments, the scientific community typically achieved 2D magnetism in the topological insulator Bi_2Se_3 via magnetic doping. Alternatively, the interfacial proximity effect is another method to achieve the 2D magnetism. Due to the strong spin-coupling effect of TI, when Bi_2Se_3 is combined with a magnetic thin film to form a 2D heterostructure, the *3d* orbitals in the magnetic material exchange-couple with the topological surface states, causing changes in the interfacial electronic structure, thereby introducing 2D ferromagnetic order into the TI layers. This interfacial effect is known as the "proximity effect." EuS/Bi_2Se_3 heterostructures were the first experimentally observed topological heterostructures with magnetic proximity effects, which was proved by Moodera *et al.* by polarized neutron diffraction. The long-range magnetic order in the EuS/Bi_2Se_3 heterostructures was introduced by the exchange-coupling effect in the interface, which could enhance the magnetism over room temperature and the T_c is far exceeding that of the topological ferromagnetic phase introduced by magnetically-doping TI[92,100]. Simultaneously, Moodera *et al.*'s experimental results also proved that the magnetic proximity effect not only introduces magnetism into the TI layer but can also effectively enhance the T_c of adjacent ferromagnetic layers. The fundamental mechanism is that the coupling between the topological surface states and ferromagnetic material enhances the spin interactions in the ferromagnetic layer, thereby strengthening its ferromagnetism. We will discuss this topic in detail in Chapter 7. Constructing topological magnetic heterostructures, studying the long-range magnetic order introduced in the interface, has significant implications for developing advanced spintronic devices. On the one hand, magnetic materials with topological characteristics are excellent materials for realizing quantum anomalous Hall effects, with the potential to realize novel spinteonic quantum devices. On the other hand, because the penetration depth of the proximity effect is only a few nanometers, the magnetism produced in heterostructures also exhibits 2D characteristics. Through suitable material selection and structural design, we can clarify the generation and manipulation mechanism of 2D magnetism. In this section, we have prepared a series of TI/ferromagnetic heterostructures and used electrical measurements to investigate the proximity effect in the interface.

Compared to Bi_2Te_3, Bi_2Se_3 has a lower resistivity and a larger bandgap, making it the best material for observing the magnetic proximity effect. Therefore, we chose Bi_2Se_3 as the TI layer material in the heterostructure[64]. After a comprehensive comparison of all ferromagnetic materials, we chose the ferromagnetic semiconductor (FMS) as the ferromagnetic layer material in the heterostructure. The FMS is a novel material doped with magnetic atoms in semiconductor materials (such as Ge, Si, etc.). Its ferromagnetism stems from the RKKY interactions within the material, so its ferromagnetism can be controlled by the external stimuli such as electric fields[124,125]. Simultaneously, the resistivity of the FMS can be precisely controlled by controlling growth conditions, which is beneficial for subsequent electrical measurements. Considering that the Mn_xGe_{1-x} and Bi_2Se_3 have a small lattice mismatch, we propose using Bi_2Se_3/Mn_xGe_{1-x} to study the magnetic proximity effect.

5.2.1 Preparation of Bi_2Se_3/Mn_xGe_{1-x} heterostructure

Considering the large lattice mismatch between the FMS Mn_xGe_{1-x} and the sapphire substrate, we chose GaAs (111) B as the substrate for the heterostructure. A 20 nm-thick Mn_xGe_{1-x} thin film was grown on a commercial GaAs (111) B substrate in our MBE system. Inheriting the structure of Ge crystal, Mn_xGe_{1-x} has a cubic crystal structure with a lattice constant of 5.65Å. Here the Mn doping concentration of Mn_xGe_{1-x} is around 4% and each Mn atom randomly occupies the position of Ge in the unit cell, as shown in Figure 45a. Then 8 nm Bi_2Se_3 was deposited on the Mn_xGe_{1-x} to fabricate a heterostructure. Here, the substrate temperature was strictly controlled at 200 ºC. Otherwise, a Ge-Se impurity phase will be formed. X-ray diffraction (XRD) was employed to characterize the crystal structure of the heterostructure and a typical result is shown in Figure 45b. Mn_xGe_{1-x} {111} peak exhibits the strongest intensity and other diffraction peaks correspond to Bi_2Se_3 {003} family planes (according to the PDF card of #15-0863), indicating that no other impurity phase was formed.

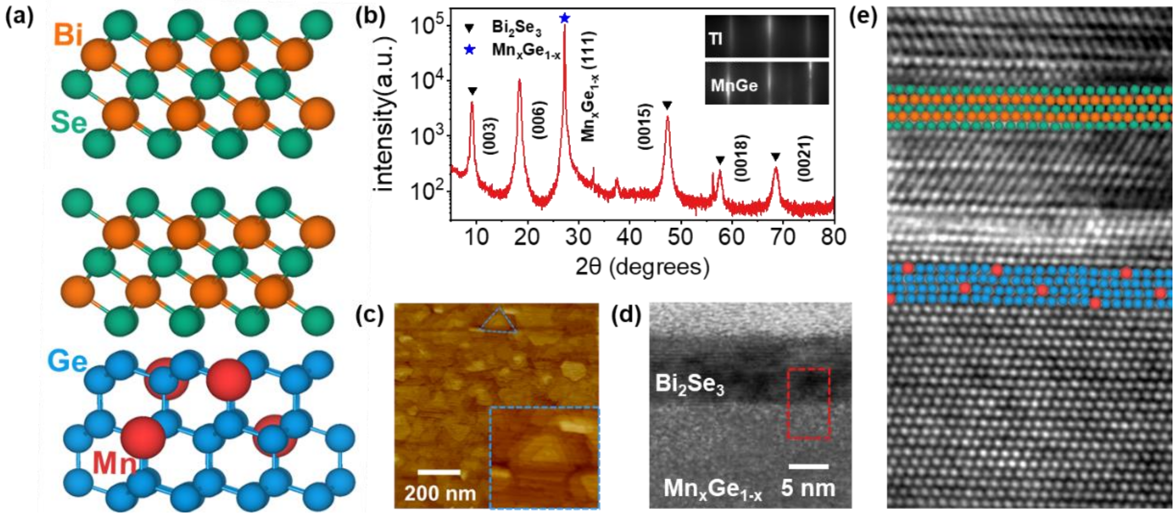

Figure 45. Characterization of the Bi_2Se_3/MnxGe1-x (x=0.04) heterostructure

During the growth, reflection high-energy electron diffraction (RHEED) was used to monitor the deposition, and the pattern of the heterostructure was shown in the inset of Figure 1b. For the initial growth, a sharp streaky RHEED pattern of Mn_xGe_{1-x} thin film could be observed, indicating a smooth surface morphology. The lattice mismatch of Mn_xGe_{1-x} and Bi_2Se_3 is 3.6%, which is relatively smaller than other substrates for Bi_2Se_3, and the Van der Waals growth of topological insulators helps the heterostructure to overcome the mismatch, promising the perfect quality of the interface. After growth, a streaky pattern can be also observed from the Bi_2Se_3 film, demonstrating a 2D surface of the Bi_2Se_3 film. The perfect surface morphology was further confirmed by atomic force microscopy (AFM), as shown in Figure 45c, which shows a typical terrace structure similar to already reported TI results. The quality of the interface was investigated by high-resolution transmission electron microscopy (HRTEM), as shown in Figure 45d and Figure 45e. The HRTEM result demonstrates a thin amorphized gap of 6 Å, above which the first Bi_2Se_3 layer develops. Except that, our heterostructure has a good crystal structure for Mn_xGe_{1-x} and Bi_2Se_3 layers.

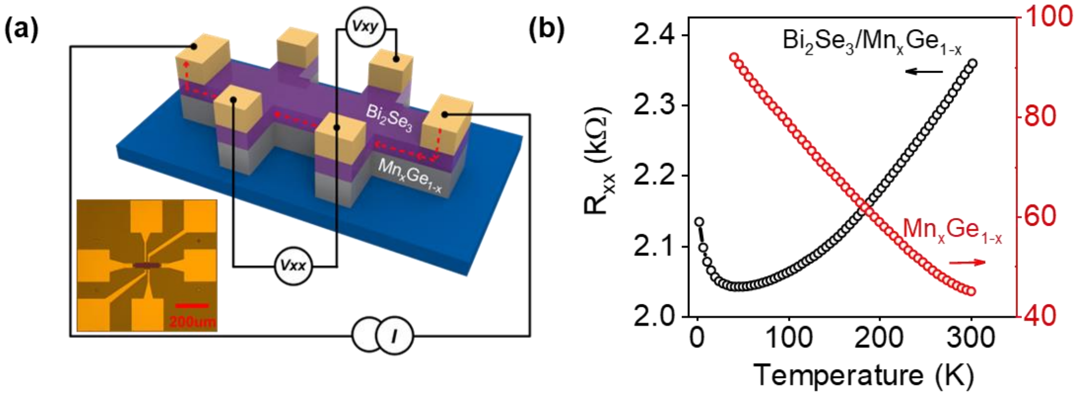

Figure 46. Transport measurement results of Bi_2Se_3/Mn_xGe_{1-x} heterostructure: (a) Schematic diagram of the Hall bar structure; (b) Resistance-Temperature (R-T) curve of the heterostructure

5.2.2 Transport measurement of the Bi_2Se_3/Mn_xGe_{1-x} heterostructure

To investigate the magnetic property of the heterostructure, the sample of $Bi_2Se_3(8)/Mn_xGe_{1-x}(20)$ ($x=0.04$) was fabricated into a micrometer-sized Hall bar device (shown in Figure 46a), and the physical property measurement system (PPMS) was employed to carry out the transport measurement. For clarity, an 8 nm-thick Bi_2Se_3 and 20 nm-thick Mn_xGe_{1-x} (x=0.04) thin film on Ge (111) substrate was measured as control groups. Due to the deliberate manipulation of the stoichiometry during the sample preparation, the conductance of the Mn_xGe_{1-x} layer was tuned to minimize to promise the current flow mainly from the Bi_2Se_3 layer in the heterostructure, as shown by the red line in Figure 46a. Figure 46b shows the temperature-dependent resistance (R-T curve) of the Bi_2Se_3/Mn_xGe_{1-x} heterostructure and Mn_xGe_{1-x} respectively. The resistance of Mn_xGe_{1-x} is much larger than the heterostructure, proving that the transport property of the bilayer is dominated by Bi_2Se_3's conductance channel. Notably, the heterostructure resistance decreases as the temperature decrease from 300 K to 50 K, manifesting a metallic behavior, which was also observed in pure TI[126,127]. When the temperature is below 50 K, the resistance increases as the temperature decrease because the bulk carriers in Bi_2Se_3 begin to freeze out and the surface channel dominates the conductance of the heterostructure. Figure 47a shows the temperature-dependent MR of the heterostructure, which presents a sharp negative cusp until 150 K, which belongs to the typical WL behavior. However, for pure Bi_2Se_3, the MR curve should present a positive cusp because of the π-Berry phase in topological surface states. In the quantum diffusion regime, the quantum interferences in magnetic samples have a strong contribution to current, leading to an enhancement of the probability of electron backscattering as well as the resistance, which is the reason for WL and its contribution on conductance is called quantum correction. However, for topological surface states with a π-Berry phase, this interference can be destroyed by the strong spin-orbital coupling, decreasing the probability of electron backscattering occurs and resulting in an overall decrease of electrical resistance, which was called weak-antilocalization effect (WAL), but the WL can be recovered through breaking the π-Berry phase by introducing a magnetism[128]. Thus, we conclude that such WL curves in Figure 47a come from the induced magnetism in the heterostructure, and the T_c of the magnetism is over 150 K.

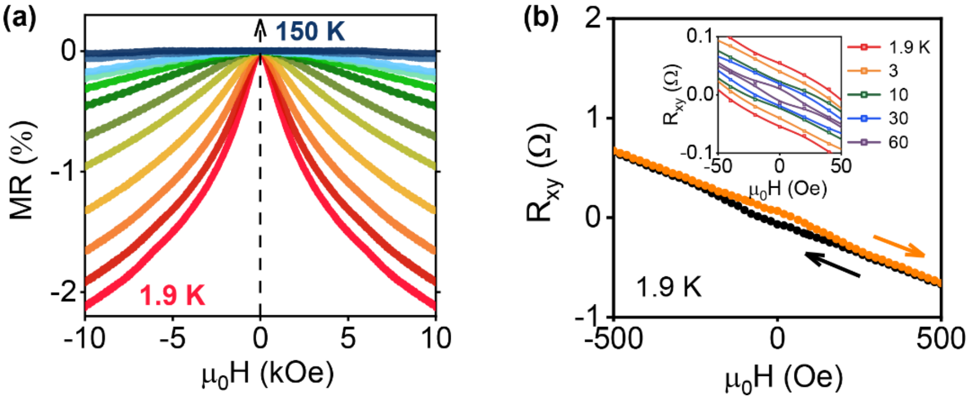

Figure 47. Hall curves and MR curves of the Bi_2Se_3/Mn_xGe_{1-x} Heterostructure

Considering the leading role of Bi_2Se_3 in the heterostructure conductance, we extracted the anomalous Hall signal to study the magnetic property of the Bi_2Se_3 layer, as shown in the inset of Figure 47b. For the magnetic sample, the Hall resistivity (R_{xy}) could be divided into two parts: $R_{xy}=R_o\cdot H+ R_A\cdot H$. Here, H is the magnetic field, M presents the magnetization, R_o and R_A are the coefficients of ordinary Hall and anomalous Hall effect (AHE) respectively. Within a small external field, the AHE component determines the Hall resistivity and manifests the magnetic property of the sample. For the heterostructure, the square anomalous Hall curves until 60 K indicate that magnetism is induced in the Bi_2Se_3 layer. Considering that no hysteresis loop was observed in pure Bi_2Se_3, the magnetism in the Bi_2Se_3 layer may come from the interfacial effect or the Mn migration from the Mn_xGe_{1-x} layer. However, previous reports have never observed the AHE in Mn-doped Bi_2Se_3 when the temperature is over 5 K[69,70]. Therefore, we conclude that the interfacial proximity is the reason for the magnetism in Bi_2Se_3. The inversed AHE curve could be evidence for this conclusion, in which the forward and reverse branch is shifted in opposite direction along the magnetic field as compared to normal hysteresis. In this work, due to the antiferromagnetic coupling between Bi_2Se_3 and Mn_xGe_{1-x}, the proximity-induced opposite magnetization will lead to a negative-sign AHE signal.

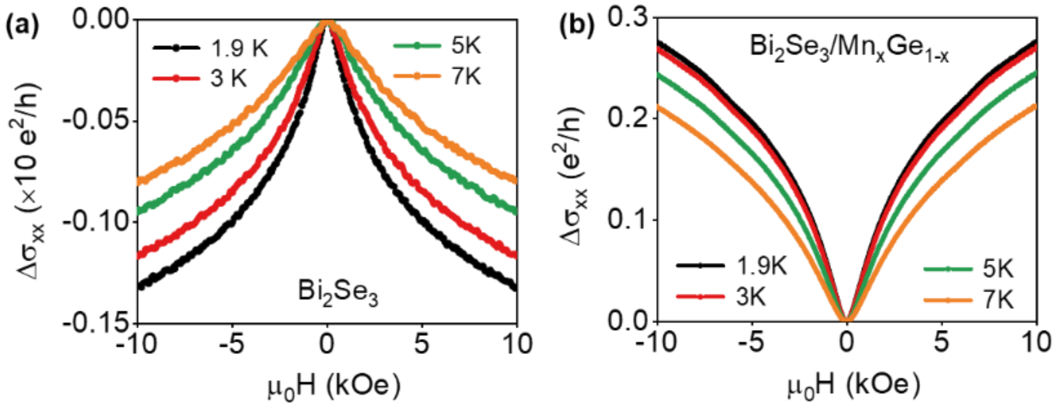

Figure 48. The transition from WAL to WL in pure Bi_2Se_3 and Bi_2Se_3/Mn_xGe_{1-x} (x=0.04)

5.2.3 Proximity-induced magnetism

To quantitatively understand the relation between the proximity-induced ferromagnetism and the TRS-protected topological surface states, the magnetoconductivity (MC) $\Delta\sigma(B)=\sigma(B)-\sigma(0)$ of pure Bi_2Se_3 and the heterostructure were investigated respectively. Due to the bulk freezing at low temperatures, the conductance of TI is dominated by surface states and should exhibit a WAL feature. Therefore, as shown in Figure 48a, all MC curves in pure Bi_2Se_3 film display a typical negative cusp. Such behavior can be fitted via the single-component Hikami−Larkin−Nagaoka (HLN) formula[129]:

$$\Delta\sigma(B)=\frac{\alpha e^2}{2\pi^2\hbar}[\psi(\frac{l_B^2}{l_\phi^2}+\frac{1}{2})-\ln(\frac{l_B^2}{l_\phi^2})] \tag{5.1}$$

Here, ψ is the digamma function; l_ϕ is the phase coherence length; l_B is the magnetic length which can be given by: $l_B=(\hbar/4e|B|)^{1/2}$; α is the WAL perfector that quantity its contribution to the quantum interference. For ideal TI with surface states, the maximum value of α is -0.5 because there is only one WAL channel dominates the conductance. In this work, fitting to the MC data by the HLN formula yields an α near -0.4, as shown by the blue line in Figure 49b. This value is slightly higher than the ideal value, which may be contributed to the defects in the surfaces of Bi_2Se_3[128].

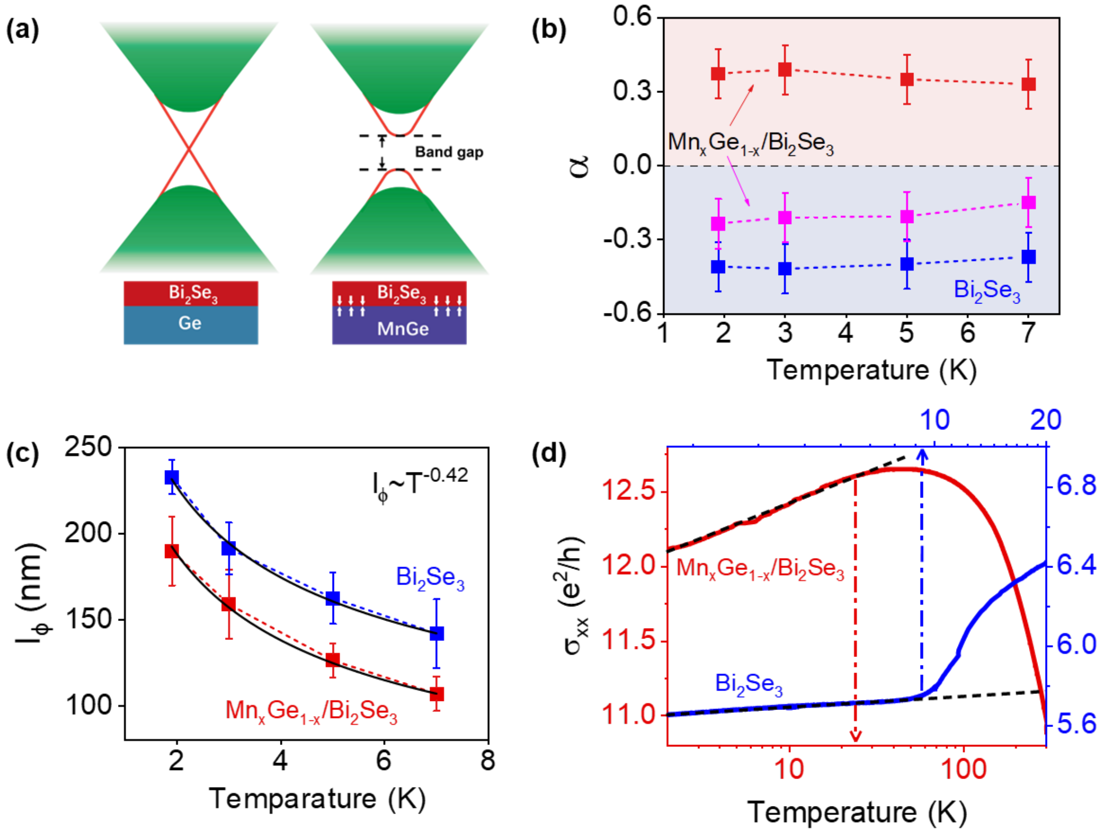

Figure 49. The contribution of the proximity-induced magnetism on TI surface states

By contrast, after integrating with the Mn_xGe_{1-x} layer, the magnetism induced by the proximity effect in Bi_2Se_3 changes the negative cusp to positive due to the TRS breaking (Figure 48b), and the data cannot be simply captured by Eq. (5.1) because the exchange gap opened in the surface states leads to a WL component while suppressing the WAL effect. To distinguish the contribution of these two effects, a two-component HLN formula is employed as[128,130]:

$$\Delta\sigma(B)=\sum_{i=1,2}\frac{\alpha_i e^2}{2\pi^2\hbar}\left[\psi\left(\frac{l_B^2}{l_{\phi i}^2}+\frac{1}{2}\right)-\ln\left(\frac{l_B^2}{l_{\phi i}^2}\right)\right] \tag{5.2}$$

Here, the magnetoconductivity consists of two ingredients: i=1 and i=2 represent the contribution of WAL and WL respectively; α_i and $l_{\phi i}$ are the corresponding perfector and phase coherence length. When the surface state is gapless, the system falls in the WAL regime with α_1=-0.5 and α_2=0. If the surface state gap is opened by the magnetism, the quantum correction can be driven into the WL regime α_1=0 and α_2=0.5.

Following Eq. (5.2), the transition from WAL to WL for the pure Bi_2Se_3 and the heterostructure can be identified by extracting the perfector α as well as the phase coherence length l_ϕ from fitting the MC in Figure 48a and Figure 48b, and all the fitting parameters are plotted in Figure 49b and Figure 49c. Different from the pure Bi_2Se_3 in which the WAL perfector α_1 keeps close to -0.5, the α_1 for the heterostructure decease to -0.2, indicating the suppressed WAL component, while the WL begins to dominate the conductance channel with a perfector α_2=0.3~0.4. This transition from WAL to WL confirms the magnetism induced by the proximity as well as the TRS breaking in the surface states in the Bi_2Se_3 layer of the heterostructure. Despite the temperature changes, the α value for the heterostructure stays almost constant, demonstrating the strong proximity effect. In contrast, l_ϕ varies with temperature, which can be described by a power law function as $T^{-\beta}$, here the ideal value of β is near 0.5 in 2D systems[131]. In this work, the extracted l_ϕ^{TI} and $l_\phi^{Bilayer}$ in the WAL component well match such power law function with a β~0.42, demonstrating that the carrier transport is mostly 2D-like in the Bi_2Se_3 layer. The value of $l_\phi^{Bilayer}$ is slightly lower than l_ϕ^{TI}, which is because the vanish of the Berry phase reduces the phase coherence length in quantum diffusive transport. After integrating with Mn_xGe_{1-x}, the crossover from WAL to WL in the Bi_2Se_3 layer demonstrates the presence of the surface bandgap due to the magnetism induced by the proximity effect, as shown in Figure 49a.

Here we calculate the quantum correction on the conductance induced by WAL and WL components in the heterostructure, then the calculated value is compared with the experimental values to verify the accuracy of our fitting results. Figure 49d shows the temperature-dependent conductivity for pure Bi_2Se_3 and Bi_2Se_3/Mn_xGe_{1-x} heterostructure, both curves present a logarithmical increase within the low-temperature region. Such logarithmic behavior results from the combined effect of quantum corrections induced by WAL, WL, and electron-electron interaction (EEI) effects[132,133]. In general, the quantum correction from WAL and WL can be described as[132]:

$$\Delta\sigma_{\mathrm{xx}}^{\mathrm{WAL(WL)}} = \frac{\alpha_i \beta_i e^2}{\pi^2 \hbar} \ln(\frac{T}{T_L}) \tag{5.3}$$

where T_L is the characteristic temperature when the quantum correction vanishes, and α_i and β_i are the factors fitted from Eq. (5.2), i=1 represents the WAL component and i=2 stands for the WL component. Following this equation, the contribution of quantum correction from WAL in pure Bi_2Se_3 ($\Delta\sigma_{xx}^{TI}$) and the heterostructure ($\Delta\sigma_{xx}^{Bilayer}$) can be calculated by adopting the extracted α_i and β_i values from Figure 49b and Figure 49c. Notably, due to the leading role of WAL in Bi_2Se_3's transport channel, the conductance is expected to present a negative slope with the temperature increases because of the negative WAL perfector. However, the pure Bi_2Se_3 shows a conductance increase in the quantum diffusive regime (Blue line in Figure 49d). Previous reports have indicated the additional conductance increase comes from the electron-electron interaction (EEI) term $\Delta\sigma_{xx}^{EEI}$ in Bi_2Se_3 thin film[132,133], which will cause an increase in the surface conductance. Therefore, the overall conductance variation for pure Bi_2Se_3 in the quantum can be described as $\Delta\sigma_{xx}^{TI}=\Delta\sigma_{xx}^{WAL}+\Delta\sigma_{xx}^{EEI}$. Here the value of $\Delta\sigma_{xx}^{TI}$ can be estimated by Eq. (5.3) as 0.12 e^2/h, while $\Delta\sigma_{xx}^{WAL}$ can be calculated using the parameter obtained in Eq. (5.1) as $\Delta\sigma_{xx}^{WAL}$=-0.07 e^2/h. Finally, the quantum correction of EEI can be calculated as 0.19 e^2/h. Along this line, in Bi_2Se_3/Mn_xGe_{1-x}, the contribution of WAL and WL can be calculated using the fitting parameter from Eq. (5.2) as $\Delta\sigma_{xx}^{WAL}$=-0.06e^2/h and $\Delta\sigma_{xx}^{WAL}$=0.26e^2/h, while the overall quantum correction is $\Delta\sigma_{xx}^{Bilayer}=\Delta\sigma_{xx}^{WL}-\Delta\sigma_{xx}^{WAL}+\Delta\sigma_{xx}^{EEI}$=0.39 e^2/h. This value is very close to the experiment value in Figure 49d ($\Delta\sigma_{xx}^{Bilayer}$~0.4 e^2/h), confirming the accuracy of our fitting results in the quantum interference picture, which are correlated to the proximity-induced magnetic order in the Bi_2Se_3 film. Figure 49a shows the band structures of pure Bi_2Se_3 and Bi_2Se_3/Mn_xGe_{1-x} heterostructures. Considering the relatively small proximity length, we propose that the bandgap is opened in the Dirac cone of the bottom surface. Meanwhile, the bandgap induced by the magnetism in the surface state can be identified with the obtained α_1 and α_2 in Eq. (5.2) because the perfectors of WAL and WL in Bi_2Se_3 are explicit functions of gap size Δ and Fermi level E_F[134], as discussed in the next section. After careful examination, the E_F position of the Bi_2Se_3 layer is calculated to be 113 meV at 1.9 K, and the opening bandgap size is 80 meV, this value is comparable to that of Bi_2Se_3 film with magnetic doping ($\Delta\approx$75 meV).

5.2.4 Estimation of the surface state gap size

In the heterostructure, both the WAL perfector α_1 and WL perfector α_2 in the quantum interferences are related to the band gap in the surface states and the Fermi level E_F. Specifically, α_1 and α_2 can be expressed as[134]:

$$\alpha_1 = -\frac{a^4 b^4}{(a^4+b^4)(a^4+b^4-a^2b^2)} \tag{5.4}$$

$$\alpha_2 = \frac{(a^4+b^4)(a^2-b^2)^2}{2(a^4+b^4-a^2b^2)^2} \tag{5.5}$$

Here $a \equiv \cos\frac{\Theta}{2}$, $b \equiv \sin\frac{\Theta}{2}$, and $\cos\Theta \equiv \frac{\Delta}{2E_F}$. Obviously, either α_1 or α_2 is determined by the bandgap size (Δ). In topological surface states, the band is gapless with $\cos\Theta \to 0$, then the conductance channel is dominated by the WAL effect with α_1=-1/2 and α_2=0. By contrast, if a surface state gap is opened by magnetism, and the Fermi level locates in the gap ($\cos\Theta \to 1$), the quantum correction can be driven into the WL regime with α_1=0 and α_2=1/2. In addition, the Fermi level position relative to the Dirac point E_F can be estimated by the formula[135]:

$$E_F = \hbar / (2m^*)(3\pi N_{BD})^{2/3} \tag{5.6}$$

Here the effective mass m^* is assumed to be $m^* \approx 0.15 m_e$, and the bulk carrier density N_{BD} at 1.9 K can be extracted as 9.4×10^{18} cm^{-2} from Figure 47b. Therefore, the E_F of Bi_2Se_3 in the heterostructure is fixed approximately at ~0.113 eV. Finally, by using the value of E_F and the obtained α_1, α_2 in Figure 4a, the surface state bandgap of the Bi_2Se_3 layer is estimated to be $\Delta\approx$ 80 meV at 1.9 K.

5.3 Topological surface states and interfacial spin-related effects

The topological surface states endow TIs with many special properties. Studying the spin manipulation characteristics of topological surface states is an important direction to realize ultra-low power consumption spintronic devices and quantum computing devices. Experimentally, angle-resolved photoemission spectroscopy (ARPES) is often used to directly observe the surface band structure of TI, as shown in Figure 50[136]. In the *E-k* band diagram, due to spin-orbit coupling, the TI bulk band is reversed to form a spin-polarized topological surface state. The electron spins on the left and right surface state bands are perpendicular to the *E*-*k* plane and the spin polarization directions are opposite. Due to time reversal symmetry protection, when the surface state electron momentum changes from *k* to -*k*, its spin direction will also change accordingly. This is the origin of the spin-momentum locking feature. Therefore, TI material can achieve efficient conversion between spin current and charge current. Experimentally, the spin Hall angle (θ_{SHE}) is often used to describe the charge-spin conversion ability of a material. The θ_{SHE} of TIs is much larger than that of ordinary heavy metals, so it can be used to achieve efficient spin current utilization, and then achieve efficient spin terahertz (THz) emission[137,138].

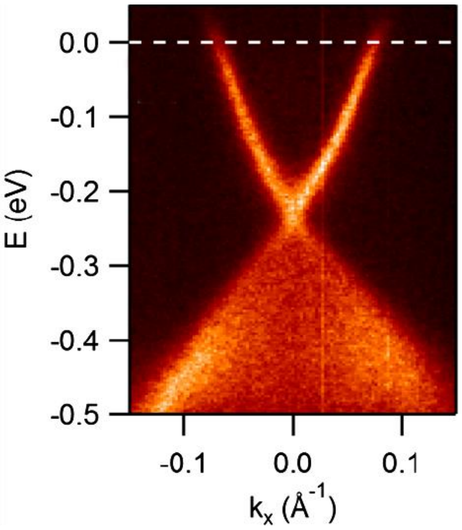

Figure 50. The surface band structure of Bi_2Se_3 measured by ARPES [136]

5.3.1 Photovoltaic characterization of surface states

In Section 5.2, we introduced that how to characterize the TI surface states by electrical measurement, that is, quantifying the surface band gap by analyzing the transition of the magnetoresistance curve from WAL to WL. However, electrical measurement often needs to be carried out at low temperatures and requires patterning of the film. In recent years, optoelectronic methods mainly based on terahertz (THz) detection have provided a new way to measure the TI surface states. Compared with traditional electrical methods, the optoelectronic testing system is simple, does not require device preparation, and can characterize already packaged film samples. The previous research has confirmed that by using a specific polarized femtosecond laser to excite the TI film, and measuring its THz emission through a terahertz time-domain spectroscopy system (THz-TDS), its surface states can be characterized[139-142].

Figure 51 shows a schematic diagram of the THz-TDS system used in this work. This system uses a commercial laser as a femtosecond laser source, with a laser center wavelength of 800 nm, a pulse width of 100 fs, and a repetition rate of 80 MHz. After the laser pulse is emitted from the laser, it is divided into a pump light and a probe light by a beam splitter, and irradiated onto the sample to be tested and the ZnTe crystal respectively. After the sample is excited by the pump light, the sample will emit a THz signal, which is reflected to the ZnTe crystal after a series of processing. According to the electro-optic effect, the ZnTe crystal will decompose the probe light into two polarized lights with different polarization directions. By measuring the light intensity of the two polarized lights, the magnitude of the THz emitted by the sample can be calculated. Furthermore, by adjusting the time delay between the pump light and the probe light, the time-domain change of the THz signal can be measured.

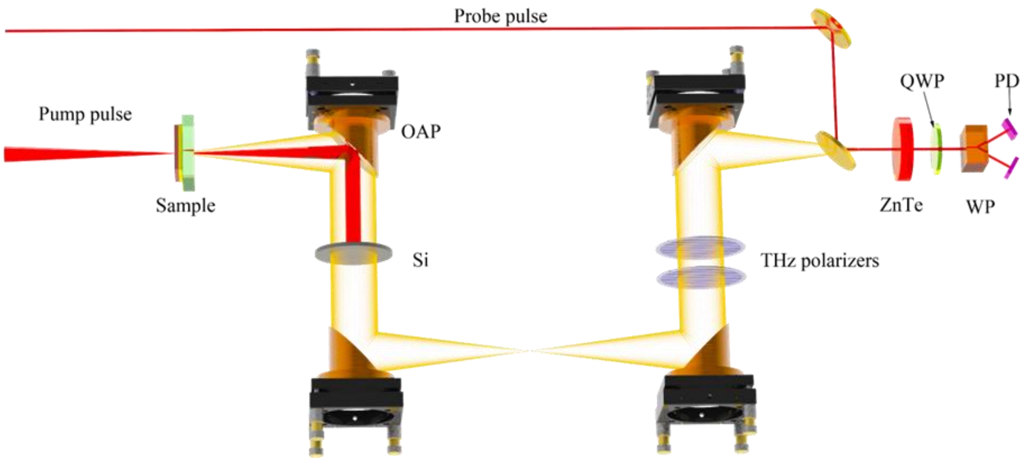

Figure 51. THz-TDS system used in this work

Figure 52a shows a schematic diagram of the THz emission achieved by exciting a Bi_2Te_3 film with a femtosecond laser. Due to the spin texture of the topological surface state, a specific chiral circularly polarized femtosecond laser can selectively excite a specific spin current. Moreover, due to the spin-momentum locking of the surface state, this asymmetric distribution of spins will be converted into an ultrafast photocurrent perpendicular to the spin direction[139]. This process is called the circular photogalvanic effect (CPGE), which can be explained by the following phenomenological formula:

$$j_{CPGE} = \gamma_{\lambda\mu} i(\boldsymbol{E} \times \boldsymbol{E}^{*})\mu \tag{5.7}$$

Here, j_{CPGE} represents the ultrafast photocurrent generated by the topological surface state, and $\boldsymbol{E}$ represents the electric field magnitude of the femtosecond laser. Since the frequency of the ultrafast photocurrent j is in the terahertz band, the Bi_2Te_3 film can achieve THz emission under the excitation of a femtosecond laser. Obviously, when the pump light is linearly polarized, $\boldsymbol{E} \times \boldsymbol{E}^{*} = 0$. Therefore, only circularly polarized light can induce the production of CPGE current. At the same time, because the polarities of the CPGE currents excited by left-handed (σ^{+}) and right-handed (σ^{-}) light are opposite, the contribution of CPGE can be obtained by selecting the THz signal that shows a 180° period with the rotation angle of the 1/4 wave plate, and the photoelectric response signal of the topological surface state can be finally calculated.

Figure 52b, c shows the THz response of a 10 nm Bi_2Te_3 film under the excitation of left-handed and right-handed circularly polarized femtosecond lasers. Obviously, S_{xy} represents THz radiation generated by the CPGE current from the topological surface state; on the contrary, the polarity of S_{xy} does not change with the chirality of the pump light, and this component may come from the THz radiation generated by the built-in electric field of Bi_2Te_3 (this effect is called linear photogalvanic effect, LPGE)[139]. After obtaining the photoelectric response of the TI surface state, our next plan is to characterize the aforementioned Bi_2Se_3/Mn_xGe_{1-x} heterojunction using the THz method, striving to quantify the contribution of the interfacial magnetic proximity effects on topological surface states using optical method. Past research has proven that THz-TDS is an efficient method of characterizing the surface band structure of TI. By exciting the sample with a femtosecond laser and calculating the THz radiation electric field generated by the surface CPGE, various information about the surface state can be obtained, such as the surface band structure, surface carrier mobility, spin asymmetric scattering rate, etc[140-142].

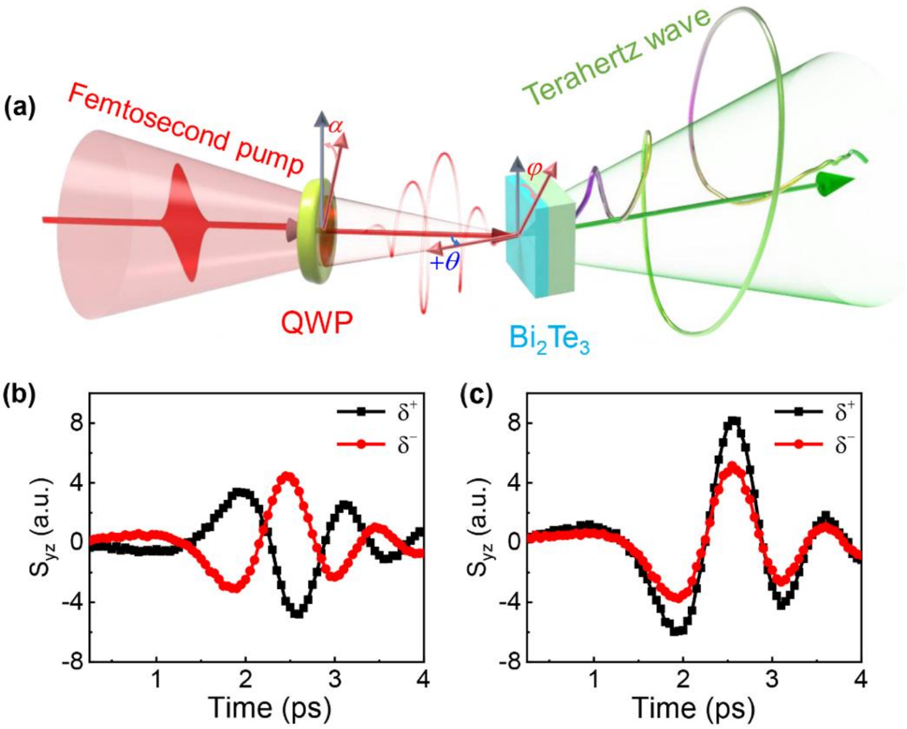

Figure 52. The THz emission for 10 nm Bi_2Te_3 film.

5.3.2 Spin-charge conversion of the TI surface states

Recently, there has been growing interest in achieving efficient THz emission using ferromagnetic/heavy metal heterostructures. Due to the imbalance of spin-up and spin-down electrons in the ferromagnetic layer material, an ultrafast spin current can be generated when excited by femtosecond laser pulses, which is then injected into the non-magnetic layer. This process is known as spin super-diffusion[143]. Since the frequency of the super-diffusive spin current is at the sub-picosecond level, it is converted into an ultrafast charge current by the spin-orbit coupling effect of the non-magnetic layer material after the spin current is injected from the ferromagnetic layer into the adjacent non-magnetic layer. This leads to efficient terahertz emission, which can be expressed by the following equation:

$$\vec{E}_{\mathrm{THz}} \propto \vec{j}_c \propto \theta_{\mathrm{SHE}} \cdot \vec{j}_s \times \overrightarrow{M} / \left|\overrightarrow{M}\right| \tag{5.8}$$

Here, $\vec{E}_{\mathrm{THz}}$ represents the radiated THz electric field, $\vec{j}_c$ represents the converted ultrafast charge current, $\vec{j}_s$ represents the ultrafast spin current generated by the ferromagnetic layer, and M represents the magnetization of the sample. Because this THz comes from the spin-charge conversion process in the interface, it is called spin THz. Unlike the THz emission in TI surface states, spin THz does not depend on the chirality of the pump light, and its intensity depends on the spin-charge conversion ability of the non-magnetic layer (i.e., the spin Hall angle θ_{SHE}). Due to the spin-momentum locking characteristics of TI material, its θ_{SHE} is more than 10 times that of traditional heavy metal materials (Bi_2Se_3=1.75, Pt=0.08, W=0.4) [144,145]. Thus, TIs are considered important materials for replacing heavy metals in achieving efficient spin THz emission [146]. By constructing a ferromagnetic/topological insulator heterostructure and studying its spin THz emission capability, we can perform a qualitative study of the SCC process on the TI surface.

In this paper, we prepared a series of Bi_2Te_3/CoFeB and CoFeB/heavy metal heterostructures and measured the spin THz emission capabilities of different samples using THz-TDS system. The results are shown in Figure 53[147]. Compared with the classic spin THz emitter W(1.8)/CoFeB(3)/Pt(1.8), Bi_2Te_3(10)/CoFeB(3) has almost the same level of THz intensity. To rule out the photocurrent effect in Bi_2Te_3 or the THz emission caused by the ultrafast demagnetization in CoFeB, we also compared the THz emission capabilities of pure Bi_2Te_3 and CoFeB thin films. Compared with the topological heterostructures, the THz emission from the single layer thin films is almost negligible. This conclusion confirms the great potential of TI materials as spin or charge converter. Since the SCC process occurs on the TI surface, our results prove that it is possible to achieve efficient spin control by constructing a FM/TI heterostructure and utilizing the interface SCC effect, which lays the foundation for future exploration of spintronic memory devices based on TIs.

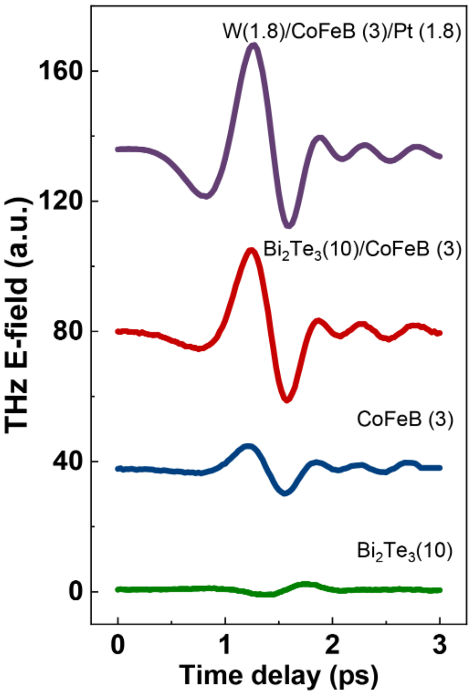

Figure 53. Quantifying the spin-charge conversion of different materials by THz method

5.4 Chapter summary

In this section, we mainly investigated the magnetism introduced by interfacial effects in FM/TI heterostructures. We first prepared a series of Bi_2Se_3/MnGe heterostructures using MBE and then characterized the quality of the heterostructures by multiple morphology and crystal structure characterization methods. After obtaining high-quality heterostructures, we tested the magnetic transport properties of the samples by electrical measurements. After integrating with MnGe, the transport properties of Bi_2Se_3 changed from the original WAL to WL, confirming that a magnetism can be introduced into t Bi_2Se_3 by interfacial effects. Further analysis proved that the long-range magnetic order introduced by the interfacial magnetic proximity opened a gap on the TI surface states. This finding not only contributes to the study of the generation and control of 2D magnetism but also lays the foundation for realizing quantum spintronic devices at high operating temperatures in the future.

Subsequently, we studied the TI surface states by THz measurements. We first quantified the photoelectric effect of TI surface states by measuring the THz response of single Bi_2Se_3 film. Further, we prepared Bi_2Se_3/Fe heterostructures and measured their spin-charge conversion capability by THz-TDS system. The results proved that the spin Hall angle of TI material is larger than that of traditional heavy metal materials, demonstrating great application potential.

Chapter 6. Interfacial Magnetism Manipulation in 2D Magnetic Topological Heterostructure

Due to the low-dimensional characteristics of 2D materials, they exhibit high sensitivity to external stimuli. Therefore, through the construction of 2D heterostructure and the introduction of interfacial effects, the magnetic[11-14], electric[15,16], and optical properties[17] of 2D magnets can be effectively manipulated. In 2D magnet, the introduction of interfacial effects can also enhance the spin interactions of the material, thereby increasing the T_c. Previous research has proven that in 2D magnetic heterostructure, the magnetic properties of the 2D magnetic layer[11-14], including T_c, magnetization, and coercivity field, can be tunned through the interfacial exchange interactions.

Based on the previous research results, the main content of this chapter is to prepare 2D magnetic heterostructure with high working temperatures and high spin manipulation efficiency. The heterostructure is composed of an FGT film and a high-quality TI film. Due to the strong orbital coupling of the TI material, there is a strong exchange coupling at the FGT/TI heterostructure, which can significantly enhance the magnetism of the FGT layer. Our work demonstrates that by changing the film structure of the heterostructure, such as film thickness or doping concentration, the interfacial effect can be effectively regulated. Furthermore, through THz method, we have demonstrated that the FGT/TI heterostructure has a high spin-charge conversion efficiency. Combined with its easily controllable interfacial effects, 2D magnetic heterostructure are expected to be used in the preparation of low-power magnetic memory or high-efficiency spintronic THz devices.

6.1 Preparation and characterization of Fe_3GeTe_2/Bi_2Te_3 heterostructure

In order to study the magnetism enhancement induced by the interface in FGT/TI heterostructure, we did not immediately choose Fe_4GeTe_2 but first selected Fe_3GeTe_2 as the magnetic layer of the heterostructure. As discussed in Chapter 4, Fe_4GeTe_2 itself has strong magnetism (intrinsic T_c=270 K), and its long-range magnetic moment is not limited by the dimensionality effect, but rather interacts with the substrate interface, thereby further increasing its T_c. In contrast, the T_c of Fe_3GeTe_2 is lower and is limited by the dimensionality decrease. As shown in Figure 54, previous research has shown that the T_c of bulk Fe_3GeTe_2 is close to 200 K, while this value for few-layer Fe_3GeTe_2 is reduced to 30 K [46]. This thickness dependency of Fe_3GeTe_2 provides an excellent platform for studying the interfacial effect.

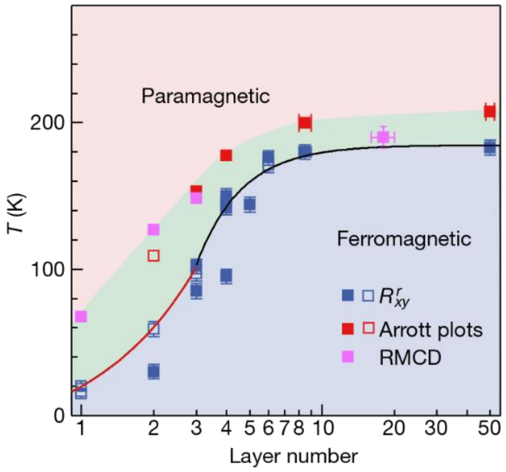

Figure 54. Thickness-dependent T_c in Fe_3GeTe_2 [46]

6.1.1 Heterostructure growth

To investigate the interfacial effect of 2D magnetic heterostructures, we first need to to prepare the sapphire/Bi_2Te_3/Fe_3GeTe_2 samples by MBE system. During the preparation process, we also use RHEED and quartz to monitor the growth process in-situ.

(1) Substrate cleaning and annealing. This step is identical to the one described in Chapter 3. After the substrate has been annealed, the substrate temperature is returned to room temperature in preparation for the deposition of Bi_2Te_3.

(2) Preparation of Bi_2Te_3. The process for preparing Bi_2Te_3 is the same as described in Chapter 5. We use a two-step process to grow a Bi_2Te_3 film on the sapphire substrate with an appropriate thickness. After the growth is complete, the effusion cell shutters and the substrate shutter are closed.

(3) Preparation of Fe_3GeTe_2. The substrate temperature is adjusted to the temperature required for the preparation of Fe_3GeTe_2 (280℃), and the beam flux ratio of the Fe, Ge, Te

elements is ensured to be 3:1:10. Once all temperatures are stable, the substrate shutter is opened and growth begins. After the growth is complete, the substrate shutter and three b effusion cell shutters are closed in sequence, and the temperature is returned to room temperature. If necessary, the sample can be annealed at 280℃ for five minutes to obtain a better crystal quality.

(4) Once all temperatures are decreased to room temperature, the sample is transferred to the load lock chamber and removed from the chamber.

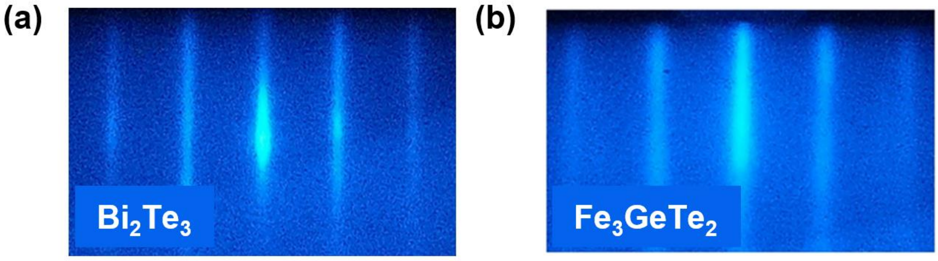

Figure 55. RHEED patterns of (a) 10 nm Bi_2Te_3; (b) 10 nm Fe_3GeTe_2

6.1.2 Preparation process optimization

In the preparation of Fe_3GeTe_2, the beam flux ratio of the Fe, Ge, Te elements is commonly set to 3:1:15. Due to the high volatility of Te, it is difficult to adsorb on the sapphire substrate. Therefore, it is often to ensure that Te is in an excess state when preparing Te-based compounds. It is worth noting that the preparation of Bi_2Te_3 in the last section was also carried out in a Te-rich environment. Therefore, whether to maintain the beam flux ratio of Fe, Ge, Te elements at 3:1:15 when preparing Fe_3GeTe_2 on Bi_2Te_3 is a content we need to study.

Here, we first prepared a high-quality 10 nm Bi_2Te_3 thin film, and then prepared a 10 nm Fe_3GeTe_2 thin film on the Bi_2Te_3 film using a 3:1:15 beam flux ratio. Its RHEED pattern is shown in Figure 56a. In addition to the stripe pattern, Figure 56a also contains a series of dot matrix patterns, indicating that in addition to the 2D Fe_3GeTe_2 phase, the sample also contains a 2D phase. This miscellaneous phase may be due to a 3D compound $FeTe_x$ formed by Fe reacting with excess Te. The appearance of $FeTe_x$ confirms that during the growth process of Fe_3GeTe_2, the beam flux of Te cannot be blindly increased, especially in an environment rich in Te, the rate of Te should be appropriately reduced. Therefore, we adjusted the beam flux ratio to 3:1:10, and prepared a 10 nm Fe_3GeTe_2 thin film on the 10 nm Bi_2Te_3 thin film again. As shown in Figure 56b, the Fe_3GeTe_2 deposited under this parameter only contains a single 2D phase, and the sharp stripe pattern also confirms its flat and high-quality surface morphology.

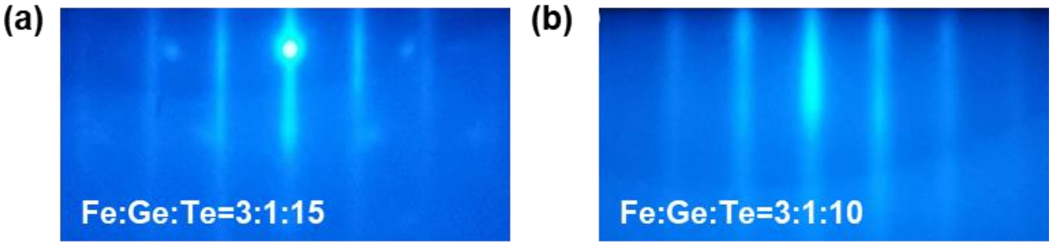

Figure 56. RHEED patterns for Fe_3GeTe_2 thin films under different flux ratios

6.1.3 Morphology and crystal structure characterization

In Section 6.1, we have already proven that the Fe_3GeTe_2/Bi_2Te_3 heterostructure has a flat 2D layer structure. Next, we will further characterize the crystal structure and surface morphology of the heterostructure through XRD, TEM, and AFM.

In Chapter 3, we briefly introduced the structure of Fe_3GeTe_2. Fe_3GeTe_2 belongs to the space group P63/mmc, and its basic unit is a Fe-Fe dumbbell structure wrapped by two layers of Te atoms, with a collinear pair of Fe-Ge atoms in the middle. Since both Fe_3GeTe_2 and Bi_2Te_3 belong to the hexagonal system, it is easy to grow Fe_3GeTe_2 along the 0001 direction on the Bi_2Te_3 thin film to prepare a 2D heterostructure. After the growth is completed, we use XRD to characterize the crystal structure of the heterostructure. Figure 57 shows the XRD spectra for Bi_2Te_3 thin film and the Fe_3GeTe_2/Bi_2Te_3 heterostructure. Before the Fe_3GeTe_2 was deposited, the sample's XRD showed peaks of $Bi_2Te_3\{003\}$ crystal planes; after the heterostructure was prepared, the sample showed peaks of both $Bi_2Te_3\{003\}$ and $Fe_3GeTe_2\{002\}$ crystal planes, proving that both layers of the heterostructure are high-quality single crystal thin films. It is worth noting that after Fe_3GeTe_2 deposition, the XRD signal originally belonging to Bi_2Te_3 decreased, which is due to the Fe_3GeTe_2 covering the surface and absorbing part of the XRD signal.

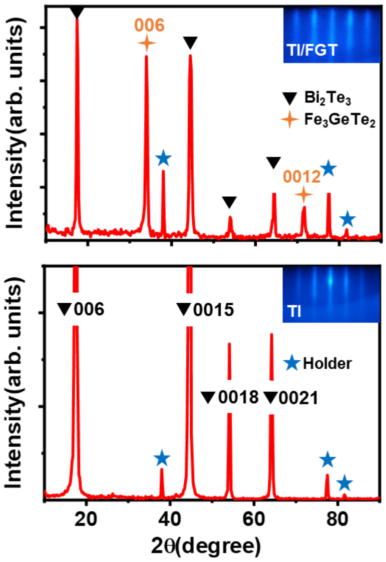

Figure 57. The XRD results for Fe_3GeTe_2/Bi_2Te_3 heterostructure and Bi_2Te_3 thin film

Further, we characterized the surface of the sample by AFM and used NanoScope Analysis software to analyze its surface morphology. Figure 58 shows the AFM results of pure Bi_2Te_3 thin films and Fe_3GeTe_2/Bi_2Te_3 heterostructures. Similar to past reports, Bi_2Te_3 shows a triangular step-like surface morphology, which is related to the layered structure of the TI material, and its surface roughness (R_q) is 0.56 nm. In contrast, Fe_3GeTe_2 has a smoother surface than TI. Therefore, after growing Fe_3GeTe_2, the roughness of the heterostructure becomes 0.3 nm, as shown in Figure 58b.

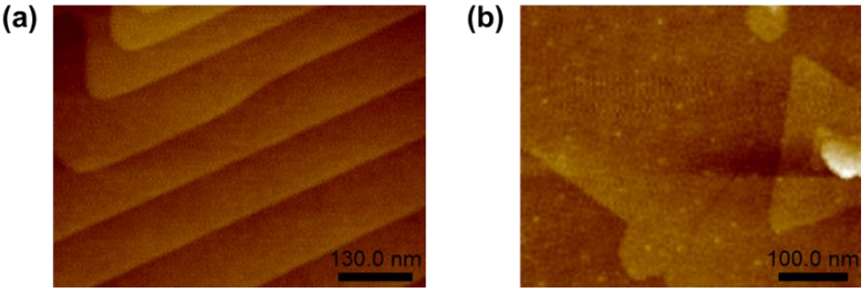

Figure 58. AFM scanning images of Bi_2Te_3 and Fe_3GeTe_2/Bi_2Te_3 heterostructures

TEM was used to measure the crystal structure of the heterostructure to clarify the quality at its interface. As shown in Figure 59a, in the low-resolution TEM results, three areas of different brightness can be observed, which correspond to Fe_3GeTe_2/Bi_2Te_3/sapphire from top to bottom. Figure 59b shows the magnified crystal structure of Fe_3GeTe_2 and Bi_2Te_3. In both materials, clear van der Waals gaps can be observed, and there are no obvious lattice defects and dislocations, proving that the heterostructure has maintained a layered growth mode during the growth process.

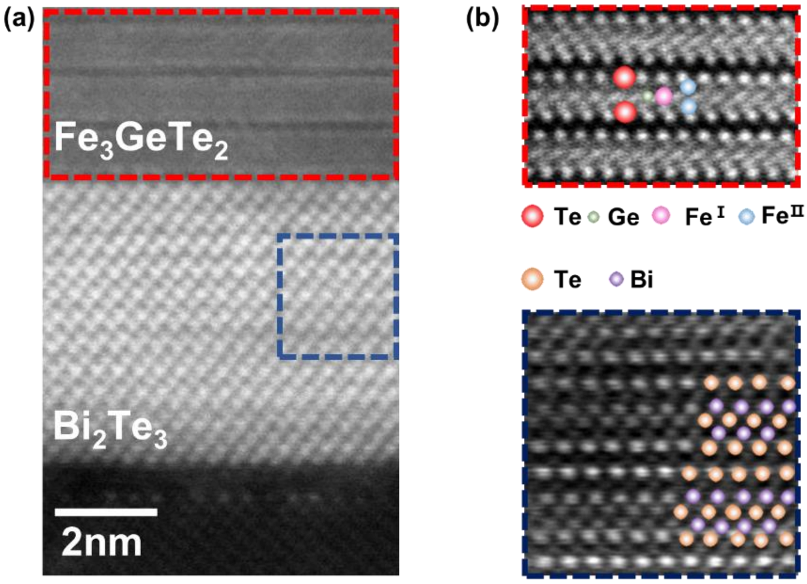

Figure 59. TEM scanning results of Fe_3GeTe_2/Bi_2Te_3 heterostructure

6.2 Interfacial magnetism manipulation in Fe_3GeTe_2/Bi_2Te_3

In our previous research work, we have fully characterized the magnetic properties of Fe_3GeTe_2 thin films and Fe_3GeTe_2/Bi_2Te_3 heterostructures[24]. By comparing the transport measurement results of 55 nm Fe_3GeTe_2 and Fe_3GeTe_2(8 nm)/Bi_2Te_3(10 nm) heterostructures, we proved that after integration with Bi_2Te_3, the T_c of Fe_3GeTe_2 was raised to above room temperature (380K), which is much higher than pure Fe_3GeTe_2 thin film (220K). Then, we prepared heterostructures with different thicknesses of Fe_3GeTe_2, including Fe_3GeTe_2(3 nm)/Bi_2Te_3(10 nm), Fe_3GeTe_2(4 nm)/Bi_2Te_3(10 nm), and Fe_3GeTe_2(8 nm)/ Bi_2Te_3(10 nm), to further study the relationship between the heterostructure magnetism and the structure. Figure 60a summarizes the T_c change with the different FGT thickness in the Fe_3GeTe_2(n)/Bi_2Te_3(10 nm) heterostructures (n=3,4,5,10 nm), which was extracted from the remnant anomalous Hall resistance Rxy(0)/Rxy(H_s). Obviously, when n=4 nm, the Fe_3GeTe_2 (n)/Bi_2Te_3 (10 nm) heterostructure exhibits the highest T_c, at n=3 nm and 5 nm, the T_c of the sample are relatively close, while the heterostructure has the lowest T_c at n=10 nm.

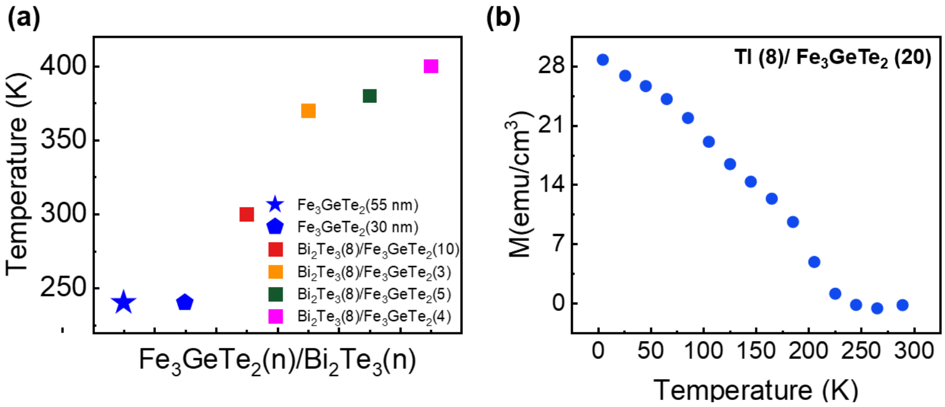

Figure 60. Dimensional effects in the Fe_3GeTe_2/Bi_2Te_3 heterostructure. (a) Thickness-dependent T_c of Fe_3GeTe_2/Bi2Te3 heterostructures and Fe_3GeTe_2 thin films; (b) M-T curve of the heterostructure with a 20-nm Fe_3GeTe_2 thickness of 20 nm [24]

Previous reports have shown that several external methods can increase the T_c of Fe_3GeTe_2. In Chapter 3, we proposed a method to enhance the ferromagnetism of FGT by magnetic doping. The mechanism of the T_c enhancement by doping is the increase of the spin-exchange interaction in the FGT structure. However, we did not deliberately adjust the magnetic doping in the Fe_3GeTe_2/Bi_2Te_3 heterostructure so this mechanism can be excluded. Recent theoretical calculations show that applying stress in 2D magnet can also control their ferromagnetism. For example, a tensile strain of 5% can increase the T_c of $CrGeTe_3$ from 57 K to above 100 K[90]. The mechanism of the T_c enhancement is that the tensile strain of the lattice enhances the spin-orbit coupling, thereby enhancing the ferromagnetism of the material[148,149]. However, considering that both Fe_3GeTe_2 and Bi_2Te_3 are van der Waals materials, the epitaxy process of the heterostructure can overcome a large lattice mismatch. And, there was no observation of lattice dislocations or obvious defects through in-situ monitoring by RHEED. Therefore, the potential impact of stress is also excluded.

Based on the above analysis, we believe that the interfacial coupling in the Fe_3GeTe_2/Bi_2Te_3 heterostructure is the cause of the enhancement in its magnetism. In Chapter 5, we mentioned that due to the non-trivial surface states and strong spin-orbit coupling in TI, the interfacial coupling in TI/FM heterostructure can introduce a magnetism in TI layer and even enhancing the original ferromagnetism of the heterostructure[72]. According to previous literature[24], we have clarified the interfacial interaction mechanism in the Fe_3GeTe_2/Bi_2Te_3 heterostructure through first-principles calculations: After forming a heterostructure with TI, the magnetic exchange interaction at the interface of the Fe_3GeTe_2/Bi_2Te_3 heterostructure is enhanced, which leads to a higher T_c.

After identifying the mechanism of interfacial magnetism manipulation in the Fe_3GeTe_2/Bi_2Te_3 heterostructure, the thickness dependency of the magnetism shown in Figure 60a can be explained by the competitive relationship between the interfacial effect and the intrinsic dimensionality effect of Fe_3GeTe_2. When the thickness of Fe_3GeTe_2 is 4 nm, the exchange interaction at the interface balances the dimensionality effect of Fe_3GeTe_2, leading to the highest T_c enhancement. When the thickness of Fe_3GeTe_2 is smaller ($\leqslant$4 nm), the contribution of interfacial exchange coupling on the T_c enhancement is less than the limiting effect of the dimensionality effect. When the thickness of Fe_3GeTe_2 is greater than 4 nm, because the exchange interaction only exists at the heterostructure interface, its enhancement effect will decrease as the Fe_3GeTe_2 thickness increases. Furthermore, continuing to increase the Fe_3GeTe_2 thickness again will promote the magnetic property of the heterostructure gradually approach pure Fe_3GeTe_2, which is manifested as a decrease in T_c. To verify this conclusion, we further prepared a Fe_3GeTe_2 (20 nm)/Bi_2Te_3 (8 nm) heterostructure and measured the temperature-dependent magnetic curve using SQUID (Figure 60b). The result indicates that the T_c of this sample is about ~230 K, which is similar to bulk Fe_3GeTe_2, proving that the magnetic properties of the Fe_3GeTe_2 (20 nm)/Bi_2Te_3 (8 nm) heterostructure are now close to those of a pure Fe_3GeTe_2 thin film.

6.3 Terahertz emission in Fe_3GeTe_2/Bi_2Te_3 heterostructure

After obtaining a high-quality 2D heterostructure with room temperature magnetism, our next goal is to study its spin transport properties to lay a foundation for the preparation of 2D spintronic devices in the future. In the last chapter, we introduce the spin THz, which considered a key technology for studying 2D interfacial spin properties due to its lossless, ultra-fast, and interface-sensitive characteristics. In the last chapter, we mentioned the formula for the generation of spin terahertz due to the spin charge conversion (SCC) effect:

$$\vec{E}_{\mathrm{THz}} \propto \vec{j}_c \propto \theta_{\mathrm{SHE}} \cdot \vec{j}_s \times \overrightarrow{M} / \left|\overrightarrow{M}\right| \tag{6.1}$$

After femtosecond laser excitation, the magnitude of the THz signal emitted by the Fe_3GeTe_2/Bi_2Te_3 heterostructure depends on its net magnetization and the spin Hall angle. According to the previous discussion, these two parameters are closely related to the interfacial effects of the heterostructure (for example, spin-orbit coupling effect and spin exchange effect). Therefore, by measuring the spin terahertz emission of the Fe_3GeTe_2/Bi_2Te_3 heterostructure, we can further explore its magnetic properties and interfacial effects.

6.3.1 Spin THz generation in the heterostructure

Figure 61 shows the terahertz emission schematic of the Fe_3GeTe_2/Bi_2Te_3 heterostructure. By placing the sample under an in-plane magnetic field of 80 mT and using a femtosecond laser to excite the heterojunction material, a spin THz signal can be detected.

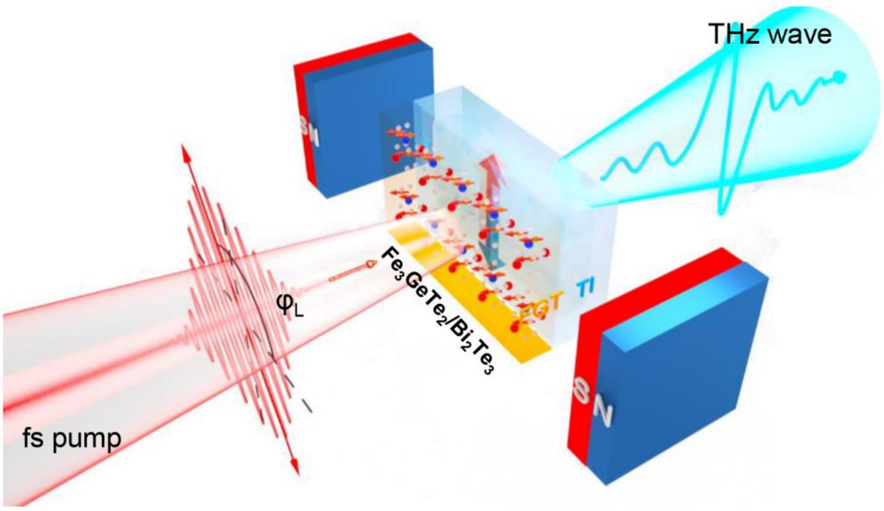

Figure 61. The schematic diagram of the THz emission model of the Fe_3GeTe_2/Bi_2Te_3 heterostructure

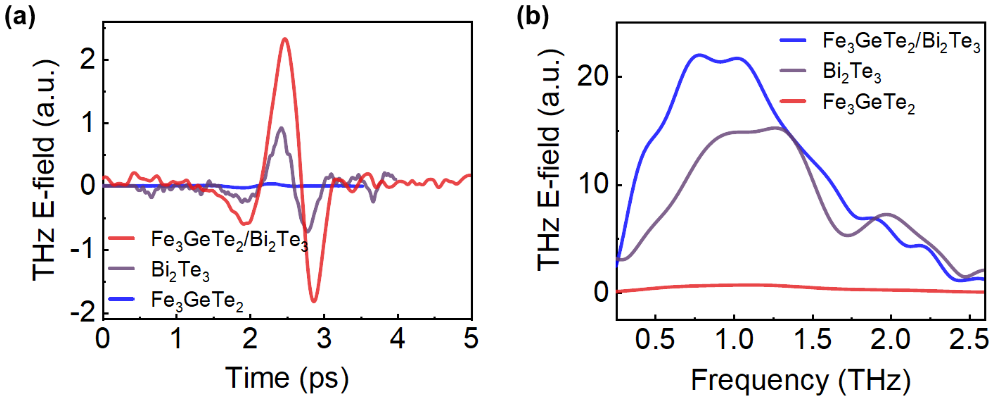

Figure 62. THz emission for Fe_3GeTe_2(4 nm)/Bi_2Te_3(8 nm) heterostructure, 4 nm Fe_3GeTe and 8 nm Bi_2Te_3 (a) Time domain signals (b) Frequency domain signals.

As shown in Figure 62a, while keeping the laser pump flux at 12 μJ/cm^2, we detected the THz time domain signals of the Fe_3GeTe_2 (4 nm)/Bi_2Te_3 (8 nm) heterostructure, 4 nm Fe_3GeTe_2, and 8 nm Bi_2Te_3 respectively, and obtained their frequency domain signals through fast Fourier transform, as shown in Figure 62b. It is worth noting that the THz signal magnitude of the heterostructure is far exceeds the signal of the thin film samples. In previous studies, it has been proven that most magnetic materials can produce ultrafast demagnetization phenomena under the excitation of femtosecond lasers, thereby emitting THz radiation[150-152]. However, the THz radiation signal generated by this method is small. In addition, due to the weak magnetization of Fe_3GeTe_2 itself, the contribution of ultrafast demagnetization to the THz emission of the heterostructure can be ruled out. Moreover, in Figure 62b, the peak frequencies of the heterostructure and Bi_2Te_3 thin film signals are ~0.8 THz and ~1.2 THz, respectively, indicating that the THz emission mechanism in the heterostructure is different from that of pure Bi_2Te_3 thin films.

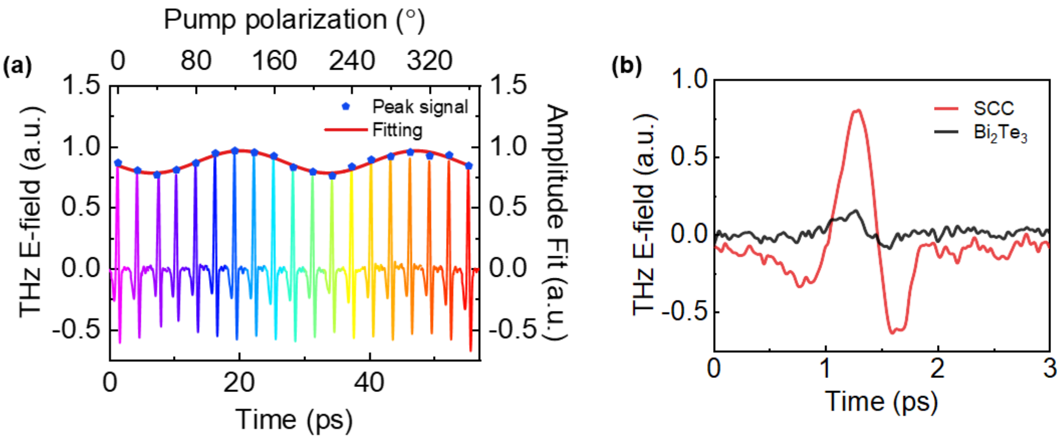

Figure 63. THz results of the Fe_3GeTe_2(4 nm)/Bi_2Te_3(8 nm) heterostructure (a) Polarization-dependent THz signal; (b) THz components belonging to SCC and Bi_2Te_3 photoelectric effect.

Previous research has shown that under the pump of femtosecond lasers, pure Bi_2Te_3 thin films can generate THz radiation due to the photoelectric effect (CPGE or LPGE). However, the THz radiation generated by the photoelectric effect depends on the polarization direction of the pump light [158]. When we fix the azimuth angle of the sample and the direction of the magnetic field and only control the polarization plane of the femtosecond laser, we find that the THz signal emitted by the heterostructure only undergoes a small periodic oscillation (as shown in Figure 63a which indirectly confirms that the THz radiation generated by the photoelectric effect in Bi_2Te_3 only has a very small contribution on the heterostructure signal, and its magnitude can be ignored. Further, we extracted the components of the THz signal that varied and did not change with the polarization state of the incident light and plotted their signals in Figure 63b. According to the above discussion, the two types of THz components come from the SCC effect on the interface and the photoelectric effect inside Bi_2Te_3. Obviously, the intensity of the former is much greater than that of the latter. Therefore, the THz signal emitted by the Fe_3GeTe_2/Bi_2Te_3 heterostructure is considered to only come from the SCC effect on the interface.

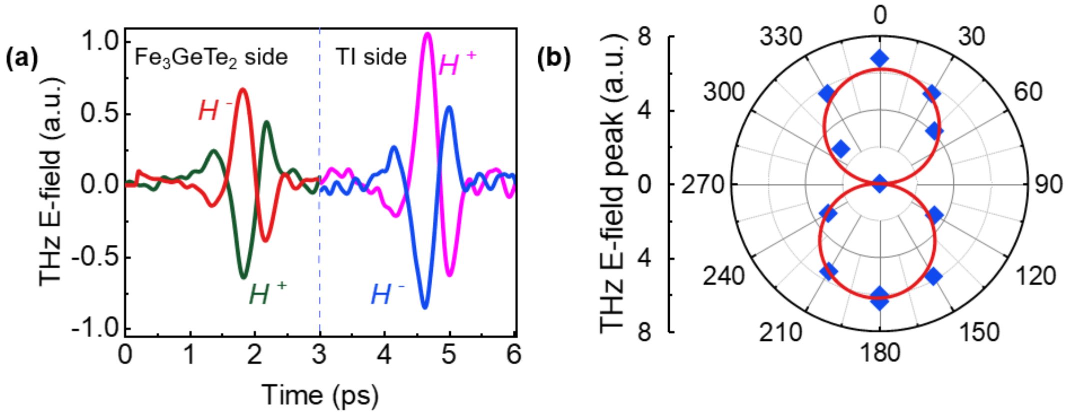

Figure 64. THz emission manipulation in Fe_3GeTe_2/Bi_2Te_3 heterostructure (a) incidence plane and external magnetic field dependent signals; (b) external field direction dependent signals

To further confirm this conclusion, we systematically studied the dependence of the heterostructure THz emission on the light incidence angle and the magnetization direction, as shown in Figure 64a. Clearly, flipping the sample (i.e., changing the incidence plane) or changing the direction of the magnetic field will cause a flip in the polarity of signal, which is in line with the prediction of Eq. (6.1), and can also eliminate the possibility that THz is caused by ultrafast demagnetization. Previous studies have demonstrated that the THz signal induced by ultrafast demagnetization is only related to the sample's azimuthal angle and irrelevant to the incidence direction. Figure 64b shows the change of the THz signal with the magnetic field. By rotating the direction of the magnetic field, the intensity of the signal follows a quadratic rotational symmetry relationship with the angle. With the removal of the external magnetic field, the heterostructure can still achieve THz emission, and its emission intensity shows hysteresis behavior as the magnetic field changes[17]. Moreover, we found that the intensity of the THz from the heterostructure is linearly related to the power of the pump light (Figure 65). All these phenomena are in line with the description of Eq. (6.1), which directly proves that the THz signal emitted from the Fe_3GeTe_2/Bi_2Te_3 heterostructure originates from the Spin-Charge Conversion (SCC) effect at the interface.

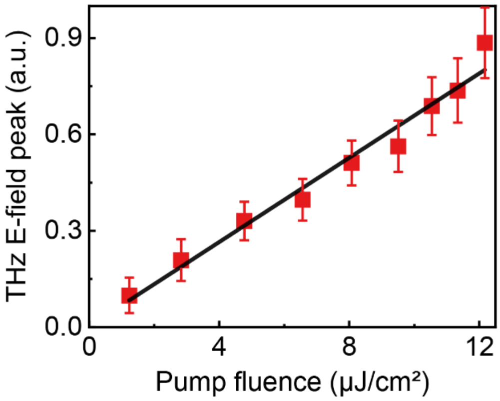

Figure 65. THz intensity of the heterostructure with the change in the power of the pump light.

6.3.2 Characterization of the interfacial effects by THz method

To study the interfacial exchange interaction in the Fe_3GeTe_2/Bi_2Te_3 heterostructure, we prepared heterostructures with different Fe_3GeTe_2 thickness, and then characterized the contribution of the interface on the magnetism through THz method. Figure 66a shows the transient THz signal of the Fe_3GeTe_2 (n nm)/Bi_2Te_3 (8 nm) heterostructure, and Figure 66b summarizes the peak-to-peak value of the THz signal for all samples. The peak value initially increases and then decreases with increasing Fe_3GeTe_2 thickness. Figure 67 compares the T_c of the Fe_3GeTe_2 (n nm)/Bi_2Te_3 (8 nm) heterostructure (measured by VSM) with the THz peak intensity as a function of Fe_3GeTe_2 thickness, two curves show the same with the thickness, which confirms that the change in the intensity of the THz originates from the magnetism change of the heterostructure. Its fundamental reason is the interfacial magnetism enhancement of the heterostructure. Therefore, when the Fe_3GeTe_2 thickness is 4 nm, the THz signal from the heterostructure reaches its maximum value.

Because of the competitive relationship between the interfacial effect and intrinsic dimensionality effects of in the heterostructure, when the thickness of Fe_3GeTe_2 is small, its T_c is greatly limited by dimensionality effects, which directly manifests as a decrease in the net magnetization intensity of the heterostructure, resulting in a decrease in the intensity of the THz signal. At the same time, according to Eq. (7.1), thinner samples will reduce the spin current J_s injected to the interface, which will also result in a lower THz emission efficiency. When the Fe_3GeTe_2 thickness is greater than 4 nm, because the exchange interaction only exists at the heterostructure interface, further increasing the Fe_3GeTe_2 thickness will make the magnetic properties of the heterostructure gradually approach pure Fe_3GeTe_2, the result of which is also the decline of the THz emission efficiency. When the Fe_3GeTe_2 thickness is 4 nm, the contribution of the exchange interaction on the interface reaches its maximum, leading to the highest T_c, as well as the highest and the THz emission efficiency.

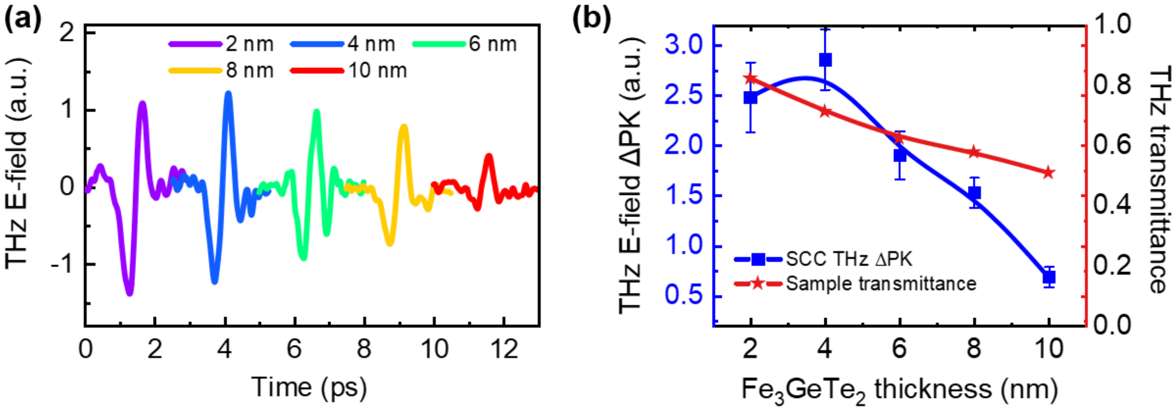

Figure 66. THz emission as a function of the FGT thickness. (a) Radiated THz temporal waveforms for various FGT thickness with a fixed TI thickness of 8 nm. (b) Extracted SCC effect induced THz peak-to-peak signals and the corresponding THz transmittance ratio.

To exclude the terahertz signal absorption effect caused by increased thickness, Figure 66b also measures the absorption ratio of different heterostructures for the THz radiation, which monotonically increases with the increase in thickness. This verifies that the change in THz intensity observed in Figure 66a is not due to the sample's absorption of the emitted signal.

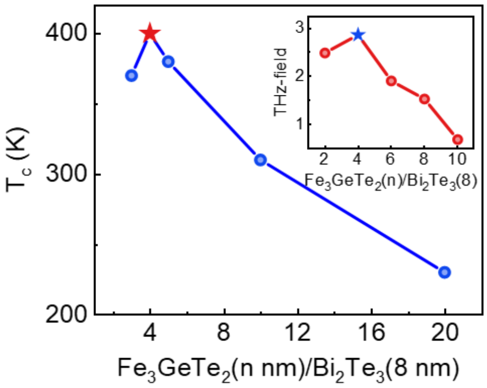

Figure 67. FGT thickness-dependent T_c and THz magnitude for Fe_3GeTe_2 (n nm)/Bi_2Te_3 (8 nm) heterostructures.

6.3.3 Characterization of the interfacial SCC effect by THz

According to Eq. (5.8), the intensity of the THz signal emitted by the heterostructure is proportional to the Spin-Charge Conversion (SCC) ability of the heterostructure, i.e., the value of the Spin Hall angle θ_{SHE}. A previous research has proven that the SCC effect in a TI-based heterostructure may stem from the inverse Edelstein effect (IEE) on the TI interface or the inverse spin Hall effect (ISHE) in the TI bulk[146]. To explore the source of SCC in the Fe_3GeTe_2/Bi_2Te_3 heterostructure, we prepared a series of Fe_3GeTe_2 (4 nm)/Bi_2Te_3 (n nm) heterostructures and systematically studied the THz emission efficiency with the TI thickness.

Figure 68a shows the THz signals emitted by the heterostructure when the thickness of Bi_2Te_3 is 4, 6, 8, 10, 12, and 15 nm. For the 4 nm sample, the intensity of the THz signal is relatively small; as the thickness of Bi_2Te_3 further increases the THz intensity also increases; however, when the thickness of Bi_2Te_3 exceeds 6 nm, the emitted THz begins to gradually decrease. Figure 68b summarizes the peak-to-peak value of the signals for all samples, and same TI thickness dependency been reported in TI/FM heterostructure[146]. This non-monotonic relationship proves that the SCC effect in the interface o does not come from ISHE but from the IEE effect on the TI surface. Due to the strong spin-orbit coupling, TI material has a topologically nontrivial surface with a momentum-locked spin channel, where any injected spin/charge current will be efficiently converted into charge/spin current. In 2D scales (Bi_2Te_3 thickness less than 6 nm), due to the hybridization effect of the upper and lower surfaces, the surface state of Bi_2Te_3 will open a bandgap, thereby destroying its spin-momentum-locked transport channel and reducing its SCC efficiency[153]. Compared with IEE, ISHE has a lower spin-charge conversion efficiency. Therefore, as the thickness of Bi_2Te_3 increases, the contribution from the bulk state to the SCC increases accordingly, resulting in a decrease in THz emission efficiency. In addition, as the sample thickness increase, the absorption of the THz from the sample is another factor leading to the decline in emission efficiency, as shown in Figure 68b.

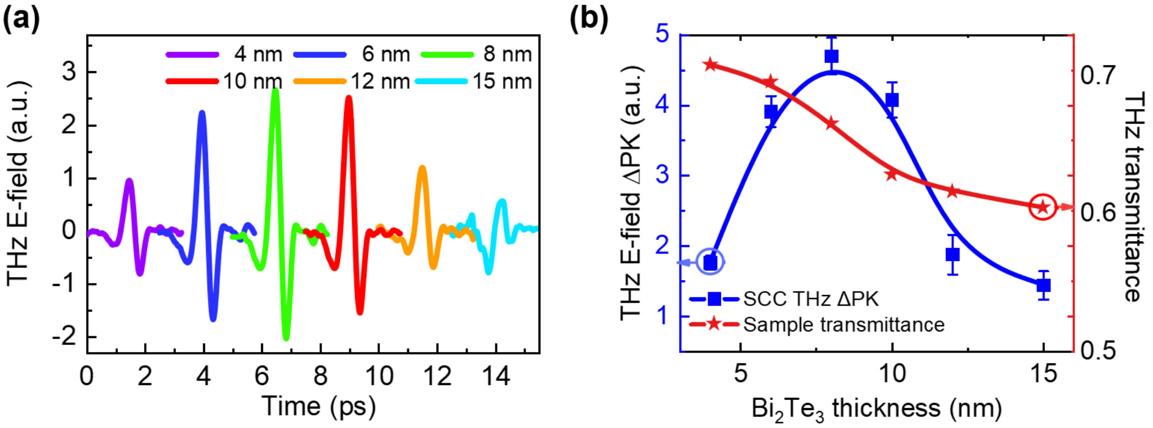

Figure 68. Effect of TI thickness on THz emission. (a) Recorded THz transients from FGT(4 nm)|TI heterostructures with different TI thicknesses of 4, 6, 8, 10, 12, and 15 nm. (b) THz peak-to-peak signal as a function of the TI thickness, and the corresponding linear THz transmittance ratio.

6.4 Interfacial magnetism manipulation in Fe_4GeTe_2/Bi_2Te_3

Until now, we have confirmed the enhancement effect of the interface on the T_c of Fe_3GeTe_2 by electrical and optical methods. A series of thickness-dependent experiments have also proven that the magnetic properties of a 2D heterostructure are subject to the combined effects of the intrinsic dimensionality effect and the interfacial exchange coupling. Since the T_c of Fe_3GeTe_2 is relatively low, and the magnetic anisotropy can only be along the perpendicular direction, it has a smaller application value. In contrast, Fe_4GeTe_2 has a higher T_c and its magnetic anisotropy can be tunned through doping, which has more potential for the manufacture of 2D spintronic devices. Therefore, in this section, we will prepare Fe_4GeTe_2/Bi_2Te_3 heterostructures and discuss the interfacial magnetism manipulation in the heterostructure.

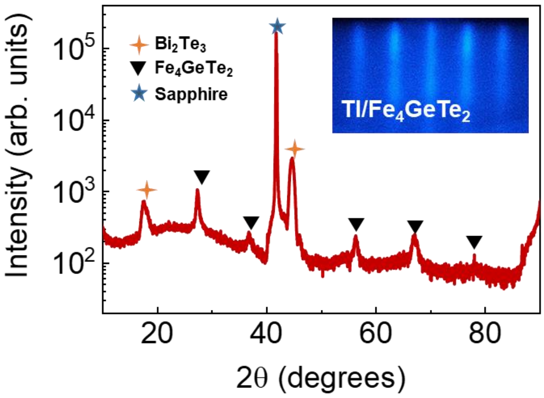

Figure 69. XRD results of Fe_4GeTe_2 (4 nm)/Bi_2Te_3 (8 nm) heterostructure

Firstly, we also use MBE to prepare the required Fe_4GeTe_2/Bi_2Te_3. Referencing our research results in Section 6.3, we chose to use 8 nm Bi_2Te_3 and 4 nm Fe_4GeTe_2 to form a heterostructure for the strongest interfacial effect. Similar to the growth method of Fe_3GeTe_2/Bi_2Te_3 in Section 6.1, after the preparation of Bi_2Te_3, we adjust the Fe, Ge, and Te flux ratio to 4:1:15, and continue to grow a 4 nm Fe_4GeTe_2 film. During the growth process, we also use RHEED for in-situ monitoring (as shown in the insert of Figure 69). After the sample is prepared, we use XRD to characterize the crystal structure of the heterostructure. Figure 69 shows the XRD spectrum of the Fe_4GeTe_2 (4 nm)/Bi_2Te_3 (8 nm) heterostructure. The sample simultaneously exhibits peaks of the Bi_2Te_3\{003\} and Fe_4GeTe_2\{003\} crystal planes, confirming that both layers of heterostructure are high-quality single-crystal films.

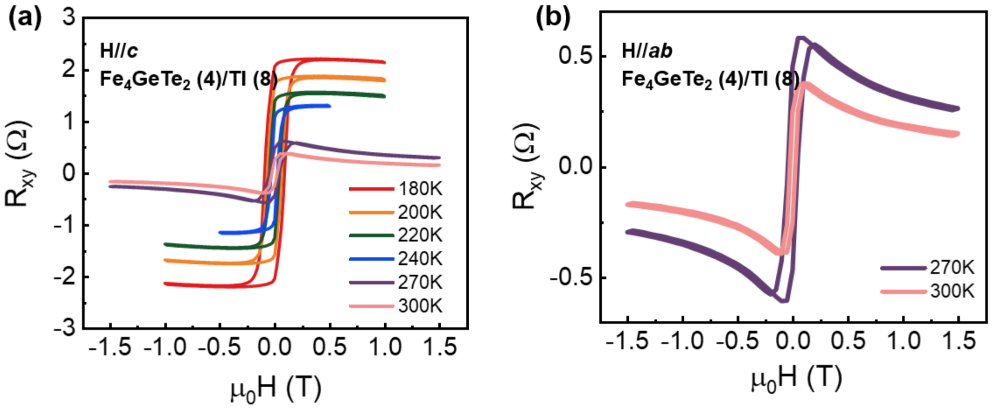

Figure 70. Hall curves of Fe_4GeTe_2(4 nm)/Bi_2Te_3(8 nm) heterostructure under (a) out-of-plane and (b) in-plane magnetic fields

Previous results have shown that the intrinsic T_c of Fe_4GeTe_2 is 220 K, and its magnetic anisotropy is vertical at low temperatures and in-plane at high temperatures, which has been confirmed in Chapter 3. After obtaining high-quality Fe_4GeTe_2/Bi_2Te_3 heterostructures, we also use electrical and magnetic methods to characterize the magnetic properties of the heterostructures. By comparing the Fe_4GeTe_2/Bi_2Te_3 results with pure Fe_4GeTe_2, the contribution of the interface on the magnetism can be identified. Figure 70a shows the temperature dependent Hall curve of the heterostructure under a vertical magnetic field. Apparently, after integrating with Bi_2Te_3, the T_c of the Fe_4GeTe_2/Bi_2Te_3 heterostructure is risen to above room temperature, confirming that the T_c enhancement by Bi_2Te_3 interface is also applicable to Fe_4GeTe_2. It is worth noting that, unlike the intrinsic Fe_4GeTe_2, the Fe_4GeTe_2/Bi_2Te_3 heterostructure displays square hysteresis loops in the temperature range of 180 K-300 K, demonstrating that it has vertical magnetic anisotropy.

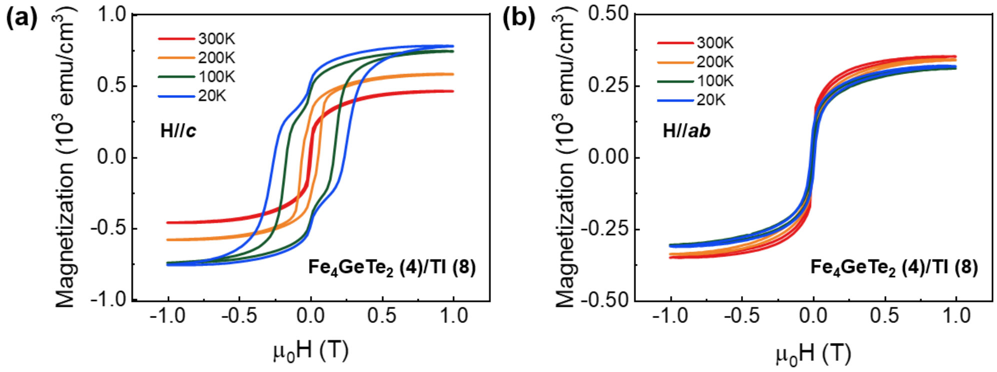

Figure 71. Hysteresis loop of Fe_4GeTe_2(4 nm)/Bi_2Te_3(8 nm) heterostructure under out-of-plane and in-plane magnetic fields

To confirm this result, we measured the Hall curve of the heterostructure under an in-plane magnetic field, as shown in Figure 70b. At 270 K and 300 K, the heterostructure displays steep in-plane Hall curves, indicating that the sample maintains stable vertical magnetic anisotropy even at high temperatures. This result ion dictates that the interface of Fe_4GeTe_2/Bi_2Te_3 not only regulates the T_c of the heterostructure but can also change the magnetic anisotropy of the adjacent 2D magnet. To verify the results of electrical testing, we also use a Superconducting Quantum Interference Device (SQUID) to directly measure the magnetic properties of the Fe_4GeTe_2 (4 nm)/Bi_2Te_3 (8 nm) heterostructure. Figure 71 shows the hysteresis loop of the heterostructure under perpendicular and in-plane magnetic fields, clearly indicating that the sample maintains a stable vertical magnetic anisotropy in the temperature range of 20 K-300 K. Figure 72 shows the change in the sample's remanent magnetization with temperature. When the temperature reaches above 330 K, the remanent magnetization falls to zero, indicating that the T_c of the Fe_4GeTe_2 film indeed rises to above room temperature after integration with Bi_2Te_3. These results are basically consistent with the electrical measurements results, confirming the manipulation of interfacial exchange on the T_c and magnetic anisotropy of 2D magnets.

Unfortunately, due to time constraints, this thesis has not delved into the mechanism of the interfacial manipulation in Fe_4GeTe_2/Bi_2Te_3 heterostructures. Preparing Fe_4GeTe_2/Bi_2Te_3 samples of different thicknesses, studying the interface dependence of the T_c, and clarifying the manipulation mechanism of this interfacial effect will be an important objective for the next stage of this thesis.

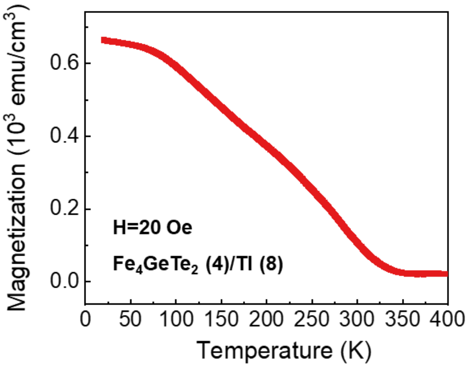

Figure 72. Temperature-dependent remanent magnetization of the Fe_4GeTe_2(4 nm)/Bi_2Te_3(8 nm) heterostructure

6.5 Chapter summary

In this chapter, we combined the 2D topological insulator Bi_2Te_3 with FGT to form a 2D magnetic/topological heterostructure, and studied the magnetism manipulation effect by the interface. We first chose Fe_3GeTe_2 as the magnetic layer and used electrical method to reveal the T_c enhancement induced by the interface. Based on this result, we optimized the structure of Fe_3GeTe_2/Bi_2Te_3, and a series of thickness-dependent experiments confirmed that both dimensionality effect and interfacial exchange coupling can tune the magnetic properties of the heterostructure. Subsequently, we used THz method to study the magnetic properties of the

Fe_3GeTe_2/Bi_2Te_3 heterostructure, confirming the magnetism enhancement induced by the interface again and elucidating the spin-charge conversion process on the interface by THz-TDS system. Finally, we prepared a series of Fe_4GeTe_2/Bi_2Te_3 heterostructures and proved that the interfacial magnetism manipulation in the magnetic/topological interface is effective for all 2D FGT materials. And its function is not only increasing the T_c, but can also significantly changing the magnetic anisotropy of FGT layer. This result demonstrates the huge potential of 2D topological/ferromagnetic heterostructures in the construction of spintronic devices.

Chapter 7. Conclusion and Outlook

In 1958, Jack Kilby created the world's first IC on a germanium substrate. Thanks to the development of semiconductor fabrication processes, the density of IC has rapidly increased over the next sixty-plus years, going from one transistor per chip to 100 billion transistors per chip, which almost adheres to the prediction of Moore's Law. However, as key node enter the 1 nm stage, traditional 3D materials cannot maintain their original physical properties at sub-nanometer scales, failing to meet the needs of IC manufacturing processes. Also, the gradually reducing linewidth introduces uncontrollable power consumption issues. As the channel size decreases, the static power consumption caused by leakage current in IC devices gradually increases. Under the constraints of size and power limits, the development of Moore's circuits is gradually approaching a bottleneck. Therefore, researching new materials and devices to break through the "size wall" and "power wall" has become a key direction to lead the technical revolution in the IC field.

2D materials are layered materials interconnected by van der Waals forces, and they possess rich electrical, magnetic, mechanical, and optical properties. Unlike traditional 3D materials, 2D materials can still maintain their physical properties at atomic thickness, meeting the needs of sub-nanometer IC manufacturing processes. Therefore, 2D materials have been receiving much attention as a fundamental electronic material to extend Moore's Law. Spintronics is a novel discipline that studies electron spin. Unlike traditional CMOS device that manipulates the movement of charges, spintronic device achieves information read/write by controlling electron spin flips, featuring low power consumption, radiation resistance, and non-volatile data. 2D spintronic devices based on two-dimensional magnetic materials can take advantage of the high integration of 2D materials and the ultra-low power consumption of spintronic materials, potentially breaking through the "power wall" and "size wall" currently constraining the development of IC, and further extending Moore's Law.

However, due to the dimensional effects of 2D materials, their 2D ferromagnetic order is hard to maintain at high temperatures, which cannot meet the industrial working temperature requirements for magnetic materials. The existing methods to enhance 2D magnetism through external stimuli (such as carrier manipulation, laser, strain, etc.) lack the necessary conditions for industrialization, such as large-area, controllability, and high efficiency. In addition, previous research on 2D magnets often used mechanically exfoliated samples, which is not conducive to wafer-scale preparation or subsequent material processing. Importantly, mechanically exfoliated samples discard the "interface property" of 2D materials, which is considered a crucial factor in achieving efficient magnetism manipulation. Compared to traditional methods, the magnetism manipulation on epitaxial 2D magnets through interfacial effects has advantages such as large area, simple structure, and high efficiency. Also, this method is compatible with modern semiconductor industrial patterning processes. Further, by epitaxially combining 2D magnets with other functional 2D materials (such as topological insulators) into 2D heterostructures, it is possible to control the spin properties of heterostructures by introducing the 2D interface. The study of ferromagnetic heterostructures with 2D interface effects will lay the foundation for future low-power, high-integration efficient spintronic devices.

7.1 Work summary

This paper investigates the manipulation of magnetism by interfacial effects in epitaxially prepared 2D systems, including 2D magnets, 2D topological insulators (TI), and 2D magnetic/topological heterostructures. Firstly, targeting the pain points of traditional 2D magnets, such as low T_c and difficulties in large-scale preparation, this paper successfully explores the epitaxial preparation process of 2D magnet FGT (including Fe_4GeTe_2 and Fe_3GeTe_2) with a high T_c. By magnetic doping, we successfully achieved the preparation of 2D magnet with room temperature T_c and adjustable magnetic anisotropy. Further, combined with theoretical calculations, we successfully revealed the magnetism manipulation of the Fe_4GeTe_2/Al_2O_3 interface and confirmed this theoretical model through experiments. After structurally optimization, the T_c of Fe_4GeTe_2 can reach above 500 K. In addition to the intrinsic 2D magnets, we also studied the 2D ferromagnetic order introduced by interface effects.

Integrating TI with ferromagnetic material, a long-range magnetic order can be introduced on the surface of TI layer through the magnetic proximity effect at the interface, with a T_c greater than common magnetic TI introduced through doping. At the same time, through transport measurements, we found that the introduced ferromagnetism breaks the time-reversal symmetry of the TI layer, opening a gap in the surface state, which is fundamental to realizing spintronic quantum devices based on TI materials. Further, we combined TI with 2D magnet FGT into 2D heterostructures, hoping to use the interfacial effect to achieve 2D devices with high T_c, strong magnetic anisotropy, and high spin control efficiency. Combined with electrical and optical methods, we proved that the FGT/Bi_2Te_3 heterostructure has stable perpendicular magnetic anisotropy at room temperature and can achieve efficient spin-charge conversion. The specific research contents are as follows:

1. We explored the method for preparing large-area, high-quality 2D magnet Fe_4GeTe_2 using molecular beam epitaxy equipment. Furthermore, through a series of temperature-dependent magnetic characterization results, we proved that the temperature dependence of Fe_4GeTe_2 magnetic anisotropy originates from the competition between magnetocrystalline anisotropy and shape anisotropy. After obtaining high-quality Fe_4GeTe_2, we successfully established a Heisenberg model based on RKKY exchange interaction to describe its magnetism. Based on this model, we proposed that the T_c of Fe_4GeTe_2 could be controlled by magnetic doping. By precisely controlling the Fe beam flow in Fe_4GeTe_2 during growth, we discovered three magnetic 2D phases of Fe_4GeTe_2: Fe_4GeTe_2, $Fe_{4+x}GeTe_2$, and $Fe_{4-x}GeTe_2$. Through electrical and magnetic measurements, we found that the magnetic properties of Fe_4GeTe_2 (such as T_c and magnetic anisotropy) vary with Fe doping concentration. The experimental results are consistent with theoretical predictions, laying a foundation for us to achieve 2D magnetism with high T_c and adjustable anisotropy.
2. When studying the magnetic properties of epitaxially prepared Fe_4GeTe_2, we unexpectedly found that the T_c of our thin film sample was much higher than the values reported in the past, while the T_c of the bulk sample was close to past values. A series of thickness-dependent experiments confirmed that this abnormal magnetism enhancement comes from

the Fe_4GeTe_2/Al_2O_3 interface. When the thickness of Fe_4GeTe_2 is thin, the interface's contribution is significant, leading to a larger increase in the T_c. Through first-principles calculations, we simulated the electronic structure of the Fe_4GeTe_2/Al_2O_3 interface and found that the migration of Fe localized states introduced by orbital coupling from the interface is the reason for the T_c enhancement. Further, we unveiled the localized state shift as a function of interface through thickness-dependent photoelectron spectroscopy, confirming the existence of this interface effect.

3. In addition to studying the contribution of interfacial effects on magnetism enhancement, we also studied the magnetism introduction by the interfacial effect. Using topological insulator Bi_2Se_3 and ferromagnetic semiconductor MnGe, we successfully realized the magnetic proximity effect on the heterostructure and introduced a long-range ferromagnetic order in Bi_2Se_3. The transport characteristics transition from WAL to WL confirms this conclusion. Unlike traditional ferromagnetic topological phases achieved through doping, this proximity-induced ferromagnetic order has a higher T_c. Further electrical measurement results show that a band gap of about 80 meV was opened on the surface state of the TI layer. This finding not only facilitates the study of the generation and manipulation of 2D magnetism but also lays the foundation for achieving high-temperature quantum spintronic devices.
4. Based on the above research results, we combined Bi_2Te_3 with FGT to form 2D magnetic heterostructure and studied the interfacial magnetism manipulation effect. To intuitively display the enhancing effect of the interface on the magnetism, we first selected Fe_3GeTe_2 as the magnetic layer and confirmed the enhancing effect of the interface on the T_c through electrical and magnetic characterization methods. Further, a series of thickness-dependent experiments proved that the T_c of the heterostructure is subject to the combined effect of the intrinsic dimensionality effect of the 2D magnet and the interfacial exchange coupling, and the two are in a competitive relationship. Finally, we used terahertz method to study the magnetic properties of the Fe_3GeTe_2/Bi_2Te_3 heterostructure. While confirming the enhancing effect of the interfacial effect on 2D magnetism, we also elucidated the spin-

charge conversion process on the 2D magnetic interface through terahertz time-domain spectra. This result demonstrates the great potential of 2D topological/ferromagnetic heterostructures in constructing superconducting power-consuming two-dimensional spintronic devices. Lastly, we studied the magnetic properties of the Fe_4GeTe_2/Bi_2Te_3 heterostructure and revealed the manipulation of magnetism and magnetic anisotropy by interfacial effects.

7.2 Outlook

Although this thesis has made significant progress in the preparation of high-quality 2D magnets and heterostructure, the construction of 2D magnetic interface models, and the elucidation of the mechanisms of interface manipulation of 2D magnetism, due to time constraints and other objective conditions, there are still many areas that need further improvement. We believe that further research on the following issues can lead to greater progress in the field of 2D magnetic materials:

1. Although this thesis systematically studies the changes in electronic structure and T_c caused by the interfacial effects of Fe_4GeTe_2, it is still necessary to further verify whether this conclusion is applicable to all 2D magnets. In past research, there are numerous reports involved in 2D magnets preparation by MBE. However, similar interfacial manipulation effects have rarely been reported. In future work, we plan to choose different substrate materials, hoping to verify the fundamental mechanism of the interfacial effect through the study of different substrate interfaces, to achieve more effective control of 2D magnetism.
2. In Chapter 6, we prepared Fe_3GeTe_2/Bi_2Te_3 heterostructure and characterized their magnetic properties through electrical and optical method, confirming the interfacial enhancement effect on the magnetism of Fe_3GeTe_2. However, according to the results of Chapter 5, interfacial effects not only contribute to the magnetic layer, but also introduce a 2D magnetism into the TI layer. Unfortunately, since Fe_3GeTe_2 is metallic, it is difficult to separate the magnetoresistance characteristics of the two layers of the heterostructure, and hence to study its magnetic proximity effect. Therefore, exploring new 2D magnetic

insulators, preparing them into heterostructure with topological insulator, and studying the magnetic proximity effect in the interface, is an important part of our future research.

3. In this thesis, the Fe_3GeTe_2/Bi_2Te_3 heterostructure we prepared showed efficient THz emission characteristics. Compared with other 2D systems, its high emission efficiency comes from two aspects: one is the high T_c brought by interface effects, and the other is the large spin Hall angle characteristic of the topological surface states. This inspires us to use the 2D magnetic/topological heterostructure to achieve high charge-spin conversion efficiency. By fabricating the heterostructure into an SOT device, it is expected to achieve spintronic memory or spintronic sensor devices based on a 2D system.

Chapter 8. Résumé étendu

En 1958, Jack Kilby a créé le premier circuit intégré au monde sur substrat de germanium. Grâce au développement des procédés de fabrication de semi-conducteurs, la densité des circuits intégrés a rapidement augmenté au cours des soixante années suivantes, passant d'un transistor par puce à 100 milliards de transistors par puce, ce qui correspond presque à la prédiction de la loi de Moore. Cependant, alors que le nœud clé entre dans la phase 1 nm, les matériaux 3D traditionnels ne peuvent pas conserver leurs propriétés physiques d'origine à des échelles inférieures au nanomètre, ne parvenant pas à répondre aux besoins des processus de fabrication de circuits intégrés. En outre, la réduction progressive de la largeur de ligne introduit des problèmes de consommation d'énergie incontrôlables. À mesure que la taille du canal diminue, la consommation d'énergie statique provoquée par le courant de fuite dans les dispositifs IC augmente progressivement. Sous les contraintes de taille et de puissance, le développement des circuits de Moore se rapproche progressivement d'un goulot d'étranglement. Par conséquent, la recherche de nouveaux matériaux et dispositifs pour briser le « mur de taille » et le « mur de puissance » est devenue une direction clé pour mener la révolution technique dans le domaine des circuits intégrés.

Les matériaux 2D sont des matériaux en couches interconnectés par les forces de Van der Waals et possèdent de riches propriétés électriques, magnétiques, mécaniques et optiques. Contrairement aux matériaux 3D traditionnels, les matériaux 2D peuvent toujours conserver leurs propriétés physiques à une épaisseur atomique, répondant ainsi aux besoins des processus de fabrication de circuits intégrés inférieurs au nanomètre. Par conséquent, les matériaux 2D ont reçu beaucoup d'attention en tant que matériaux électroniques fondamentaux pour étendre la loi de Moore. La spintronique est une nouvelle discipline qui étudie le spin des électrons. Contrairement au dispositif CMOS traditionnel qui manipule le mouvement des charges, le dispositif spintronique permet la lecture/écriture des informations en contrôlant les retournements de spin des électrons, avec une faible consommation d'énergie, une résistance aux radiations et des données non volatiles. Les dispositifs spintroniques 2D basés sur des matériaux magnétiques bidimensionnels peuvent tirer parti de la forte intégration des matériaux 2D et de la consommation d'énergie ultra-faible des matériaux spintroniques, brisant ainsi potentiellement le « mur de puissance » et le « mur de taille » qui limitent actuellement le développement des circuits intégrés, et étendant encore la loi de Moore.

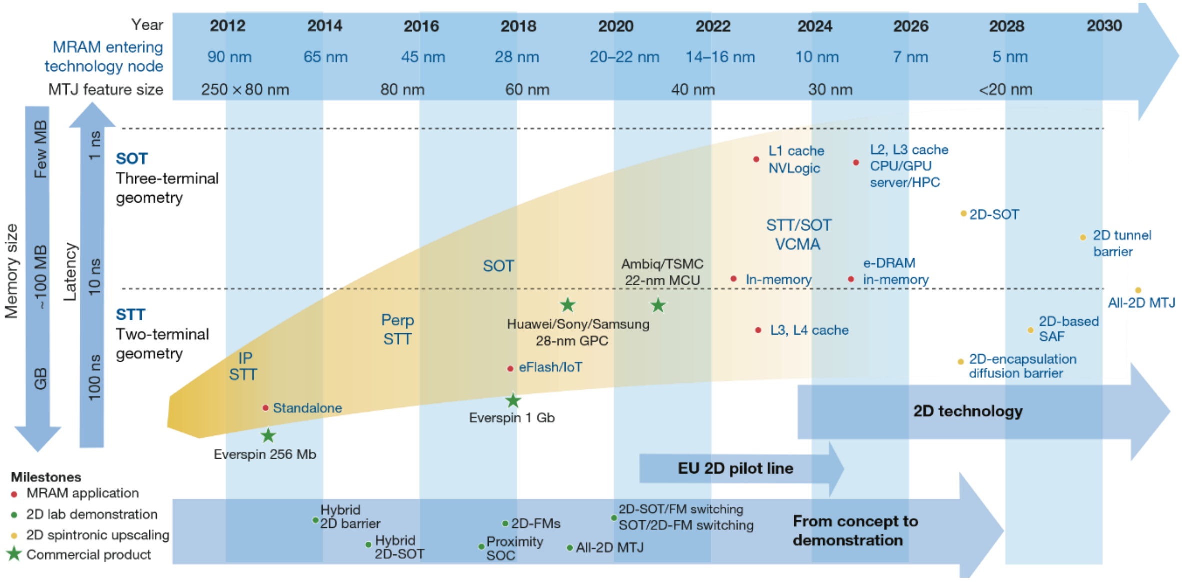

Figure 73. Le potentiel des aimants 2D pour la mémoire spintronique

Cependant, en raison des effets dimensionnels des matériaux 2D, leur ordre ferromagnétique 2D est difficile à maintenir à des températures élevées, ce qui ne peut pas répondre aux exigences de température de fonctionnement industrielle des matériaux magnétiques. Les méthodes existantes pour améliorer le magnétisme 2D grâce à des stimuli externes (tels que la manipulation du porteur, le laser, la déformation, etc.) ne disposent pas des conditions nécessaires à l'industrialisation, telles qu'une grande surface, une contrôlabilité et une efficacité élevée. De plus, les recherches antérieures sur les aimants 2D utilisaient souvent des échantillons exfoliés mécaniquement, ce qui n’est pas propice à la préparation à l’échelle d’une tranche ou au traitement ultérieur des matériaux. Il est important de noter que les échantillons exfoliés mécaniquement éliminent la « propriété d’interface » des matériaux 2D, considérée comme un facteur crucial pour parvenir à une manipulation efficace du magnétisme. Par rapport aux méthodes traditionnelles, la manipulation du magnétisme sur des aimants épitaxiaux 2D via des effets d'interface présente des avantages tels qu'une grande surface, une structure simple et un rendement élevé. En outre, cette méthode est compatible avec les processus industriels modernes de modélisation des semi-conducteurs. De plus, en combinant par épitaxie des aimants 2D avec d'autres matériaux 2D fonctionnels (tels que des isolants topologiques) dans des hétérostructures 2D, il est possible de contrôler les propriétés de spin des hétérostructures en introduisant l'interface 2D. L'étude des hétérostructures ferromagnétiques avec effets d'interface 2D jettera les bases de futurs dispositifs spintroniques à faible consommation et à haute intégration.

8.1 Résumé des travaux

Cet article étudie la manipulation du magnétisme par effets interfaciaux dans des systèmes 2D préparés par épitaxie, notamment des aimants 2D, des isolants topologiques (TI) 2D et des hétérostructures magnétiques/topologiques 2D. Premièrement, en ciblant les problèmes des aimants 2D traditionnels, tels que la faible Tc et les difficultés de préparation à grande échelle, cet article explore avec succès le processus de préparation épitaxiale de l'aimant 2D FGT (y compris Fe_4GeTe_2 et Fe_3GeTe_2) avec une Tc élevée. Par dopage magnétique, nous avons réussi à préparer un aimant 2D avec une Tc à température ambiante et une anisotropie magnétique réglable. De plus, en combinaison avec des calculs théoriques, nous avons révélé avec succès la manipulation du magnétisme de l'interface Fe_4GeTe_2/Al_2O_3 et confirmé ce modèle théorique par des expériences. Après optimisation structurelle, la T_c de Fe_4GeTe_2 peut atteindre plus de 500 K. En plus des aimants 2D intrinsèques, nous avons également étudié l'ordre ferromagnétique 2D introduit par les effets d'interface. En intégrant le TI à un matériau ferromagnétique, un ordre magnétique à longue portée peut être introduit à la surface de la couche de TI grâce à l'effet de proximité magnétique à l'interface, avec une T_c supérieure au TI magnétique commun introduit par dopage. Dans le même temps, grâce à des mesures de transport, nous avons constaté que le ferromagnétisme introduit rompait la symétrie d'inversion temporelle de la couche TI, ouvrant ainsi une brèche dans l'état de surface, ce qui est fondamental pour réaliser des dispositifs quantiques spintroniques basés sur des matériaux TI. De plus, nous avons combiné TI avec un aimant 2D FGT dans des hétérostructures 2D, dans l'espoir d'utiliser l'effet d'interface pour obtenir des dispositifs 2D avec une T_c élevée, une forte anisotropie magnétique et une efficacité de contrôle de spin contrôle. En combinaison avec des méthodes électriques et optiques, nous avons prouvé que l'hétérostructure FGT/Bi_2Te_3 présente une anisotropie magnétique perpendiculaire stable à température ambiante et peut réaliser une conversion efficace de charge de spin. Les contenus spécifiques de la recherche sont les suivants:

1. Nous avons exploré la méthode de préparation d'un aimant 2D Fe_4GeTe_2 de grande surface et de haute qualité à l'aide d'un équipement d'épitaxie par jets moléculaires. Grâce à une série de résultats de caractérisation magnétique dépendant de la température, nous avons prouvé que la dépendance à la température de l'anisotropie magnétique de Fe_4GeTe_2 provient de la compétition entre l'anisotropie magnétocristalline et l'anisotropie de forme. Après avoir obtenu du Fe_4GeTe_2 de haute qualité, nous avons réussi à établir un modèle de Heisenberg basé sur l'interaction d'échange RKKY pour décrire son magnétisme. Sur la base de ce modèle, nous avons proposé que la T_c de Fe_4GeTe_2 puisse être contrôlée par dopage magnétique. En contrôlant précisément le flux du faisceau de Fe dans Fe_4GeTe_2 pendant la croissance, nous avons découvert trois phases magnétiques 2D de Fe_4GeTe_2: Fe_4GeTe_2, $Fe_{4+x}GeTe_2$, et $Fe_{4-x}GeTe_2$. Grâce à des mesures électriques et magnétiques, nous avons constaté que les propriétés magnétiques de Fe_4GeTe_2 (telles que Tc et l'anisotropie magnétique) varient en fonction de la concentration de dopage en Fe. Les résultats expérimentaux sont cohérents avec les prédictions théoriques, jetant les bases pour atteindre un magnétisme 2D avec une T_c élevée.
2. Lors de l'étude des propriétés magnétiques du Fe_4GeTe_2 préparé par épitaxie, nous avons découvert de manière inattendue que la T_c de notre échantillon de film mince était beaucoup plus élevée que les valeurs rapportées dans le passé, tandis que la T_c de l'échantillon global était proche des valeurs passées. Une série d'expériences dépendantes de l'épaisseur ont confirmé que cette augmentation anormale du magnétisme provient de l'interface Fe_4GeTe_2/Al_2O_3. Lorsque l'épaisseur de Fe_4GeTe_2 est fine, la contribution de l'interface est significative, conduisant à une augmentation plus importante du T_c. Grâce à des calculs de principes premiers, nous avons simulé la structure électronique de l'interface Fe_4GeTe_2/Al_2O_3 et avons découvert que la migration des états localisés de Fe introduite

par le couplage orbital depuis l'interface est à l'origine de l'amélioration de T_c. De plus, nous avons dévoilé le changement d'état localisé en fonction de l'interface grâce à la spectroscopie photoélectronique dépendante de l'épaisseur, confirmant l'existence de cet effet d'interface.

3. En plus d'étudier la contribution des effets interfaciaux sur l'amélioration du magnétisme, nous avons également étudié l'introduction du magnétisme par l'effet interfacial. En utilisant l'isolant topologique Bi_2Se_3 et le semi-conducteur ferromagnétique MnGe, nous avons réussi à réaliser l'effet de proximité magnétique sur l'hétérostructure et à introduire un ordre ferromagnétique à longue portée dans Bi_2Se_3 La transition des caractéristiques de transport de WAL à WL confirme cette conclusion. Contrairement aux phases topologiques ferromagnétiques traditionnelles obtenues par dopage, cet ordre ferromagnétique induit par la proximité a une T_c plus élevée. D'autres résultats de mesures électriques montrent qu'une bande interdite d'environ 80 meV a été ouverte sur l'état de surface de la couche de TI. Cette découverte facilite non seulement l’étude de la génération et de la manipulation du magnétisme 2D, mais jette également les bases de la réalisation de dispositifs spintroniques quantiques à haute température.
4. Sur la base des résultats de recherche ci-dessus, nous avons combiné Bi_2Se_3 avec FGT pour former une hétérostructure magnétique 2D et étudié l'effet de manipulation du magnétisme interfacial. Pour afficher intuitivement l'effet d'amélioration de l'interface sur le magnétisme, nous avons d'abord sélectionné Fe_3GeTe_2 comme couche magnétique et confirmé l'effet d'amélioration de l'interface sur le T_c grâce à des méthodes de caractérisation électrique et magnétique. En outre, une série d'expériences dépendantes de l'épaisseur ont prouvé que la Tc de l'hétérostructure est soumise à l'effet combiné de l'effet de dimensionnalité intrinsèque de l'aimant 2D et du couplage d'échange interfacial, et que les deux sont dans une relation de compétition. Enfin, nous avons utilisé la méthode térahertz pour étudier les propriétés magnétiques de l'hétérostructure Fe_3GeTe_2/Bi_2Te_3. Tout en confirmant l'effet d'amélioration de l'effet interfacial sur le magnétisme 2D, nous avons également élucidé le processus de conversion spin-charge sur l'interface magnétique

2D à travers des spectres térahertz dans le domaine temporel. Ce résultat démontre le grand potentiel des hétérostructures topologiques/ferromagnétiques 2D dans la construction de dispositifs spintroniques bidimensionnels supraconducteurs et consommateurs d'énergie. Enfin, nous avons étudié les propriétés magnétiques de l'hétérostructure Fe_4GeTe_2/Bi_2Te_3 et révélé la manipulation du magnétisme et de l'anisotropie magnétique par effets interfaciaux.

8.2 Résumé étendu

Bien que cette thèse ait fait des progrès significatifs dans la préparation d'aimants et d'hétérostructures 2D de haute qualité, la construction de modèles d'interface magnétique 2D et l'élucidation des mécanismes de manipulation d'interface du magnétisme 2D, en raison de contraintes de temps et d'autres conditions objectives, de nombreux domaines nécessitent encore des améliorations. Nous pensons que des recherches plus approfondies sur les questions suivantes peuvent conduire à de plus grands progrès dans le domaine des matériaux magnétiques 2D.

1. Bien que cette thèse étudie systématiquement les changements de structure électronique et de T_c provoqués par les effets interfaciaux de Fe_4GeTe_2, il est encore nécessaire de vérifier davantage si cette conclusion est applicable à tous les aimants 2D. Dans des recherches antérieures, il existe de nombreux rapports sur la préparation d'aimants 2D par MBE. Cependant, des effets similaires de manipulation interfaciale ont rarement été rapportés. Dans les travaux futurs, nous prévoyons de choisir différents matériaux de substrat, dans l'espoir de vérifier le mécanisme fondamental de l'effet interfacial grâce à l'étude de différentes interfaces de substrat, afin d'obtenir un contrôle plus efficace du magnétisme 2D.
2. Au chapitre 6, nous avons préparé l'hétérostructure Fe_3GeTe_2/Bi_2Te_3 et caractérisé leurs propriétés magnétiques par des méthodes électriques et optiques, confirmant l'effet d'amélioration interfaciale sur le magnétisme de Fe_3GeTe_2. Cependant, selon les résultats du chapitre 5, les effets interfaciaux contribuent non seulement à la couche magnétique,

mais introduisent également un magnétisme 2D dans la couche TI. Malheureusement, Fe_3GeTe_2 étant métallique, il est difficile de séparer les caractéristiques de magnétorésistance des deux couches de l'hétérostructure, et donc d'étudier son effet de proximité magnétique. Par conséquent, explorer de nouveaux isolants magnétiques 2D, les préparer en hétérostructure avec un isolant topologique et étudier l'effet de proximité magnétique dans l'interface constitue une partie importante de nos recherches futures.

3. Dans cette thèse, l'hétérostructure Fe_3GeTe_2/Bi_2Te_3 que nous avons préparée a montré des caractéristiques d'émission THz efficaces. Par rapport à d'autres systèmes 2D, son efficacité d'émission élevée provient de deux aspects : l'un est la T_c élevée apportée par les effets d'interface, et l'autre est le grand angle de Hall de spin caractéristique des états de surface topologiques. Cela nous incite à utiliser l'hétérostructure magnétique/topologique 2D pour obtenir une efficacité de conversion charge-spin élevée. En fabriquant l'hétérostructure dans un dispositif SOT, il est prévu de réaliser des dispositifs de mémoire spintronique ou de capteurs spintroniques basés sur un système 2D.

REFERENCES

[1] Theis T. N., Wong H. S. P. The End of Moore's Law: A New Beginning for Information Technology[J]. Computing in Science & Engineering, 2017, 19(2): 41-50.

[2] Žutić I., Fabian J., Das Sarma S. Spintronics: Fundamentals and applications[J]. Reviews of Modern Physics, 2004, 76(2): 323-410.

[3] Song T., Cai X., Tu M. W.-Y., et al. Giant tunneling magnetoresistance in spin-filter van der Waals heterostructures[J]. Science, 2018, 360(6394): 1214-1218.

[4] Jiang S., Li L., Wang Z., et al. Spin tunnel field-effect transistors based on two-dimensional van der Waals heterostructures[J]. Nature Electronics, 2019, 2(4): 159-163.

[5] Huang B., Clark G., Klein D. R., et al. Electrical control of 2D magnetism in bilayer CrI3[J]. Nature Nanotechnology, 2018, 13(7): 544-548.

[6] Jiang S., Li L., Wang Z., et al. Controlling magnetism in 2D CrI3 by electrostatic doping[J]. Nature Nanotechnology, 2018, 13(7): 549-553.

[7] Thiel L., Wang Z., Tschudin M. A., et al. Probing magnetism in 2D materials at the nanoscale with single-spin microscopy[J]. Science, 2019, 364(6444): 973-976.

[8] Hu X., Zhao Y., Shen X., et al. Enhanced Ferromagnetism and Tunable Magnetism in Fe_3GeTe_2 Monolayer by Strain Engineering[J]. ACS Applied Materials & Interfaces, 2020, 12(23): 26367-26373.

[9] Liu B., Liu S., Yang L., et al. Light-Tunable Ferromagnetism in Atomically Thin Fe_3GeTe_2 Driven by Femtosecond Laser Pulse[J]. Physical Review Letters, 2020, 125(26): 267205.

[10] Burch K. S., Mandrus D., Park J.-G. Magnetism in two-dimensional van der Waals materials[J]. Nature, 2018, 563(7729): 47-52.

[11] Liu S., Yang K., Liu W., et al. Two-dimensional ferromagnetic superlattices[J]. National Science Review, 2020, 7(4): 745-754.

[12] Liu S., Yuan X., Zou Y., et al. Wafer-scale two-dimensional ferromagnetic Fe_3GeTe_2 thin films grown by molecular beam epitaxy[J]. npj 2D Materials and Applications, 2017, 1(1): 30.

[13] Zhang W., Zhang L., Wong P. K. J., et al. Magnetic Transition in Monolayer VSe2 via Interface Hybridization[J]. ACS Nano, 2019, 13(8): 8997-9004.

[14] Zhang L., Huang X., Dai H., et al. Proximity-Coupling-Induced Significant Enhancement of Coercive Field and Curie Temperature in 2D van der Waals Heterostructures[J]. Advanced Materials, 2020, 32(38): 2002032.

[15] Bernevig B. A. Topological Insulators and Topological Superconductors[M]. Princeton University Press, 2013.

[16] Leijnse M., Flensberg K. Introduction to topological superconductivity and Majorana fermions[J]. Semiconductor Science and Technology, 2012, 27(12): 124003.

[17] Chen X., Wang H., Liu H., et al. Generation and Control of Terahertz Spin Currents in Topology-Induced 2D Ferromagnetic Fe3GeTe2|Bi2Te3 Heterostructures[J]. Advanced Materials, 2022, 34(9): 2106172.

[18] Voerman J. A., Li C., Huang Y., et al. Spin-Momentum Locking in the Gate Tunable Topological Insulator $BiSbTeSe_2$ in Non-Local Transport Measurements[J]. Advanced Electronic Materials, 2019, 5(12): 1900334.

[19] Li C. H., Van 'T Erve O. M. J., Yan C., et al. Electrical detection of current generated spin in topological insulator surface states: Role of interface resistance[J]. Scientific Reports, 2019, 9(1): 6906.

[20] Zhang D., Shi M., Zhu T., et al. Topological Axion States in the Magnetic Insulator $MnBi_2Te_4$ with the Quantized Magnetoelectric Effect[J]. Physical Review Letters, 2019, 122(20): 206401.

[21] Zang J., Nagaosa N. Monopole current and unconventional Hall response on a topological insulator[J]. Physical Review B, 2010, 81(24): 245125.

[22] Kou X., He L., Lang M., et al. Manipulating Surface-Related Ferromagnetism in Modulation-Doped Topological Insulators[J]. Nano Letters, 2013, 13(10): 4587-4593.

[23] Mogi M., Tsukazaki A., Kaneko Y., et al. Ferromagnetic insulator Cr2Ge2Te6 thin films with perpendicular remanence[J]. APL Materials, 2018, 6(9): 091104.

[24] Wang H., Liu Y., Wu P., et al. Above Room-Temperature Ferromagnetism in Wafer-Scale Two-Dimensional van der Waals Fe_3GeTe_2 Tailored by a Topological Insulator[J]. ACS Nano, 2020, 14(8): 10045-10053.

[25] Schuhl A., Lacour D. Spin dependent transport: GMR & TMR[J]. Comptes Rendus Physique, 2005, 6(9): 945-955.

[26] Binasch G., Grünberg P., Saurenbach F., et al. Enhanced magnetoresistance in layered magnetic structures with antiferromagnetic interlayer exchange[J]. Physical Review B, 1989, 39(7): 4828-4830.

[27] Baibich M. N., Broto J. M., Fert A., et al. Giant Magnetoresistance of (001)Fe/(001)Cr Magnetic Superlattices[J]. Physical Review Letters, 1988, 61(21): 2472-2475.

[28] Heim D. E., Fontana R. E., Tsang C., et al. Design and operation of spin valve sensors[J]. IEEE Transactions on Magnetics, 1994, 30(2): 316-321.

[29] Parkin S. S. P., Kaiser C., Panchula A., et al. Giant tunnelling magnetoresistance at room temperature with MgO (100) tunnel barriers[J]. Nature Materials, 2004, 3(12): 862-867.

[30] Yuasa S., Nagahama T., Fukushima A., et al. Giant room-temperature magnetoresistance in single-crystal Fe/MgO/Fe magnetic tunnel junctions[J]. Nature Materials, 2004, 3(12): 868-871.

[31] Tehrani S., Slaughter J. M., Chen E., et al. Progress and outlook for MRAM technology[J]. IEEE Transactions on Magnetics, 1999, 35(5): 2814-2819.

[32] Yang H., Valenzuela S. O., Chshiev M., et al. Two-dimensional materials prospects for non-volatile spintronic memories[J]. Nature, 2022, 606(7915): 663-673.

[33] Allwood D. A., Xiong G., Faulkner C. C., et al. Magnetic Domain-Wall Logic[J]. Science, 2005, 309(5741): 1688-1692.

[34] Behin-Aein B., Datta D., Salahuddin S., et al. Proposal for an all-spin logic device with built-in memory[J]. Nature Nanotechnology, 2010, 5(4): 266-270.

[35] Manipatruni S., Nikonov D. E., Young I. A. Beyond CMOS computing with spin and polarization[J]. Nature Physics, 2018, 14(4): 338-343.

[36] Habermeier H. U. Scaling problems and quantum limits in integrated circuit miniaturization[J]. AIP Conference Proceedings, 1984, 122(1): 192-197.

[37] Novoselov K. S., Geim A. K., Morozov S. V., et al. Two-dimensional gas of massless Dirac fermions in graphene[J]. Nature, 2005, 438(7065): 197-200.

[38] Geim A. K., Novoselov K. S.: The rise of graphene, Nanoscience and Technology, : Co-Published with Macmillan Publishers Ltd, UK, 2009: 11-19.

[39] Tan C., Cao X., Wu X.-J., et al. Recent Advances in Ultrathin Two-Dimensional Nanomaterials[J]. Chemical Reviews, 2017, 117(9): 6225-6331.

[40] Mermin N. D., Wagner H. Absence of Ferromagnetism or Antiferromagnetism in One- or Two-Dimensional Isotropic Heisenberg Models[J]. Physical Review Letters, 1966, 17(22): 1133-1136.

[41] Gong C., Li L., Li Z., et al. Discovery of intrinsic ferromagnetism in two-dimensional van der Waals crystals[J]. Nature, 2017, 546(7657): 265-269.

[42] Klein D. R., Macneill D., Lado J. L., et al. Probing magnetism in 2D van der Waals crystalline insulators via electron tunneling[J]. Science, 2018, 360(6394): 1218-1222.

[43] Deiseroth H.-J., Aleksandrov K., Reiner C., et al. Fe_3GeTe_2 and Ni_3GeTe_2 – Two New Layered Transition-Metal Compounds: Crystal Structures, HRTEM Investigations, and Magnetic and Electrical Properties[J]. European Journal of Inorganic Chemistry, 2006, 2006(8): 1561-1567.

[44] Chen B., Yang J., Wang H., et al. Magnetic Properties of Layered Itinerant Electron Ferromagnet Fe_3GeTe_2[J]. Journal of the Physical Society of Japan, 2013, 82(12): 124711.

[45] Yuan D., Jin S., Liu N., et al. Tuning magnetic properties in quasi-two-dimensional ferromagnetic $Fe_{3-y}Ge_{1-x}As_xTe_2$ ($0 \leqslant x \leqslant 0.85$)[J]. Materials Research Express, 2017, 4(3): 036103.

[46] Deng Y., Yu Y., Song Y., et al. Gate-tunable room-temperature ferromagnetism in two-dimensional Fe_3GeTe_2[J]. Nature, 2018, 563(7729): 94-99.

[47] Li B., Wan Z., Wang C., et al. Van der Waals epitaxial growth of air-stable CrSe2 nanosheets with thickness-tunable magnetic order[J]. Nature Materials, 2021, 20(6): 818-825.

[48] Cui F., Zhao X., Xu J., et al. Controlled Growth and Thickness-Dependent Conduction-Type Transition of 2D Ferrimagnetic Cr2S3 Semiconductors[J]. Advanced Materials, 2020, 32(4): 1905896.

[49] Huang B., Clark G., Navarro-Moratalla E., et al. Layer-dependent ferromagnetism in a van der Waals crystal down to the monolayer limit[J]. Nature, 2017, 546(7657): 270-273.

[50] Zhang Z., Shang J., Jiang C., et al. Direct Photoluminescence Probing of Ferromagnetism in Monolayer Two-Dimensional $CrBr_3$[J]. Nano Letters, 2019, 19(5): 3138-3142.

[51] Mcguire M. A., Clark G., Kc S., et al. Magnetic behavior and spin-lattice coupling in cleavable van der Waals layered $CrCl_3$[J]. Physical Review Materials, 2017, 1(1): 014001.

[52] Wang X., Du K., Fredrik Liu Y. Y., et al. Raman spectroscopy of atomically thin two-dimensional magnetic iron phosphorus trisulfide ($FePS_3$) crystals[J]. 2D Materials, 2016, 3(3): 031009.

[53] Chaisson M. J. P., Sanders A. D., Zhao X., et al. Multi-platform discovery of haplotype-resolved structural variation in human genomes[J]. Nature Communications, 2019, 10(1): 1784.

[54] Lyu B., Gao Y., Zhang Y., et al. Probing the Ferromagnetism and Spin Wave Gap in VI3 by Helicity-Resolved Raman Spectroscopy[J]. Nano Letters, 2020, 20(8): 6024-6031.

[55] Stahl J., Shlaen E., Johrendt D. The van der Waals Ferromagnets $Fe_{5-\delta}GeTe_2$ and $Fe_{5-\delta-x}Ni_xGeTe_2$ – Crystal Structure, Stacking Faults, and Magnetic Properties[J]. Zeitschrift für anorganische und allgemeine Chemie, 2018, 644(24): 1923-1929.

[56] May A. F., Bridges C. A., Mcguire M. A. Physical properties and thermal stability of $Fe_{5-x}GeTe_2$ single crystals[J]. Physical Review Materials, 2019, 3(10): 104401.

[57] May A. F., Ovchinnikov D., Zheng Q., et al. Ferromagnetism Near Room Temperature in the Cleavable van der Waals Crystal Fe_5GeTe_2[J]. ACS Nano, 2019, 13(4): 4436-4442.

[58] Zhang X., Lu Q., Liu W., et al. Room-temperature intrinsic ferromagnetism in epitaxial CrTe2 ultrathin films[J]. Nature Communications, 2021, 12(1): 2492.

[59] Liu Z.-L., Wu X., Shao Y., et al. Epitaxially grown monolayer VSe2: an air-stable magnetic two-dimensional material with low work function at edges[J]. Science Bulletin, 2018, 63(7): 419-425.

[60] Zhang Y., Chu J., Yin L., et al. Ultrathin Magnetic 2D Single-Crystal CrSe[J]. Advanced Materials, 2019, 31(19): 1900056.

[61] Deng Y., Yu Y., Shi Meng Z., et al. Quantum anomalous Hall effect in intrinsic magnetic topological insulator MnBi2Te4[J]. Science, 2020, 367(6480): 895-900.

[62] Cao H. B., Banerjee A., Yan J. Q., et al. Low-temperature crystal and magnetic structure of $RuCl_3$[J]. Physical Review B, 2016, 93(13): 134423.

[63] He L., Kou X., Wang K. L. Review of 3D topological insulator thin-film growth by molecular beam epitaxy and potential applications[J]. Physica Status Solidi - Rapid Research Letters, 2013, 7(1-2): 50-63.

[64] Xia Y., Qian D., Hsieh D., et al. Observation of a large-gap topological-insulator class with a single Dirac cone on the surface[J]. Nature Physics, 2009, 5(6): 398-402.

[65] Chang C.-Z., Zhang J., Feng X., et al. Experimental Observation of the Quantum Anomalous Hall Effect in a Magnetic Topological Insulator[J]. Science, 2013, 340(6129): 167-170.

[66] Zhang L., Zhao D., Zang Y., et al. Ferromagnetism in vanadium-doped Bi_2Se_3 topological insulator films[J]. APL Materials, 2017, 5(7): 076106.

[67] Zhang M., Lü L., Wei Z.-T., et al. Ferromagnetism on a paramagnetic host background in cobalt-doped Bi_2Se_3 topological insulator[J]. Chinese Physics B, 2014, 23(7): 076104.

[68] Liu W., West D., He L., et al. Atomic-Scale Magnetism of Cr-Doped Bi_2Se_3 Thin Film Topological Insulators[J]. ACS Nano, 2015, 9(10): 10237-10243.

[69] Zhang D., Richardella A., Rench D. W., et al. Interplay between ferromagnetism, surface

states, and quantum corrections in a magnetically doped topological insulator[J]. Physical Review B, 2012, 86(20): 205127.

[70] Liu N., Teng J., Li Y. Two-component anomalous Hall effect in a magnetically doped topological insulator[J]. Nature Communications, 2018, 9(1): 1282.

[71] He Q. L., Kou X., Grutter A. J., et al. Tailoring exchange couplings in magnetic topological-insulator/antiferromagnet heterostructures[J]. Nature Materials, 2017, 16(1): 94-100.

[72] Katmis F., Lauter V., Nogueira F. S., et al. A high-temperature ferromagnetic topological insulating phase by proximity coupling[J]. Nature, 2016, 533(7604): 513-516.

[73] Li M., Chang C.-Z., Kirby B. J., et al. Proximity-Driven Enhanced Magnetic Order at Ferromagnetic-Insulator--Magnetic-Topological-Insulator Interface[J]. Physical Review Letters, 2015, 115(8): 087201.

[74] Tang C., Chang C.-Z., Zhao G., et al. Above 400-K robust perpendicular ferromagnetic phase in a topological insulator[J]. Science Advances, 2017, 3(6): e1700307.

[75] Frolov S. M., Manfra M. J., Sau J. D. Topological superconductivity in hybrid devices[J]. Nature Physics, 2020, 16(7): 718-724.

[76] Che X., Murata K., Pan L., et al. Proximity-Induced Magnetic Order in a Transferred Topological Insulator Thin Film on a Magnetic Insulator[J]. ACS Nano, 2018, 12(5): 5042-5050.

[77] Stoner E. C. Collective electron ferromagnetism[J]. Proceedings of the Royal Society of London. Series A. Mathematical and Physical Sciences, 1938, 165(922): 372-414.

[78] Anderson P. W. Local Moments and Localized States[J]. Science, 1978, 201(4353): 307-316.

[79] Anderson P. W. Localized Magnetic States in Metals[J]. Physical Review, 1961, 124(1): 41-53.

[80] Wang Z., Zhang T., Ding M., et al. Electric-field control of magnetism in a few-layered van der Waals ferromagnetic semiconductor[J]. Nature Nanotechnology, 2018, 13(7): 554-559.

[81] Verzhbitskiy I. A., Kurebayashi H., Cheng H., et al. Controlling the magnetic anisotropy in $Cr_2Ge_2Te_6$ by electrostatic gating[J]. Nature Electronics, 2020, 3(8): 460-465.

[82] Wang N., Tang H., Shi M., et al. Transition from Ferromagnetic Semiconductor to Ferromagnetic Metal with Enhanced Curie Temperature in Cr2Ge2Te6 via Organic Ion Intercalation[J]. Journal of the American Chemical Society, 2019, 141(43): 17166-17173.

[83] Li T., Jiang S., Sivadas N., et al. Pressure-controlled interlayer magnetism in atomically thin CrI3[J]. Nature Materials, 2019, 18(12): 1303-1308.

[84] Song T., Fei Z., Yankowitz M., et al. Switching 2D magnetic states via pressure tuning of layer stacking[J]. Nature Materials, 2019, 18(12): 1298-1302.

[85] Cai W., Sun H., Xia W., et al. Pressure-induced superconductivity and structural transition in ferromagnetic $CrSiTe_3$[J]. Physical Review B, 2020, 102(14): 144525.

[86] Zhang H., Niu C., Zhang J., et al. Spin-crossover induced ferromagnetism and layer stacking-order change in pressurized 2D antiferromagnet MnPS3[J]. Physical

Chemistry Chemical Physics, 2021, 23(16): 9679-9685.

[87] Chen W., Sun Z., Wang Z., et al. Direct observation of van der Waals stacking–dependent interlayer magnetism[J]. Science, 2019, 366(6468): 983-987.

[88] Webster L., Yan J.-A. Strain-tunable magnetic anisotropy in monolayer $CrCl_3$, $CrBr_3$ and CrI_3[J]. Physical Review B, 2018, 98(14): 144411.

[89] Sheng P., Wang B., Li R. Flexible magnetic thin films and devices[J]. Journal of Semiconductors, 2018, 39(1): 011006.

[90] Li X., Yang J. CrXTe3 (X = Si, Ge) nanosheets: two dimensional intrinsic ferromagnetic semiconductors[J]. Journal of Materials Chemistry C, 2014, 2(34): 7071-7076.

[91] Wang Y., Wang C., Liang S.-J., et al. Strain-Sensitive Magnetization Reversal of a van der Waals Magnet[J]. Advanced Materials, 2020, 32(42): 2004533.

[92] Katmis F., Lauter V., Nogueira F. S., et al. A high-temperature ferromagnetic topological insulating phase by proximity coupling[J], 2016, 533: 513-516.

[93] Lang M., Montazeri M., Onbasli M. C., et al. Proximity Induced High-Temperature Magnetic Order in Topological Insulator - Ferrimagnetic Insulator Heterostructure[J]. Nano Letters, 2014, 14(6): 3459-3465.

[94] Lee J. S., Richardella A., Fraleigh R. D., et al. Engineering the breaking of time-reversal symmetry in gate-tunable hybrid ferromagnet/topological insulator heterostructures[J]. npj Quantum Materials, 2018, 3(1): 51.

[95] Shen Z.-X., Bo X., Cao K., et al. Magnetic ground state and electron-doping tuning of Curie temperature in Fe_3GeTe_2: First-principles studies[J]. Physical Review B, 2021, 103(8): 085102.

[96] Dong X.-J., You J.-Y., Zhang Z., et al. Great enhancement of Curie temperature and magnetic anisotropy in two-dimensional van der Waals magnetic semiconductor heterostructures[J]. Physical Review B, 2020, 102(14): 144443.

[97] Dong X.-J., You J.-Y., Gu B., et al. Strain-Induced Room-Temperature Ferromagnetic Semiconductors with Large Anomalous Hall Conductivity in Two-Dimensional $Cr_2Ge_2Se_6$[J]. Physical Review Applied, 2019, 12(1): 014020.

[98] Manchon A., Koo H. C., Nitta J., et al. New perspectives for Rashba spin–orbit coupling[J]. Nature Materials, 2015, 14(9): 871-882.

[99] Eremeev S. V., Men'shov V. N., Tugushev V. V., et al. Magnetic proximity effect at the three-dimensional topological insulator/magnetic insulator interface[J]. Physical Review B, 2013, 88(14): 144430.

[100] Wei P., Katmis F., Assaf B. A., et al. Exchange-Coupling-Induced Symmetry Breaking in Topological Insulators[J]. Physical Review Letters, 2013, 110(18): 186807.

[101] Li H., Huang J.-K., Shi Y., et al. Toward the Growth of High Mobility 2D Transition Metal Dichalcogenide Semiconductors[J]. Advanced Materials Interfaces, 2019, 6(24): 1900220.

[102] Wang Q. H., Kalantar-Zadeh K., Kis A., et al. Electronics and optoelectronics of two-dimensional transition metal dichalcogenides[J]. Nature Nanotechnology, 2012, 7(11): 699-712.

[103] Zhang D., Liu Y., He M., et al. Room temperature near unity spin polarization in 2D

Van der Waals heterostructures[J]. Nature Communications, 2020, 11(1): 4442.

[104] Wu X., Feng Y., Li S., et al. 2D $Mn_2C_6Se_{12}$ and $Mn_2C_6S_6Se_6$: Intrinsic Room-Temperature Dirac Spin Gapless Semiconductors and Perfect Spin Transport Properties[J]. The Journal of Physical Chemistry C, 2020, 124(29): 16127-16135.

[105] Wang Z., Gutiérrez-Lezama I., Ubrig N., et al. Very large tunneling magnetoresistance in layered magnetic semiconductor CrI_3[J]. Nature Communications, 2018, 9(1): 2516.

[106] Lin M.-W., Zhuang H. L., Yan J., et al. Ultrathin nanosheets of $CrSiTe_3$: a semiconducting two-dimensional ferromagnetic material[J]. Journal of Materials Chemistry C, 2016, 4(2): 315-322.

[107] Bonilla M., Kolekar S., Ma Y., et al. Strong room-temperature ferromagnetism in VSe_2 monolayers on van der Waals substrates[J]. Nature Nanotechnology, 2018, 13(4): 289-293.

[108] Zhang H., Chen R., Zhai K., et al. Itinerant ferromagnetism in van der Waals $Fe_{5-x}GeTe_2$ crystals above room temperature[J]. Physical Review B, 2020, 102(6): 064417.

[109] Seo J., Kim D. Y., An E. S., et al. Nearly room temperature ferromagnetism in a magnetic metal-rich van der Waals metal[J]. Science Advances, 2020, 6(3): eaay8912.

[110] Mondal S., Khan N., Mishra S. M., et al. Critical behavior in the van der Waals itinerant ferromagnet Fe_4GeTe_2[J]. Physical Review B, 2021, 104(9): 094405.

[111] Wisniowski P., Wrona J., Stobiecki T., et al. Magnetic Tunnel Junctions Based on Out-of-Plane Anisotropy Free and In-Plane Pinned Layer Structures for Magnetic Field Sensors[J]. IEEE Transactions on Magnetics, 2012, 48(11): 3840-3842.

[112] Ruderman M. A., Kittel C. Indirect Exchange Coupling of Nuclear Magnetic Moments by Conduction Electrons[J]. Physical Review, 1954, 96(1): 99-102.

[113] Kasuya T. A Theory of Metallic Ferro- and Antiferromagnetism on Zener's Model[J]. Progress of Theoretical Physics, 1956, 16(1): 45-57.

[114] Yosida K. Magnetic Properties of Cu-Mn Alloys[J]. Physical Review, 1957, 106(5): 893-898.

[115] Pertijs M. a. P., Makinwa K. a. A., Huijsing J. H. A Single-Trim CMOS Bandgap Reference With a 3σ Inaccuracy of ±0.15% From −40℃ to 125℃[J]. IEEE Journal of Solid-State Circuits, 2005, 40(12): 2805-2815.

[116] Anderson P. W. Theory of Magnetic Exchange Interactions:Exchange in Insulators and Semiconductors[J]. Journal of Physics C: Solid State Physics, 1963, 14: 99-214.

[117] Schrieffer J. R., Wolff P. A. Relation between the Anderson and Kondo Hamiltonians[J]. Physical Review, 1966, 149(2): 491-492.

[118] He T., Wang Z., Zhong F., et al. Etching Techniques in 2D Materials[J]. Advanced Materials Technologies, 2019, 4(8): 1900064.

[119] Park H., Shin G. H., Lee K. J., et al. Atomic-scale etching of hexagonal boron nitride for device integration based on two-dimensional materials[J]. Nanoscale, 2018, 10(32): 15205-15212.

[120] Jia J., Jang S. K., Lai S., et al. Plasma-Treated Thickness-Controlled Two-Dimensional Black Phosphorus and Its Electronic Transport Properties[J]. ACS Nano, 2015, 9(9): 8729-8736.

[121] Sun H., Dong J., Liu F., et al. Etching of two-dimensional materials[J]. Materials Today, 2021, 42: 192-213.

[122] Yang T. Y., Wan Q., Yan D. Y., et al. Directional massless Dirac fermions in a layered van der Waals material with one-dimensional long-range order[J]. Nature Materials, 2020, 19(1): 27-33.

[123] Moore J. E., Balents L. Topological invariants of time-reversal-invariant band structures[J]. Physical Review B, 2007, 75(12): 121306.

[124] Liu W., Zhang H., Shi J.-A., et al. A room-temperature magnetic semiconductor from a ferromagnetic metallic glass[J]. Nature Communications, 2016, 7(1): 13497.

[125] Matsukura F., Tokura Y., Ohno H. Control of magnetism by electric fields[J]. Nature Nanotechnology, 2015, 10(3): 209-220.

[126] He L., Xiu F., Wang Y., et al. Epitaxial growth of Bi_2Se_3 topological insulator thin films on Si (111)[J]. Journal of Applied Physics, 2011, 109(10): 103702-103702.

[127] He L., Xiu F., Yu X., et al. Surface-Dominated Conduction in a 6 nm thick Bi_2Se_3 Thin Film[J]. Nano Letters, 2012, 12(3): 1486-1490.

[128] Lu H.-Z., Shen S.-Q. Weak localization of bulk channels in topological insulator thin films[J]. Physical Review B, 2011, 84(12): 125138-125138.

[129] Hikami S., Larkin A. I., Nagaoka Y. Spin-Orbit Interaction and Magnetoresistance in the Two Dimensional Random System[J]. Progress of Theoretical Physics, 1980, 63(2): 707-710.

[130] Xu S.-Y., Neupane M., Liu C., et al. Hedgehog spin texture and Berry's phase tuning in a magnetic topological insulator[J]. Nature Physics, 2012, 8(8): 616-622.

[131] Altshuler B. L., Aronov A. G., Khmelnitsky D. E. Effects of electron-electron collisions with small energy transfers on quantum localisation[J]. Journal of Physics C: Solid State Physics, 1982, 15(36): 7367-7386.

[132] Jing Y., Huang S., Zhang K., et al. Weak antilocalization and electron–electron interaction in coupled multiple-channel transport in a Bi_2Se_3 thin film[J]. Nanoscale, 2016, 8(4): 1879-1885.

[133] Liu M., Chang C.-Z., Zhang Z., et al. Electron interaction-driven insulating ground state in Bi_2Se_3 topological insulators in the two-dimensional limit[J]. Physical Review B, 2011, 83(16): 165440.

[134] Lu H.-Z., Shi J., Shen S.-Q. Competition between Weak Localization and Antilocalization in Topological Surface States[J]. Physical Review Letters, 2011, 107(7): 076801.

[135] Brahlek M., Koirala N., Bansal N., et al. Transport properties of topological insulators: Band bending, bulk metal-to-insulator transition, and weak anti-localization[J]. Solid State Communications, 2015, 215-216: 54-62.

[136] Pan Z.-H., Fedorov A., Gardner D., et al. Measurement of an exceptionally weak electron-phonon coupling on the surface of the topological insulator Bi_2Se_3 using angle-resolved photoemission spectroscopy[J]. Physical Review Letters, 2012, 108(18): 187001.

[137] Wu H., Xu Y., Deng P., et al. Spin-Orbit Torque Switching of a Nearly Compensated

Ferrimagnet by Topological Surface States[J]. Advanced Materials, 2019, 31(35): 1901681.

[138] Wang Y., Deorani P., Banerjee K., et al. Topological surface states originated spin-orbit torques in Bi 2 Se 3[J]. Physical Review Letters, 2015, 114(25): 257202.

[139] Haihui Z., Xinhou C., Chen O., et al. Generation and manipulation of chiral terahertz waves in the three-dimensional topological insulator Bi_2Te_3[J]. Advanced Photonics, 2020, 2(6): 066003.

[140] Hamh S. Y., Park S.-H., Han J., et al. Anisotropic Terahertz Emission from Bi 2 Se 3 Thin Films with Inclined Crystal Planes[J]. Nanoscale research letters, 2015, 10(1): 489.

[141] Tu C.-M., Yeh T.-T., Tzeng W.-Y., et al. Manifestation of a second Dirac surface state and bulk bands in THz radiation from topological insulators[J]. Scientific reports, 2015, 5: 14128.

[142] Zhu L.-G., Kubera B., Mak K. F., et al. Effect of surface states on terahertz emission from the Bi 2 Se 3 surface[J]. Scientific reports, 2015, 5: 10308.

[143] Kampfrath T., Battiato M., Maldonado P., et al. Terahertz spin current pulses controlled by magnetic heterostructures[J]. Nature Nanotechnology, 2013, 8(4): 256-260.

[144] Khang N. H. D., Ueda Y., Hai P. N. A conductive topological insulator with large spin Hall effect for ultralow power spin–orbit torque switching[J]. Nature Materials, 2018, 17(9): 808-813.

[145] Wang Y., Zhu D., Wu Y., et al. Room temperature magnetization switching in topological insulator-ferromagnet heterostructures by spin-orbit torques[J]. Nature Communications, 2017, 8(1): 1-6.

[146] Wang X., Cheng L., Zhu D., et al. Ultrafast Spin-to-Charge Conversion at the Surface of Topological Insulator Thin Films[J]. Advanced Materials, 2018, 30(52): 1-19.

[147] Chen X., Wang H., Wang C., et al. Efficient Generation and Arbitrary Manipulation of Chiral Terahertz Waves Emitted from Bi2Te3–Fe Heterostructures[J]. Advanced Photonics Research, 2021, 2(4): 2000099.

[148] Zhuang H. L., Kent P. R. C., Hennig R. G. Strong anisotropy and magnetostriction in the two-dimensional Stoner ferromagnet Fe_3GeTe_2[J]. Physical Review B, 2016, 93(13): 134407.

[149] May A. F., Calder S., Cantoni C., et al. Magnetic structure and phase stability of the van der Waals bonded ferromagnet Fe_3GeTe_2[J]. Physical Review B, 2016, 93(1): 014411.

[150] Kumar N., Hendrikx R. W. A., Adam A. J. L., et al. Thickness dependent terahertz emission from cobalt thin films[J]. Optics Express, 2015, 23(11): 14252.

[151] Gorelov S., Mashkovich E., Tsarev M., et al. Terahertz Cherenkov radiation from ultrafast magnetization in terbium gallium garnet[J]. Physical Review B, 2013, 88(22): 220411.

[152] Mikhaylovskiy R., Hendry E., Kruglyak V., et al. Terahertz emission spectroscopy of laser-induced spin dynamics in TmFeO 3 and ErFeO 3 orthoferrites[J]. Physical Review B, 2014, 90(18): 184405.

[153] Lang M., He L., Kou X., et al. Competing Weak Localization and Weak Antilocalization in Ultrathin Topological Insulators[J]. Nano Letters, 2013, 13(1): 48-53.

Outcomes Achieved During PhD Study

Journal article

[1] **Wang H,** Murata K, *et al.*. Proximity-Induced Magnetic Order in Topological Insulator on Ferromagnetic Semiconductor[J]. SCIENCE CHINA Information Sciences, 2023 (**IF: 8.8, JCR:Q1,** Accepted)

[2] **Wang H,** Lu H, *et al.*. Interfacial engineering of ferromagnetism in wafer-scale van der Waals Fe_4GeTe_2 far above room temperature[J]. Nature Communications, 14, 2483 (2023). **(IF: 17.7, JCR:Q1)**

[3] Chen X, **Wang H,** Liu H, *et al.*. Generation and Control of Terahertz Spin Currents in Topology Induced 2D Ferromagnetic Fe_3GeTe_2| Bi_2Te_3 Heterostructures[J]. Advanced Materials, 2022, 34(9): 2106172. **(IF: 30.25, JCR:Q1)**

[4] Zhao H, Chen X, Ouyang C, **Wang H**, *et al.*. Generation and manipulation of chiral terahertz waves in the three-dimensional topological insulator Bi_2Te_3[J]. Advanced Photonics, 2020, 2(6): 066003. **(IF: 13.58, JCR:Q1)**

[5] Fang Z, **Wang H**, Wu X, *et al.*. Nonlinear terahertz emission in the three-dimensional topological insulator Bi_2Te_3 by terahertz emission spectroscopy[J]. Applied Physics Letters, 2019, 115(19): 191102. **(IF: 3.6, JCR:Q2)**

[6] **Wang H**, Zhao H, Wen L, *et al.*. High-performance THz emission: From topological insulator to topological spintronics[J], ACTA PHYSICA SINICA, 2020, 69(20): 200704 **(IF: 0.6, JCR:Q4)**

[7] Pandey C A, Li X, **Wang H,** *et al.*. Enhancing perpendicular magnetic anisotropy through dead layer reduction utilizing precise control of Mg insertions[J]. Journal of Magnetism and Magnetic Materials, 2020, 511: 166956. **(IF: 2.84, JCR:Q2)**

[8] Wang H, Liu Y, Wu P, **Wang H**, *et al.*. Above room-temperature ferromagnetism in wafer-scale two-dimensional van der Waals Fe_3GeTe_2 tailored by a topological insulator[J]. ACS nano, 2020, 14(8): 10045-10053. **(IF: 16.2, JCR:Q1)**

[9] Chen X, **Wang H**, Wang C, *et al.*. Efficient Generation and Arbitrary Manipulation of Chiral Terahertz Waves Emitted from Bi_2Te_3–Fe Heterostructures[J]. Adv. Photonics Res., 2: 2000099

[10] Sun Y, Zhang F, **Wang H,** *et al.*. Research and Application of Spintronic Terahertz Emitter Based on Ultrafast Spintronics[J]. Acta Electronica Sinica, 2022, 50(12), 2854-2873

Conference paper

[1] Chen X, **Wang H,** Wei G, *et al.*. Generation and Manipulation of Chiral Terahertz Waves in Iron-Topological Insulator Heterostructures[C]//2020 45th International Conference

on Infrared, Millimeter, and Terahertz Waves (IRMMW-THz). IEEE, 2020: 1-2.

[2] Chen X, **Wang H,** Wei G, *et al.*. Terahertz Emission Spectroscopy as Contactless Ultrafast Detection for Room-temperature 2D Magnetic Materials[C]//CLEO: Science and Innovations. Optical Society of America, 2020: SM1F. 5.

[3] Zhao H, **Chen X,** Wang H, *et al.*. Topological Insulator-based Terahertz Emission with Manipulated Polarization[C]//CLEO: Science and Innovations. Optical Society of America, 2020: SM1F. 1.

[4] Zhao H, Wu X, **Wang H,** *et al.*. Femtosecond Control of Photocurrent in Topological Insulators[C]//Optical Fibers, Fiber-based Devices and Applications. Optical Society of America, 2019

[5] Li P, Chen X, **Wang H,** *et al.*. Magnetic 2D ferromagnetic heterostructures for spintronic THz emission[C]//2021 46th International Conference on Infrared, Millimeter and Terahertz Waves (IRMMW-THz). IEEE, 1-2.

Oral presentation

[1] Tunable Terahertz Wave via Synthesis of Spin and Charge Induced Radiations in Topological Insulator. INTERMAG 2021 Conference, 2021, online.